Western Australia School of Mines
Department of Exploration Geophysics

Fluid injection in reservoir rocks with X-ray CT scanning and active ultrasonic monitoring

Sofia Alexandra Correia Lopes

This thesis is presented for the Degree of
Doctor of Philosophy
of
Curtin University

October 2013

DECLARATION

To the best of my knowledge and belief this thesis contains no material previously published by any other person except where due acknowledgement has been made.

This thesis contains no material which has been accepted for the award of any other degree or diploma by any University.

Date:

24/10/2013

Signature:

Sofia Alexandra Correia Lopes

ACKNOWLEDGEMENTS

The biggest and most important “спасибо” (thank you) goes to my supervisor, Dr. Maxim Lebedev, for giving me the freedom to experiment and try many, many ideas. I learned so much!

Dr. Tobias Müller
CSIRO, Earth Science and Resource Engineering
for the constant support and invaluable feedback to our work.

Dr. Boris Gurevich
Department Exploration Geophysics, Curtin University
for giving me a home for my growth from a student to a scientist.

Dr. Ben Clennell
CSIRO, Earth Science and Resource Engineering
for valuable technical and financial contribution.

Dr. Vassili Mikhaltsevitch, Dr. Eva Caspari & Mr. Qi Qiaomu
Department Exploration Geophysics, Curtin University
Dr. Lionel Esteban & Dr. Joël Sarout
CSIRO, Earth Science and Resource Engineering
for laboratorial and technical support.

This PhD was partially funded by *Australia-China Natural Gas Technology Fund* (Contract Number CTR-DJ-04194-1), by the *Australian Commonwealth Government* through the *Cooperative Research Centre for Greenhouse Gas Technologies* (*CO2CRC*), by the sponsors of the *Curtin Reservoir Geophysics Consortium* (*CRGC*) and by the *Commonwealth Scientific and Industrial Research Organisation (*CSIRO).

The limestone sample in Part I was kindly provided by *CSIRO*.
The carbonate samples in Part II were kindly provided by *Petrobras*.

ABSTRACT

Quantitative interpretation of time-lapse seismic data requires knowledge of the relationship between elastic wave velocities and fluid saturation. This relationship is not unique but depends on the spatial distribution of the fluid in the pore-space of the rock. In turn, the fluid distribution depends on the injection rate. To study this dependency, forced imbibition experiments with constant and variable injection rates, at ambient and under-pressure conditions were performed on air-dry sandstones and carbonates. Water and oil was injected in cylindrical samples of sandstones and carbonates. The fluid flow was simultaneously monitored by X-Ray Computed Tomography (CT) and ultrasonic acoustic waves through transducers of frequency 1 MHz. This methodology enabled matching the intrusion of fluids with specific responses of the P-wave velocity and fluid saturation.

As soon as the fluid entered the ultrasonically monitored position (or when the local fluid saturation increased) a well-marked increase or decrease in the P-wave velocity was observed. This was accompanied by a decrease in P-wave amplitude that continued progressively until full saturation (at which the amplitude increased considerably). Water injection in sandstones at different injection rates showed specific responses. A high injection rate, when compared to the natural imbibition rate, promoted a flat, compact saturation front and a fast increase in the P-wave velocity and fluid saturation while the low injection rate promoted a diffusive saturation front and both, the P-wave velocity and fluid saturation, increased slowly with the presence of fluid. A common evolution of the P-wave velocity and fluid saturation with changing the injection rate was found for both sandstones and carbonates. It was also found that the same P-wave velocity was obtained for different water saturations. The influence of gravity on the geometry of the saturation front was studied in a limestone. When the injection was vertical (parallel to gravity), the saturation front was compact (higher local water saturation) while it was more diffusive (lower local water saturation) in the horizontal configuration (direction of injection perpendicular to gravity). CT scans were analysed to spot structural heterogeneities of the sample and study its influence in fluid distribution. The P-wave velocity dependence with confining pressure, $V_P(p_c)$, was evaluated for carbonates. Measurements at dry and fully saturated phases evaluated how the P-

wave velocity depended on pressure and how it compared to the effect of the presence of fluids. As expected, the acoustic properties of carbonates were much less sensitive to the presence of fluids when compared to sandstones: lower values of the P-wave velocity were observed for high fluid saturations. Also carbonates produced higher variations in the P-wave velocity due to the increase in confining pressure than due to the presence of fluids. Structural heterogeneities (i.e. the presence of large pores or fractures) could also be inferred through $V_P(p_c)$. More particularly, the non-linearity of $V_P(p_c)$ showed that at a certain confining pressure, fractures closed (or large pores collapsed). This led to a sudden increase in local density and, consequently, the P-wave velocity increased rapidly.

The overall results confirmed that the injection rate has significant influence on fluid distribution and consequently, in the corresponding acoustic response, and that acoustic wave propagation is very sensitive to spatial fluid distribution.

INDEX

INTRODUCTION

"… seismic-wave propagation is affected by the physical (…) characteristics of the pore-filling fluid and its interaction with the solid phase."

Biot (1956)

Quantification of fluid flow through porous media is an essential part of hydrocarbon recovery and reservoir characterization. In particular, the controlled replacement of one fluid by another is a common procedure in order to stimulate reservoir performance, for example, for secondary oil recovery, waterflooding or CO_2 sequestration. When injecting fluids in a rock, acoustic data can indicate the presence of fluids. However, its interpretation requires a well-founded knowledge of heterogeneous porous media, particularly of acoustic signatures in multi-phase reservoirs. Multi-phase flow phenomena in porous media are crucial when dealing with the recovery or storage of fluids in the subsurface. Subsurface oil reservoirs often contain a combined variety of fluid phases: water, oil and gas. To outline the structure of reservoirs and discern fluid phases is the overall goal in seismic exploration and monitoring. Particularly, time-lapse seismic reservoir monitoring is a method that aims at the continuous mapping of fluid distribution and flow patterns in time and space (Lumley 2001). This is done by acquiring successive 3D seismic data surveys over the area of interest for a period of time using acoustic sensors arrays. The time-lapse seismic method remotely analyses the movement of reservoir fluids and can be used to track fluid fronts. It is meant to observe changes in seismic signals resulting from changes in the acoustic impedance. Since the acoustic impedance is the product of velocity and density, time-lapse signals are affected by the compressibility of the reservoir rock and of the pore fluids (Assefa, McCann & Sothcott 2003). For example, soft rocks, such as sandstones, will generate higher impedance contrasts than stiff rocks such as carbonates. Fluids with strong density contrasts like gas-oil or gas-water will have distinguishable signals while heavy oils flooded by water may be very challenging to monitor seismically (Lumley 2001). When seismic waves are recorded during fluid injection changes in wave-

amplitude, wavelength and arrival time are observed (Albright et al. 1994). More particularly, seismic wave velocities and attenuation are affected by the degree of saturation and spatial distribution of fluids (Li, Zhong & Pyrak-Nolte 2001; Müller, Gurevich & Lebedev 2010). Figure 1 shows the change in wave-amplitude and P-wave arrival time due to the presence of water when water was injected into a dry sandstone (results from the fluid imbibition presented in this thesis, Chapter 2). Figure 2 shows that for the same water saturation is possible to have very different fluid distributions (Cadoret, Marion & Zinszner 1995). Importantly, each spatial distribution results in a different acoustic wave velocity. For an extensive review on the influence of saturation and fluid distribution on seismic wave velocities see Müller, Gurevich & Lebedev (2010).

Fluid substitution is an important part of the time-lapse seismic analysis as it provides a tool for fluid detection and quantification in a reservoir. This analysis is generally performed using Gassmann's equation (Gassmann 1951): it relates the bulk and shear moduli of a rock to its solid matrix, pore network and fluid properties. Including the density of the rock, these are the only parameters needed to estimate longitudinal (P) and shear (S) wave velocities (in the lower frequency limit). The change in the rock's moduli (due to the presence of fluids) is directly related to the change in the acoustic wave velocity. Particularly, the Gassmann-Wood theory establishes the direct proportionality between acoustic velocities and density/bulk modulus of the mixed pore fluid phase.

A particular case of fluid substitution is *imbibition*. It is defined as the displacement of a non-wetting fluid by a wetting fluid. It is a process driven by surface energy through the action of capillary pressure (the difference in pressure across the interface of two immiscible fluids) (Akin et al. 2000; Morrow & Mason 2001). In a vertical-directed injection the displacement of the fluids is the result of the balance between capillary forces (upward) and gravity forces (downward, inhibiting the imbition). In a natural or spontaneous imbibition, the process by which the wetting fluid is drawn into the pore space is the capillary action (suction). In a dynamic forced imbibition experiment, the imbibition rate is imposed by an injection pump and the non-wetting fluid is displaced into the porous medium under a pressure gradient.

There is a considerable number of variables that influence the propagation of acoustic waves in fluid substitution processes: (1) the type of rock (mainly, its mineralogical composition), (2) the type of fluids present in the pore space (for example, gas-water or oil-water systems) (Lumley 2001), (3) the type of pores (predominance of micro- or macro-porosity, closed or open pores, etc.), (4) fluid distribution (Cadoret, Marion & Zinszner 1995), and (5) pressure (Guéguen & Palciauskas 1994). The most influential forces governing fluid flow are *viscous*, *gravity* and *capillary* forces as well as the applied external pressure (Leverett 1940; Karimaie & Torsaeter 2007; Riaz et al. 2007). The relative importance of capillary, viscous and gravitational forces will determine the overall flow regime. For water imbition (injection of water in an air-saturated system), capillary and gravity forces are the governing forces. Viscous forces, in this case, are negligible as the residual air offers virtually no resistance to the water flow. Viscous forces are only relevant if the viscosity of the injecting fluid is comparable to the viscosity of the displaced fluid. For example, when injecting water in an oil-saturated system, viscous forces govern the fluid flow (Akin et al. 2000). Gravity forces are caused by differences in the density of the fluids. The influence of gravity increases with the increase in density contrast between the fluids (for example, water/air). More significantly, gravity forces tend to stabilize the interface between fluids and inhibit fluid displacement (Birovlej et al. 1991). Capillary forces are present in multiphase flow and they are always active at the interface between two immiscible fluid phases (Skjæveland & Kleppe 1992). In water imbibition, capillary forces control the microscopic fluid distribution.

It is also of great importance to predict the recovery of the residual fluid, i.e. the percentage of fluid expelled. It is a challenging problem as the effectiveness of the imbibition depends very much on the nature of the porous medium (porosity, permeability and pore structure) and of the fluid system (viscosity of each fluid) (Li & Horne 2010) and on the rate of the injection (Babadagli & Ershaghi 1992). The displacement efficiency can be maximized by controlling the injection rate (Sudaryanto & Yortsos 2000). The procedure of changing injection rates during a continuous fluid injection is a common procedure to control pore pressure and avoid reservoir depletion (Teufel, Rhett & Farrell 1991; Yousef et al. 2006). However, different injection rates create different acoustic responses (Meleán, Broseta &

Blossey 2003). Also, the injection rate has a strong impact on immiscible-phase displacement: at high rates the saturation front is sharp with a straight piston-like displacement while at low rates capillarity controls the distribution of the fluid in the micropore-space causing a diffusive broadening of the saturation front (Blunt 1995; Meleán, Broseta & Blossey 2003). Thus, understanding the impact of injection rate on fluid distribution and its associated acoustic response may have significant implications in reservoir surveillance.

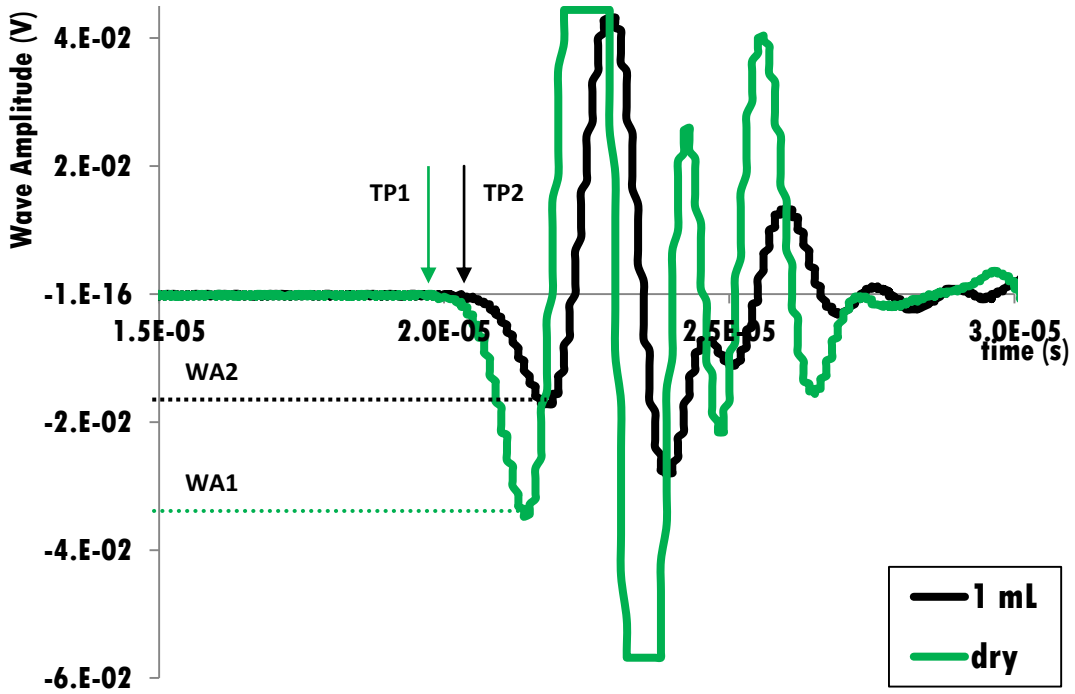

Figure 1 Waveforms for dry sandstone (black line) and after injecting 1 mL of water (green line). Note the decrease in wave amplitude (from WA1 to WA2) and the increase in the P-wave arrival time (from TP1 to TP2) with the presence of water.

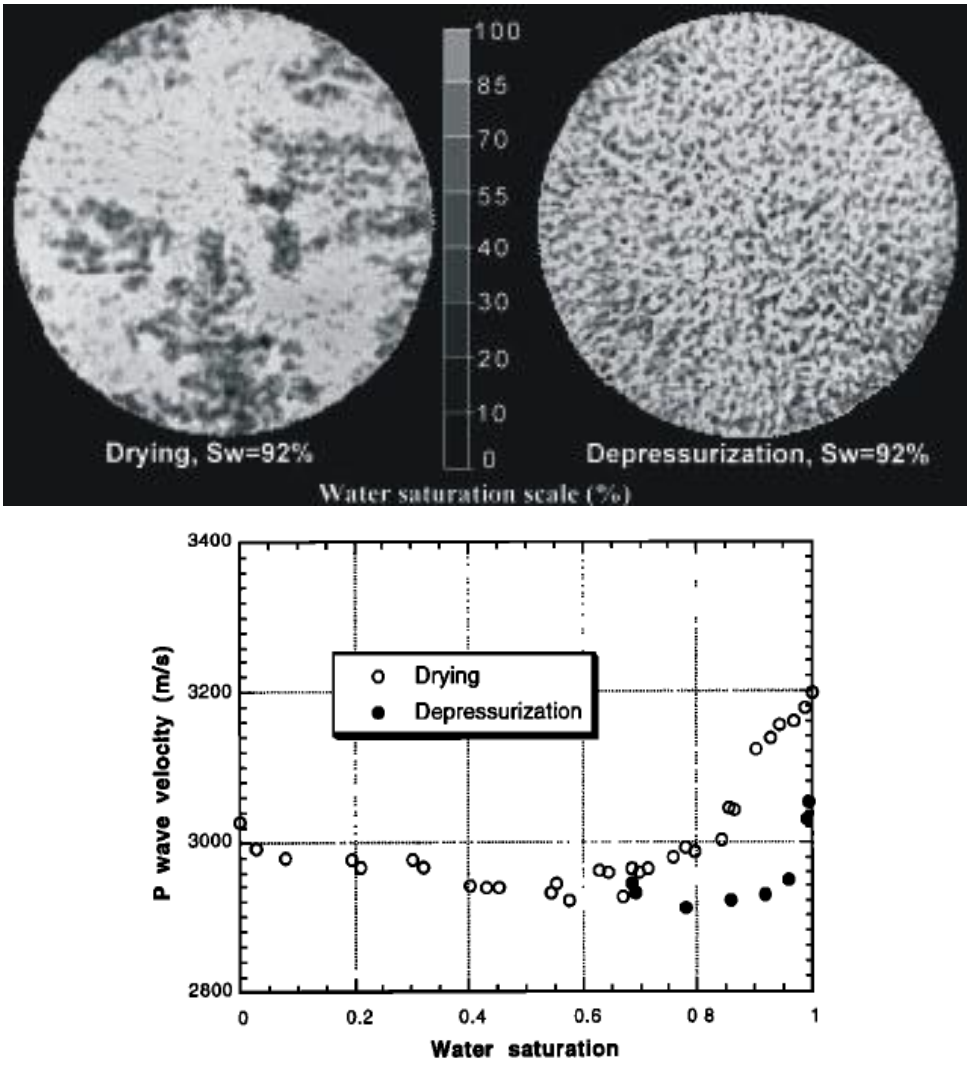

Figure 2 Different fluid distribution at the end of (a) drainage by drying and (b) saturation by depressurization, result in the same final water saturation (92%). However, the P-wave velocity for each case is different (Cadoret, Mavko & Zinszner 1998).

1. BASIC CONCEPTS OF TWO-PHASE FLUID FLOW

One of the main goals in reservoir characterization is to quantify and localize fluid content. For that, quantitative relationships between fluid saturation and acoustic wave velocities are needed. Variations in seismic properties can be related to fluid changes within the reservoir and velocity and amplitude analysis of elastic waves are common procedures to infer about the presence of fluids. However, there is a significant array of parameters that bring their own contribution into fluid processes in reservoirs: the porous structures (like grain size and permeability), the rock's properties (such as porosity, mineral composition and level of heterogeneity) and wetting condition (for example, saturation of each fluid and wettability, which evaluates the preference of the solid matrix to be in contact with fluids). In the special case of multi-phase fluid systems (gas, water and oil can easily co-exist in reservoirs), heterogeneity and fluid mixture are key factors that complicate the interpretation of seismic signatures. Even in the classic case of the two-phase fluid system of air/water, in a homogeneous sample, a direct relationship between acoustic velocities and saturation is difficult to establish since the fluid flow result, most of the time, in partial saturations. Partial or *patchy saturation* (Figure 3) of a fluid or fluids in a porous media has a significant impact in acoustic wave propagation by creating local pressure gradients. Moreover, the size of the patches and their distribution from regularly distributed of simple geometry (White, Mihailova & Lyakhovitsky 1975) or of more general shape (Johnson 2001) to randomly distributed (Müller & Gurevich 2004), cause different acoustic signatures. Each case induces attenuation (mostly due to grain softening) and velocity dispersion (mostly due to heterogeneities) (Li, Zhong & Pyrak-Nolte 2001) at different levels, complicating the interpretation and distinction of pore-scale effects. Cadoret, Marion & Zinszner (1995), Cadoret, Mavko & Zinszner (1998), Monsen & Johnstad (2005) and Lebedev et al. (2009) have experimentally assessed the influence of patchy saturation in wave propagation (different imbibition techniques resulted in different fluid distributions). Though, their review was mostly qualitative, some theoretical predictions and numerical simulations of velocity-saturation relationships were made by applying Gassmann's theory.

Gassmann's generalized equations are the most used set of relationships to determine different characteristics of rock samples and *in situ* rocks based on field measurements and laboratorial experiments. Most importantly, it accounts for the influence of saturation on the propagation of acoustic wave velocities. Given a set of P-wave velocities (V_P), S-wave velocities (V_S) and the density of the dry rock (ρ), Gassmann's equations compute the "new" acoustic velocities when fluids are present based on the increase in the effective bulk modulus. The acoustic velocities and the rock's density relate to the bulk modulus, K, and shear modulus, μ, as seen in Equations 1 and 2, respectively,

$$V_P = \sqrt{\frac{K+\frac{4}{3}\mu}{\rho}} \tag{1}$$

$$V_S = \sqrt{\frac{\mu}{\rho}} \tag{2}$$

The Gassmann equation estimates the bulk modulus of the saturated rock, K_{sat}, (Mavko & Nolen-Hoeksema 1994) as,

$$\frac{K_{sat}}{K_0 - K_{sat}} = \frac{K_{dry}}{K_0 - K_{dry}} + \frac{K_{fluid}}{\phi(K_0 - K_{fluid})} \tag{3}$$

where K_0, K_{dry}, and K_{fluid} are the bulk modulus of the minerals, dry rock and pore fluid, respectively. ϕ is the porosity of the rock. Therefore, by replacing K_{sat} in Equation 1 it is possible to estimate V_P for the saturated sample. K is a good parameter at evaluating the rock's compressibility which invariable changes in the presence of fluids.

Discrepancies between Gassmann's prediction and calculated acoustic velocities (based on experimental measurements) can occur due, for example, the use of high frequency acoustic measurements (in the range of kHz), the existence of patchy saturation or experiments being performed on non-homogeneous samples. Gassmann's equations have evolved in the hands of other scientists (Biot 1956; Hill 1963) to accommodate Gassmann's initial assumptions and mirror more realistic

situations and less strict conditions. In particular, in the static (or low-frequency) limit, saturation can be considered homogeneous, and the rock will be saturated with a homogeneous mixture of the fluids. Here, the effective modulus of the pore fluid is given by Wood's law (Mavko, Mukerji & Dvorkin 1998),

$$\frac{1}{K_W} = \frac{S_1}{K_{fl1}} + \frac{S_2}{K_{fl2}} + \cdots + \frac{S_n}{K_{fln}} \tag{4}$$

$1/K_W$ is the inverse bulk modulus averaging of n fluids and $S_1, \ldots, S_n$ are the partial saturations of each fluid ($i = 1, \ldots, n$). So, when dealing with low frequencies, the Gassmann-Wood (GW) theory makes a better prediction about the saturation dependence of P-wave velocities.

Equation 4 shows the complexity of two- or multi-phase fluid interactions. As fluids are injected, there is a constant "competition" between the quantity (saturation) of each fluid and their individual contribution to the overall bulk modulus, K_W, and, consequently, to V_P (Equation 1). Therefore, the calculated V_P is the result of a combination of effects derived from the interaction of the P-wave with the solid skeleton, pore fluid and minerals.

Capillary pressure and relative permeability curves are also important concepts when studying two-phase fluid flow. Capillary pressure is the pressure difference between the non-wetting phase and the wetting phase (air and water, respectively, in the water imbibition case). A capillary pressure curve (capillary pressure vs. saturation) aids in understanding fluid distribution in a reservoir/rock and is a good indicator of the comparative contribution between capillary and viscous forces. Permeability evaluates the fluid conductivity of a rock: the rock's ability to store and transport fluids. As water is injected in a dry sample, for example, the rock's water permeability increase as air is expelled and more pore space is available for water's intrusion. Meanwhile, the air permeability decreases (Valvatne & Blunt 2004). Therefore, a relative permeability curve expresses the change on fluid "availability" in the pore space and reflects the competition of multiple fluids for pore space. However, the variations of the capillary pressure and permeability during fluid flow experiments are not easily measurable in laboratory. Moreover, local fluid distributions depend on the interplay of capillary, gravitational and

viscous forces. These are equally difficult to estimate. Within the experimental setup chosen for this thesis it was not possible to measure these quantities and nor could fluid distributions be imaged at pore level. Future work that includes local pore pressure measurements and X-ray micro-tomographic imaging (Arns et al. 2005; Derluyn et al. 2013) will bring new light to pore-scale interactions and their direct impact in wave-propagation.

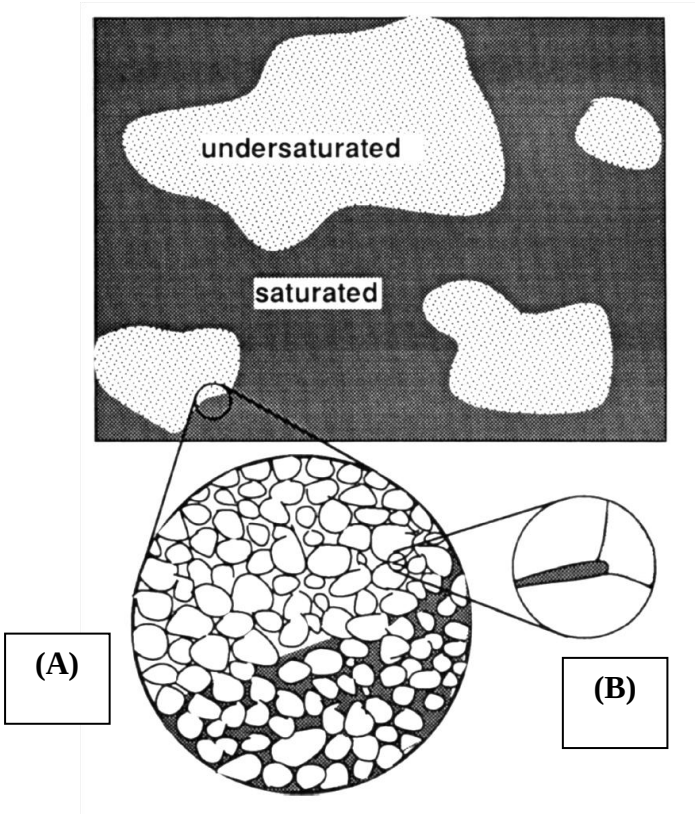

Figure 3 Diagram of patchy saturation at different scales: **(A)** sample scale, between saturated (darker areas) and under-saturated patches; **(B)** pore scale, in-between grains (Mavko & Nolen-Hoeksema 1994).

2. CT IMAGE PROCESSING

X-ray Computed Tomography (CT) complements the results obtained with active ultrasonic monitoring by providing a dimensional image that represents the fluid distribution in the rock and allows visualizing its progression with time.

X-ray CT is a non-destructive method that allows 2D (and 3D) visualization by creating images that map the variations in X-ray attenuation derived from the different densities of the scanned object. Most X-ray CT scanners consist of a single X-ray source and a ring of detectors that rotate around the scanned object. The X-ray source emits a beam of photons and the set of detectors measure the intensity of the received X-ray. While passing the scanned object, the sent signal is attenuated by scattering and absorption. For a monoenergetic beam and a homogenous material, the level of attenuation is given by Beer's Law (Equation 5) (Wellington & Vinegar 1987):

$$I = I_0 \exp(-\mu x) \tag{5}$$

I_0 is the initial X-ray intensity, I is the X-ray intensity measured by the detectors, μ is the linear attenuation coefficient for the scanned material and x is the length of the X-ray path through the scanned material. For a heterogeneous material, for each material i, with attenuation coefficient μ_i and over a length of x_i,

$$I = I_0 \exp\left[\sum_i (-\mu_i x_i)\right] \tag{6}$$

The raw data provided by the X-ray CT scanner is converted into "CT numbers" (of units Hounsfield, HU). The threshold of the CT numbers is set by the computer system. These CT numbers are mapped and the resulting images are presented in a gray-scale: shaded gray (or black) for low CT numbers and light gray (or white) for high CT numbers. The CT number of each pixel of the image is approximately equal to the average of the CT numbers related to the mineral grains, pore-spaces and pore-fluids (Toms-Stewart et al. 2009). In this case, one pixel represents a sample volume of $0.2 \times 0.2 \times 1$ mm^3 and each CT scan contains 512 x 512 pixels.

Each scanning covers 1 mm of the sample's thickness during 3 seconds of exposure. The resolution of the X-ray CT scanner does not allow imaging fluid patch geometry (at pore scale) but it does enable an overall characterization of fluid distribution (at sample scale).

For a solid homogeneous matrix, the CT number of the pixel is equal to the CT number of the grains,

$$\mathrm{CT} = \mathrm{CT}_{\mathrm{matrix}} = \mathrm{CT}_{\mathrm{grain}} \tag{7}$$

In the presence of pores (heterogeneous material with porosity ϕ),

$$\mathrm{CT}_{\mathrm{matrix}} = (1-\phi)\mathrm{CT}_{\mathrm{grain}} \tag{8}$$

If the pores are filled with a fluid,

$$\mathrm{CT}_{\mathrm{matrix}} = (1-\phi)\mathrm{CT}_{\mathrm{grain}} + \phi\mathrm{CT}_{\mathrm{fluid\ 1}} \tag{9}$$

If the pores are filled with two different fluids ($\mathrm{S}_{\mathrm{fluid\ 1}}$ is the saturation of fluid 1 and $\mathrm{CT}_{\mathrm{fluid\ 2}}$ is the CT number of fluid 2),

$$\mathrm{CT}_{\mathrm{matrix}} = (1-\phi)\mathrm{CT}_{\mathrm{grain}} + \mathrm{S}_{\mathrm{fluid\ 1}}\phi\mathrm{CT}_{\mathrm{fluid\ 1}} + (1-\mathrm{S}_{\mathrm{fluid\ 1}})\phi\mathrm{CT}_{\mathrm{fluid\ 2}} \tag{10}$$

If fluid 1 is water and fluid 2 is air, ($\mathrm{S}_{\mathrm{fluid\ 1}} = 0, \mathrm{CT}_{\mathrm{fluid\ 2}} = \mathrm{CT}_{\mathrm{air}}$), the CT number for the sample when it is dry is,

$$\mathrm{CT}_{\mathrm{dry}} = (1-\phi)\mathrm{CT}_{\mathrm{grain}} + \phi\mathrm{CT}_{\mathrm{air}} \tag{11}$$

If the sample is saturated with water ($\mathrm{S}_{\mathrm{fluid\ 1}} = \mathrm{S}_{\mathrm{w}}$), the $\mathrm{CT}_{\mathrm{S_w}}$ number is,

$$\mathrm{CT}_{\mathrm{S_w}} = (1-\phi)\mathrm{CT}_{\mathrm{grain}} + \mathrm{S}_{\mathrm{w}}\phi\mathrm{CT}_{\mathrm{w}} + (1-\mathrm{S}_{\mathrm{w}})\phi\mathrm{CT}_{\mathrm{air}} \tag{12}$$

Therefore, the variation in the CT number due to the presence of water is given by subtracting Equation 12 from Equation 11. The result is,

$$\mathrm{CT_{S_w}} - \mathrm{CT_{dry}} = \mathrm{S_w}\phi(\mathrm{CT_w} - \mathrm{CT_{air}}) \quad (13)$$

For most medical X-ray CT scanners, the CT number of air is "-1000" and the CT number of water is "0". Substituting in Equation 13 results in,

$$\mathrm{CT_{S_w}} - \mathrm{CT_{dry}} = \mathrm{S_w}\phi 1000 \quad (14)$$

The water saturation, S_W, is, then, given directly through the difference in CT numbers (ΔCT) of the scanned images, i.e.,

$$\mathrm{S_w} = \frac{\mathrm{CT_{S_w}} - \mathrm{CT_{dry}}}{\phi 1000} = \frac{\Delta \mathrm{CT}}{\phi 1000} \quad (15)$$

If oil is injected in a dry sample, the oil saturation, $S_{o,}$ is,

$$\mathrm{S_o} = \frac{\mathrm{CT_{S_o}} - \mathrm{CT_{dry}}}{\phi(\mathrm{CT_o} - \mathrm{CT_{air}})} \quad (16)$$

CT_O is the CT number of the oil. So, directly through the CT scans, solid/fluid interactions can be evaluated (1) qualitatively with the variation of the gray scale by identifying areas of high or low CT numbers and (2) quantitatively by calculating fluid saturation with the variation of the CT numbers. It is possible to plot the CT numbers with length of the sample at specific moments of the experiment (Figure 4). This is called a 'CT profile' and is used to estimate ΔCT and calculate the saturation of the injected fluid (Equations 15-16).

Digital manipulation of the raw CT scans was made to enhance the contrast between matrix-air (dry zone) and matrix-water (wet zone) and delimitate the interface (the *saturation front*). The CT scan of the dry sample was subtracted from the consecutive CT scans of the partially water-saturated sample. The resulting image is a map that only features the pixels which CT numbers have changed due to

the presence of water (Figure 5). The CT scans were displayed and the CT numbers analysed using the free image software *ImageJ*.

The error when calculating S_W, $\sigma(S_W)$, is given by the sum of the relative errors in measuring the CT numbers (both the porosity, ϕ, and the factor "1000" are constants),

$$\sigma(S_W) = \sigma\left(CT_{dry}\right) + \sigma(CT_w) = 2.\sigma(CT),\ \sigma\left(CT_{dry}\right) = \sigma(CT_w) \tag{17}$$

The error in measuring CT, $\sigma(CT)$, is given by the average deviations in the CT numbers, ΔCT, relative to the average CT number, $\overline{CT}$. For the medical CT scanner used in this thesis, the calibration values were $\Delta CT = 15$ and $\overline{CT} = 1500$,

$$\sigma(CT) = \frac{\Delta CT}{\overline{CT}} = \frac{15}{1500} = 1\% \tag{18}$$

Replacing in Equation 17, the error in estimating S_W is,

$$\sigma(S_W) = 2 \times 1\% = 2\% \tag{19}$$

Rendering data from CT scanning can produce imaging artifacts that over-enhance or cover details of a sample (for an extensive list of the limitations of X-ray CT see Cnudde & Boone 2013). One of the most common artifacts is "X-ray beam hardening". It makes the boundaries of the scanned object brighter than the inner parts even if they have the same CT number. Also, common are the streak artifacts caused by highly-attenuating inclusions or minerals. (CT scanning is actually a reliable way of detecting heterogeneities inside the sample.) Another issue relays on the voxel size. Any features smaller than the voxel size are averaged within that voxel and will not be distinguished. However, for the purpose of this study, the resolution of the medical CT scanner and the sample-scale of the images were adequate to draw the essential conclusions regarding fluid flow distribution inside the sample and follow the advancement of a saturation front (the wet/dry interface).

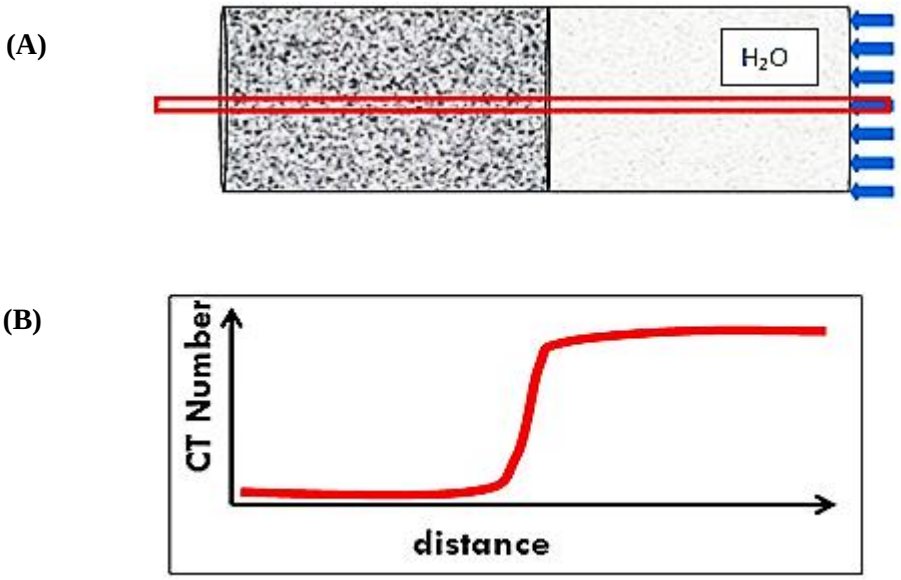

Figure 4 Display of a CT profile of a partially water-saturated sample. The CT numbers are averaged over the area of interest, delimitated by the red in **(A)**, and their change with distance is plotted in **(B)**. The presence of water induces high CT numbers on the right side. Blue arrows indicate the direction of injection.

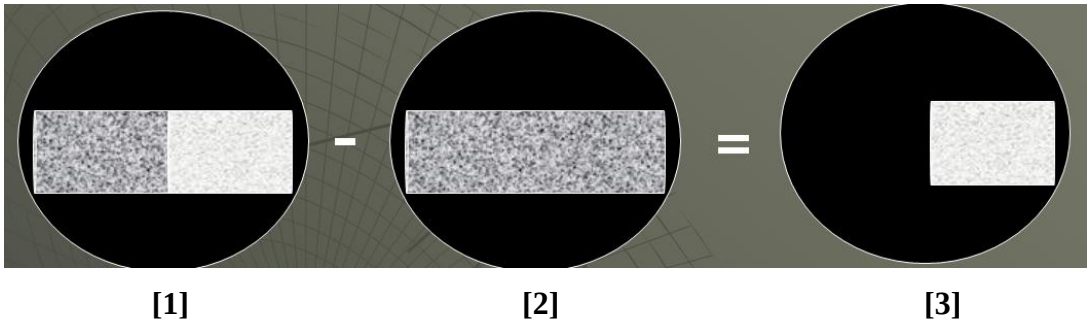

Figure 5 Digital manipulation of the CT scans. The CT scan when the sample is dry **[2]** is subtracted from the CT scan of the sample when partially saturated with water **[1]**. This results in a binarized image where the background was subtracted and only the areas which CT number has changed with the presence of water are featured **[3]**.

3. EXPERIMENTAL BACKGROUND

Several laboratory experiments have been performed with the intention of relating acoustic signatures with the presence and level of saturation of the residual and injected fluids in reservoir rocks. Masuda et al. (1993) monitored P-wave velocities during water infiltration into granite samples. Several pairs of transducers (source and receiver) were located along the cylindrical sample and P-waves were picked during the vertical injection of water. The sudden increase of the P-wave velocity revealed a saturation front passing each consecutive pair of transducers from bottom to top of the sample. Further velocity tomography revealed that the line of the saturation front was parallel to the bottom surface and it moved uniformly to the top of the sample. Wulff & Mjaaland (2002) used ultrasonic wave transmission and reflection to monitor the displacement of a saturation front within a sandstone block. The velocity, amplitude and frequency of the transmitted waves, from "source" at the top of the block to "receiver" at the bottom of the block, decreased with increasing volume of water (more saturated block). The continuous monitoring of the reflected waves was capable of detecting the moving front and confirmed that seismic surveying is a reliable method to monitor saturation fronts. Monsen & Johnstad (2005) injected gas at constant pressure into an oil-saturated sample while monitoring P-waves. Dispersion was most pronounced at the beginning of the injection and there was a significant decrease of acoustic velocities within only 20% of gas saturation. Lei & Xue (2009) measured ultrasonic velocities and attenuation during the injection of CO_2 into a water-saturated sandstone. Seismic tomography based on normalized velocities and attenuation coefficients enabled mapping CO_2 migration and water displacement. Lebedev et al. (2013) injected supercritical CO_2 ($scCO_2$) and brine on shaley sandstones to study the effect of the presence of these fluids in the acoustic response. A decrease on P-wave velocities was observed when $scCO_2$ was injected in brine-saturated samples. No noticeable changes were observed between the dry and CO_2 flushed samples revealing that the samples did not go through considerable structural damage when the $scCO_2$ was injected.

X-ray Computed Tomography (CT) has its origin in medical applications but it has become a resourceful tool in vast fields of Geosciences, for example, in

investigating fluid flow, soil transport, sediments characterization, and soil and pore-space morphology. For a list of applications see Ketcham & Carlson 2001 and Mees et al. 2003.

Several experiments using X-ray CT to study fluid distribution have been performed. Garg, Zwahlen & Patzek (1996) performed water imbibition in a dry sandstone and the saturation front was imaged through X-ray CT. A positive correlation between water imbibition and weight gain of the sample was established. Akin et al. (2000) used X-ray CT to study spontaneous water imbibition in a diatomite (in air-water and oil-water systems). The CT scans provided information about fluid displacement patterns, more particularly, the mobility of the saturation front. Through the time-space evolution of this interface, it was possible to conclude that in spite of a very low permeability, the diatomite had enough well connected flow pathways to allow a fast water imbibition. Rangel-German & Kovscek (2002) performed forced imbibition at different injection rates in fractured porous media in order to study the influence of different fracture apertures on fluid flow. X-ray CT scans helped localize saturation fronts and preferential fluid flow paths. Hirono, Takahashi & Nakashima (2003) used X–ray CT imaging to study the dependence of fluid flow properties with deformation mechanisms on fault-related rocks. Direct visualization of the scans showed that the fault zone without cataclasis acted as a fluid conduit whereas the fault zone with cataclasis (or mineral precipitation) acted as a barrier consolidating the idea that fractures dramatically influence fluid patterns and rates of flow. Meleán, Broseta & Blossey (2003) used X-ray CT scanning to analyse the dispersion of saturation fronts at various injection rates and found experimentally that low and high injection rates correspond to diffusive and sharp saturation fronts, respectively. Schembre & Kovscek (2003) used X-ray CT to compute two-phase relative permeability curves from experiments of spontaneous imbibition (water-oil and water-air) in sandstones. Through the CT scans, saturation profiles along the length of the samples were plotted and the relative permeability was estimated. Tang & Kovscek (2011) injected water into an oil-saturated sandstone at various injection rates. X-ray CT imaged the fluid displacement and the growth of fingering in the water/oil interface.

The aforementioned works provide insight into solid/fluid interactions solely based on X-ray CT scanning but no acoustic waveforms were acquired during the

imbibition. Matching the acoustic response with the evolution of fluid saturation provides additional ways of analysing solid/fluid interactions that occur during imbibition. X-ray CT complements the acoustic data with an image of the fluid‘s distribution, displacement and geometry of the saturation front. Very few laboratorial experiments used image visualization and acoustic monitoring methods simultaneously. Monsen & Johnstad (2005) designed an acoustic sample holder that was transparent to X-rays. 3D images were reconstructed from the scans and velocity-saturation relationships were established thus linking qualitative and quantitative measurements. Lebedev et al. (2009) performed forced water imbibition into a sandstone at different injection rates. P- and S-waves were recorded while the sample was scanned. Velocity-saturation relationships were found and complemented with fluid distribution images. A sudden increase of the P-wave velocity is observed at 60% of water saturation matching the moment the random distribution of patches started to coalesce in bigger clusters. Nakagawa et al. (2013) conducted measurements of seismic properties of sandstones during super critical CO_2 injection using a resonant bar technique. Fluid saturation and distribution in the rock cores were determined using X-ray CT scans. Different velocities and attenuation were observed for different $scCO_2$ distribution within the cores. Moreover, significant decrease in the velocities of saturated samples indicated strong sensitivity of the rock’s frame stiffness to pore fluid.

Though it is known that the presence of fluid, its distribution and flow rate influence the acoustic response (Li, Zhong & Pyrak-Nolte 2001) there is lack of experimental data that backs up these statements. It was the main purpose of this thesis to fill that gap by performing a significant array of experiments that allowed matching an acoustic response to a specific fluid distribution.

4. MOTIVATION & GOALS

Accurate analysis of seismic data can make all the difference when extracting reservoir information. The injection of fluids reflects changes of saturation and pressure in the reservoir and time-lapse seismic technologies are used to map these changes in space and time. To allow a correct estimation of saturation levels, quantitative relationships between fluid saturation and seismic characteristics (for example, velocities of acoustic waves, elastic parameters and effects of dispersion and attenuation) need to be established. However, **there is a considerable lack on input parameters aimed at assessing the physical behaviour of rocks in multi-phase flow conditions. This thesis intended to bridge that gap by collecting a significant amount of qualitative and quantitative data and establish relationships between governing parameters like volume of fluid injected, rate of injection and applied pressure with acoustic response, saturation level, displacement and geometry of the saturation front.**

This thesis incorporated an ultrasonic measurement technique, **Active Ultrasonic Monitoring**, together with an image acquisition technique, **X-Ray Computed Tomography (CT)**. Active Ultrasonic Monitoring is a very reliable and non-destructive experimental technique. It can be performed with limited resources, providing good data, without complex processing. X-Ray CT produces a representative dimensional image of the spatial distribution of the fluid (in 2D and 3D). The successive acquisition of CT scans allow following the time-space evolution and geometry of the saturation front. The two aforementioned experimental techniques were combined simultaneously such that X-ray CT scanning was performed while acoustic waves were recorded.

The dependence of the acoustic wave velocities, fluid saturation and distribution at different injection rates was also studied. Sandstones and carbonates were used to compare results of different types of rocks and infer about possible common behaviours. The injection of water and oil also aided in the study of the influence of different fluids (different densities) in the pattern of fluid saturation and in the evolution of acoustic wave velocities. The experiments were done at ambient conditions of pressure and temperature and also under confining pressure. The acoustic-saturation relationships analysis was complemented with (1) studying the

influence of capillary and gravity forces in the fluid distribution and acoustic response by positioning the sample vertical and horizontal, i.e. with the direction of injection parallel and perpendicular to the gravity vector, respectively; and (2) inferring about pore network properties (distribution and interconnectivity of pores) and structural heterogeneity of the samples through the CT scans that might influence the fluid distribution and acoustic response.

In spite of the technological advances and wide range of experiments in Rock Physics, the link between theory (descriptive parameters, physical laws, modelling, etc.) and *in situ* behaviour (and the ongoing problem of upscaling) is always the ultimate but difficult goal that can only be achieved by performing a significant array of laboratorial experiments. In this thesis, the method of simultaneous image acquisition and acoustic monitoring was explored to its fullest, focusing on providing results to establish unequivocal velocity-saturation relationships.

PART I
TESTS AT AMBIENT CONDITIONS

I.1 METHODOLOGY

Laboratory experiments were performed with the purpose of quantifying changes in the acoustic response, fluid saturation and fluid distribution (mainly the geometry and displacement of the saturation front). The experiments consisted on injecting water in dry samples, water *imbibition*, at different injection rates.

Part I, **fluid injection at ambient conditions** of pressure and temperature (without axial or confining pressure applied to the sample), was divided in two cases:

a. Forced imbition at **constant injection rate**. Acoustic-waves and fluid saturation were monitored during water injection without changing the injection rate. I distinguished the cases were the injection rate was high and low when compared to the natural imbibition rate of the sample. This set of experiments was performed in *sandstones* – **Chapter 1**.

b. Forced imbition at **variable injection rat**e. Acoustic-waves and fluid saturation were monitored while the injection rate was decreased and increased in one single fluid flow experiment. This set of experiments was performed in *sandstones* and *limestones* – **Chapter 2**, **3** and **4**.

The samples of interest were reservoir rocks, specifically sandstones from the Otway Basin, Australia, and limestones from Savonnières, France. Otway sandstones are fairly homogenous with porosity ~20% and permeability ranging from 30 to 70 mD. Limestones tend to be heterogeneous rocks, composed by a variety of minerals that contribute to the existence of multi-porosity. However, Savonnières limestones are a rare type of homogenous limestones, composed of 98% calcite, with porosity ~30% and permeability ~90 mD. Both types of rocks have favourable physical properties to perform fluid flow experiments: homogeneous rocks with high permeability. Heterogeneity makes the theoretical and experimental understanding of solid/fluid interactions fairly complex and many theoretical formulations on fluid flow are based in simplified approximations. Therefore, to concentrate the study in pure physical-driven effects, the samples must be as homogeneous as possible, in structure (for example, no fractures) and in mineral composition. The high permeability also allows a fast, continuous flow of

the injected fluid. This is a practical advantage as it reduces the time of experiments due to a fast saturation of the samples.

While sandstones are very much in use in experimental rock physics due to their structural homogeneity and world-wide availability, limestones have sporadically been studied with emphasis on their physical properties when dealing with fluid flow. There are many experimental studies about the thermo-chemical reactions of limestones with fluids (Strand et al. 2008; Noiriel et al. 2009) and on the use of limestones as sorbents in CO_2 storage (for an extensive overview see MacDowell et al. 2010) but not regarding the acoustic response in the presence of fluids. It was part of this thesis to bring new data and knowledge to the study of velocity-saturation relationships on limestones.

The experiments were carried out at the X-ray CT Scanner Laboratory of the Commonwealth Scientific and Industrial Research Organisation (*CSIRO*), in Perth. Figure 6 shows the experimental setup for Part I: a medical X-ray CT scanner, *Toshiba Asteion CXXG-005A*; an injection pump, *Shimadzu LC-20AT*; two pairs of P-wave piezoelectric transducers, *Olympus D7207*; a pulser/receiver, *Olympus 5077-PR*, and an oscilloscope, *Agilent DSO-3202-A*. All the samples were cored in the shape of cylinders from their original blocks (diameter: ~3.8 cm; height: ~7 cm) and then left to dry on open-air. No treatment, thermal or pressure, was done before initiating the fluid flow experiments. The outside surface of the samples was covered by epoxy, thus enforcing a unidirectional flow. Two plastic rings were glued to the top and bottom of the sample. These rings were fixed to a metallic frame attached to the table of the CT scanner to assure that the sample did not move during scanning. Each plastic ring had a hole in the centre: the hole in the top assured that the sample was in direct contact with atmospheric pressure, avoiding pressure build up as the water is injected; the bottom hole was connected to the injection pump (this hole had 0.5 cm of diameter). Grooves were cut in the bottom ring allow an even distribution of water over the base of the sample. This was designed to ensure that during water injection, a planar saturation front is created. However, the inflow was not broadly distributed in the most of our experiments (namely, Chapter 1, 3 and 4). Rather the initial imbition took the form

of a “point injection”. This might have been due to spreading of glue into the groves when the plastic rings were glued to the base of the sample.

The porosity and permeability of the samples were measured using helium gas in the *Automated Porosimeter Permeameter AP-608* at the confining pressure of 500 psi (approximately 3.5 MPa, the lowest measurable pressure with the AP-608). Since the purpose was to monitor the fluid flow between dry and saturated stages (without applied pressure), the end of the experiment was the moment the injected fluid reached the opposite end to the point of injection. For Chapters 1, 3 and 4, the injection was vertical, i.e. the direction of injection was parallel to the gravity vector so the fluid flow was against gravity (Z-direction, against gravity, Figure 6 and 8). In Chapter 2, the sample was horizontal, i.e., the direction of injection was perpendicular to gravity.

During each imbibition, ultrasonic P-waveforms (Figure 7) and X-ray CT scans (Figure 8) were acquired simultaneously. With this procedure, a P-wave velocity was matched to a level of water saturation at several moments of the injection. Also, these quantitative parameters were related to the position and geometry of the saturation front. The red circle in Figure 8 represents the ultrasonically monitored position (the position of the base of transducers) in a XZ scanning plane.

The P-wave velocity was calculated using the first-break pick of the output signal recorded by the oscilloscope (Figure 7) which was triggered manually with the pulser/receiver. Picking the first-break of the output signal can be a difficult process if waveforms are affected by noise or are highly attenuated either due to the sample’s mineralogy or even due to the presence of fluids. This makes the signal-to-noise ratio (SNR) low and a first break difficult to detect. Trial experiments of the methodology presented shown that even when the samples were 100% water saturated, SNR was high enough to detect the first break without ambiguities. Therefore, trends were easier to detect and this picking method was effective.

The transducers had a diameter of 1.5 cm and central frequency 1 MHz. Two pairs of transducers allowed monitoring two positions along the sample’s length: one closer to the point of injection and the other in the middle of the sample. The delay in the P-wave arrival time (due to the electronics of setup, transducers and wires) was calibrated using an aluminium rod, which V_P is well known. The error in calculating V_P, $\sigma(V_P)$ is given by (Taylor 1997)

$$\sigma(V_P) = V_P.\sqrt{\left(\frac{\sigma(D)}{D}\right)^2 + \left(\frac{\sigma(t_P)}{t_P}\right)^2} \quad (20)$$

D is the distance travelled by the P-wave (or the distance between transducers) and $\sigma(D)$ is the error in measuring D. $\sigma(D)$ is constant for all measurements as the distance, D, between the transducers is always the same. t_P is the P-wave arrival time for each P-wave recorded and $\sigma(t_P)$ the error in measuring that arrival time.

The CT scans provided 2D maps of the fluid distribution from which the water saturation was estimated. During each imbibition the sample was scanned along the same axial section without movement of the CT scanner table. The fluid distribution and geometry of the fluid front could be compared relative to the same scanning plane. Note that S_W is a "local" water saturation related to the volume monitored by the P-wave path between pairs of transducers. In practical terms, S_W is averaged over the area limited by the red circle in Figure 8-A.

The study of velocity/saturation relationships was optimized by injecting distilled water in dry samples. In this way, a higher contrast between air and water was obtained and dry and wet zones could be distinguished by direct observation of the CT scans. Another reason for choosing water injection in dry samples relates to the strength of the acoustic signatures. P-wave arrival times between dry and water-filled areas are much more discernible than the ones between water- and oil-saturated areas, for example. Moreover, no chemicals were added to the injected water to increase X-ray absorption. In this way, several experiments were performed on the same sample assuring that there were no significant structural changes (chemical erosions) between consecutive imbibitions. The repeatability of these experiments is crucial so results from several experiments can be compared. Injecting water can be conducive to significant changes in the bulk modulus if the samples contain clay. The clay swells considerably when absorbs water changing the density of the sample and therefore can not be considered to be a constant value. However, the samples used in our experiments did not contain clay and these effects were not present during the fluid flow experiments.

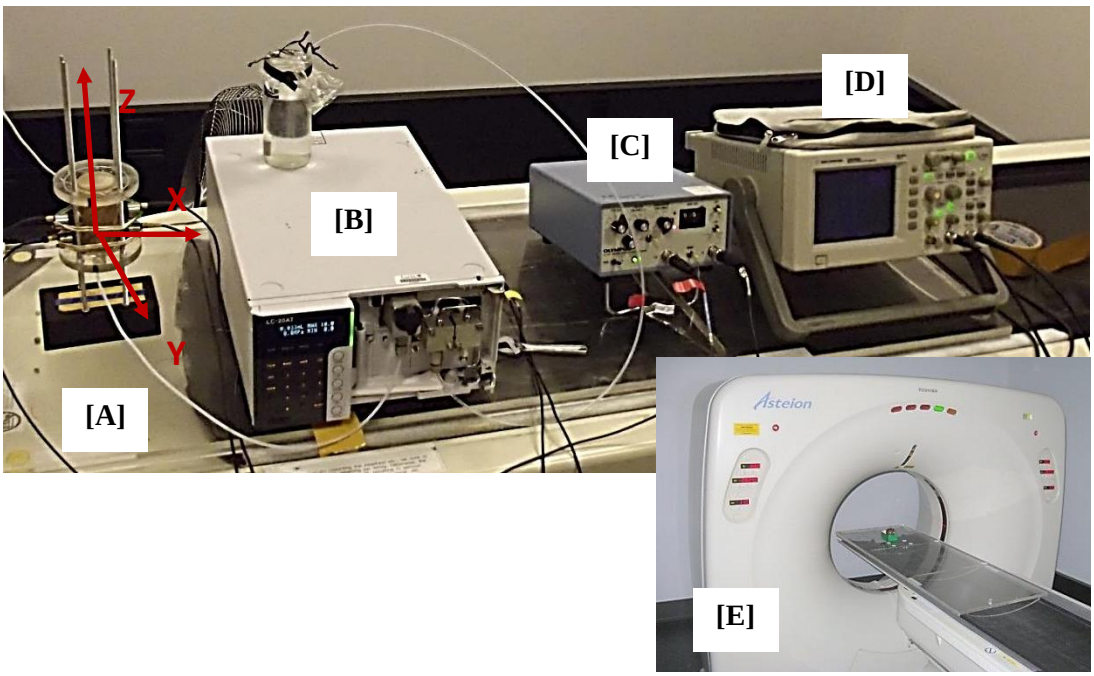

Figure 6 Experimental setup of Part I: **[A]** Sample set for vertical injection (Z-direction); **[B]** injection pump; **[C]** pulser/receiver and **[D]** oscilloscope; **[E]** medical X-ray CT scanner.

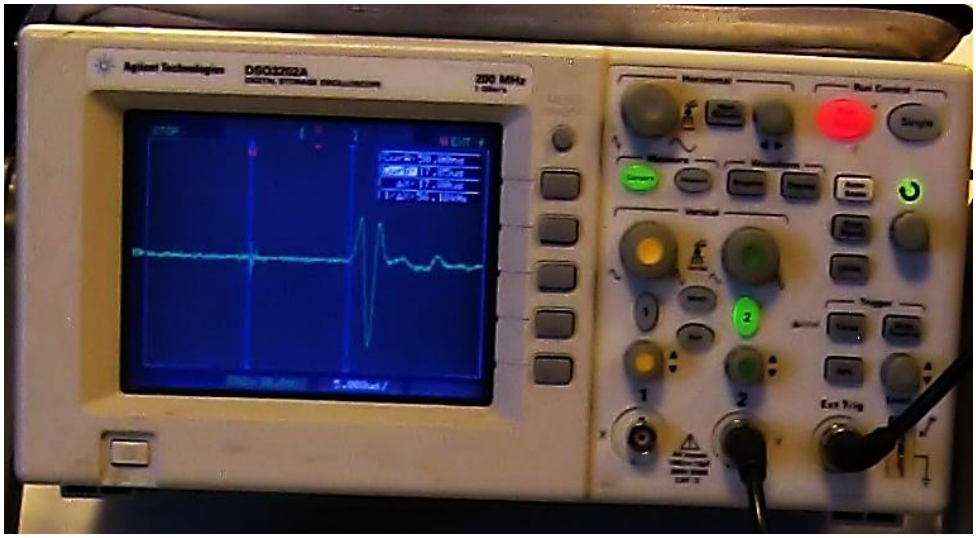

Figure 7 P-wave display on the oscilloscope. The P-wave arrival time can be determined by direct picking of the first break of the output signal.

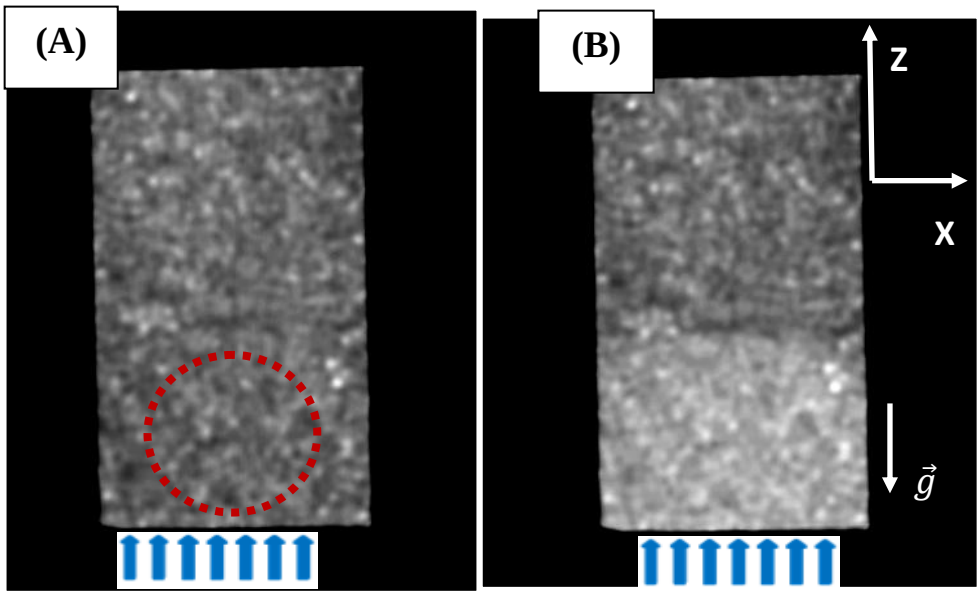

Figure 8 2D CT scans of a sandstone when **(A)** dry and **(B)** after injecting 17 mL of water. The area filled with water becomes "whiter". Blue arrows indicate the direction of injection, opposite to gravity, $\vec{\mathbf{g}}$. Red circle in (A) represents the ultrasonically monitored position covered by the transducers in the XZ scanning plane.

CHAPTER 1
CONSTANT INJECTION RATE: SANDSTONE #1[1]

Forced and natural imbibitions were performed in a reservoir **sandstone** (Otway Basin, Australia) at room temperature with no confining pressure applied to the sample. The sample's main petrophysical properties are shown in Table 1. Distilled water was imbibed into a dry sample with the intention of spotting differences in fluid distribution (evolution of water saturation and geometry of the saturation front) and acoustic response (evolution of ultrasonic P-wave velocities) at different injection rates. The use of distilled water allowed using the same sample for all experiments without inflicting structural damage between imbibitions. P-waves and CT scans were acquired simultaneously at several stages of the imbibition. The sample was in a vertical position, i.e. the direction of injection was parallel to the gravity (Z-direction, against gravity, Figure 9).

Two sets of experiments were performed:

1. At **constant injection rate**.

   The rates of 2 and 0.5 mL/h were chosen. Based on previous experiments performed in our laboratory dealing with fluid flow, 2 mL/h is a high injection rate for this type of sandstone, and 0.5 mL/h is a low injection rate (fast and slow imbibition of water, respectively). Between each experiment the sample was dried in vacuum at 50°C for two days and then left outside for a day to equilibrate with room conditions.

2. Through **natural imbibition**.

   After the forced imbibitions at constant injection rate, the sample dried following the same drying procedure and was prepared for natural imbibition. The sample was placed on top of a water surface allowing a natural uptake of water through the bottom hole.

[1] The main results of this Chapter were gathered in a manuscript accepted for publication in the book "Sandstone: Geochemistry, Uses and Environmental Impact" by Nova Science Publishers. It is presently being printed:
https://www.novapublishers.com/catalog/product_info.php?products_id=46435&osCsid=6f727d78014c0457a4ad20826b4a24fe

The temporal evolution of the P-wave velocity and water saturation at different injection rates as well as CT scans depicting the displacement and geometry of the saturation front for each imbibition are presented in Section 1.1. In Section 1.2, these results were discussed with the focus on relating the P-wave velocity to a fluid saturation and a specific fluid distribution. An attempt was made to link those changes to pore-scale phenomena. In Section 1.3, the most important experimental results were outlined.

OTWAY SANDSTONE #1	
Length (cm)	**6.33**
Diameter (cm)	**3.80**
Porosity (%)	**19.5**
Pore Volume (mL)	**14.0**
Permeability (mD)	**25.0**

Table 1 Main petrophysical characteristics of the Otway Sandstone #1.

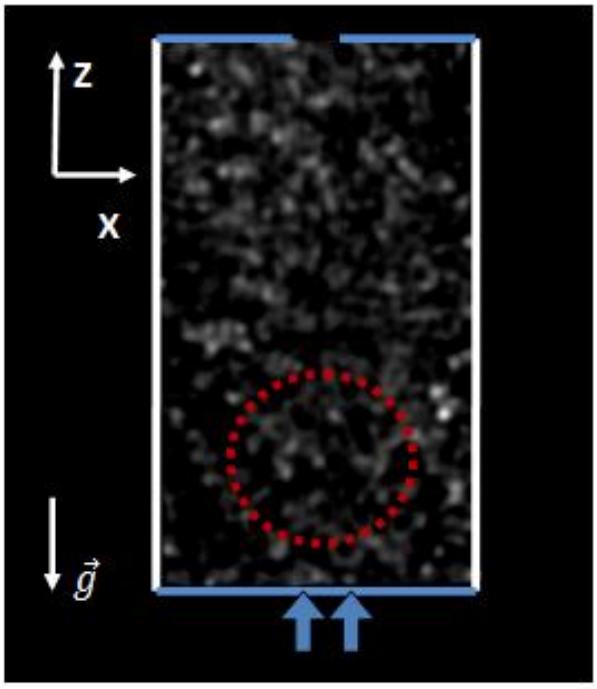

Figure 9 CT scan of the sample when dry in the XZ scanning plane. The surface of the cylindrical sample is covered by epoxy (represented by the white lines). Two plastic rings (blue lines) were glued to the top (with an open end) and to the bottom (with a connection to the injection pump, blue arrows). $\vec{g}$ represents the gravity vector. Red circle represent the area covered by the transducers.

1.1 RESULTS

1.1.1 HIGH & LOW INJECTION RATES

Figure 10 shows the waveforms of the P-waves recorded when the sample was dry and when 1 and 4 mL of water was injected at the injection rate of 2 mL/h. Within two hours of injection, the P-wave amplitude decreased considerably. Changes in the P-wave arrival time were also observed. At 4 mL of injected water (after 2 hours of injection), the P-wave arrival time decreased significantly resulting in an increase of the P-wave velocity, V_P, of almost 170 m/s from when the sample was dry.

Figure 11 shows the evolution of V_P and water saturation, S_W, with the duration of injection for the high injection rate (HIR) of 2 mL/h (Figure 11-A), and for the low injection rate (LIR) of 0.5 mL/h (Figure 11-B). Note that the HIR and LIR were performed on the same sample with just a drying process in between imbibitions.

Both V_P and S_W evolved in the same manner for each fluid flow regime: a sharp increase in the HIR and a much slower increase in LIR as the saturation front entered the ultrasonically monitored position. In more detail:

1. **HIR**: after an initial decrease of V_P during the first hour, V_P increased 200 m/s within 2 hours (at a rate of 100 m/s/h) reaching the maximum value of 2190 m/s. This was followed by an almost constant evolution. S_W followed the same pattern: a sharp increase 1 hour after the beginning of the experiment. S_W increased 60% within the first 3 hours of injection. This sharp increase was then followed by a slow but steady increase, up to the maximum value of 66%.
2. **LIR**: the evolution of V_P and S_W was much more gradual if compared to the HIR case. V_P only started to increase 4 hours after the beginning of the imbibition, at the slow rate of 40 m/s/h. S_W increased to less than 50% within 8 hours of injection. No CT scans were acquired during the last 2 hours of the imbibition due to technical issues with the medical CT scanner but the imbibition was not stopped. S_W is expected to keep increasing continuously and slowly as seen for V_P.

The evolution of V_P and S_W is intrinsically related to the position of the saturation front and its geometry. This can be verified by direct inspection of the CT scans. Figure 12 shows the advancement of the saturation front for 1, 2 and 4 mL of water injected during the HIR (Figure 12-A) and the LIR (Figure 12-B). The HIR sustained an almost flat, compact saturation front throughout the imbibition (indicated by the yellow dashed line in Figure 12-A). Though there was an initial curvature of the saturation front prompted by the point injection (data not shown), it soon became an almost flat saturation front. This initial curvature persisted in the LIR for at least 4 hours (yellow dashed line in Figure 12-B for 2 mL). However, at 4 mL, the saturation front was considerably flatter (Figure 12-B).

The change in CT numbers (ΔCT) with the sample's height (Z-direction) as water is injected is shown in Figure 13. Figure 4 in section *2. CT Image Processing* explains how the CT numbers were computed. Specifics of the geometry of the saturation front were inferred through Figure 13 for each injection rate. In particular:

1. The sharp decrease of ΔCT (down to zero) after 1, 2 and 4 mL of injected water at the HIR characterizes a steep, piston-like saturation front. Conversely, the slow decrease at LIR characterizes a more diffusive saturation front. Compare: for 1 mL of water injected (blue line), ΔCT = 160 is at 12 mm for HIR (Figure 13-A) while for LIR is at 18 mm (Figure 13-B);
2. The height of the saturation front tended to be farther up for the LIR as the imbibition progresses. For example, after injecting 4 mL of water (green line), the saturation front is at 28 and 35 mm for the HIR and LIR, respectively. This means that the same volume of water injected occupied a larger pore volume in the LIR case, characteristic of a more diffusive distribution of water. This is visible in the intense white in HIR at 4 mL when compared to LIR (less bright) for the same volume (Figure 12).

It is important to note that in Figure 13-B, the plots for 1 mL (blue line) and 2 mL (red line) of water injected are relatively close together when compared to the same colour lines in Figure 13-A. This is due to the fact that between 1 mL and 2 mL the water spread laterally before it started advancing in the height (Z-direction)

(see the increase in radius of the yellow dashed line between 1 and 2 mL in Figure 12-B).

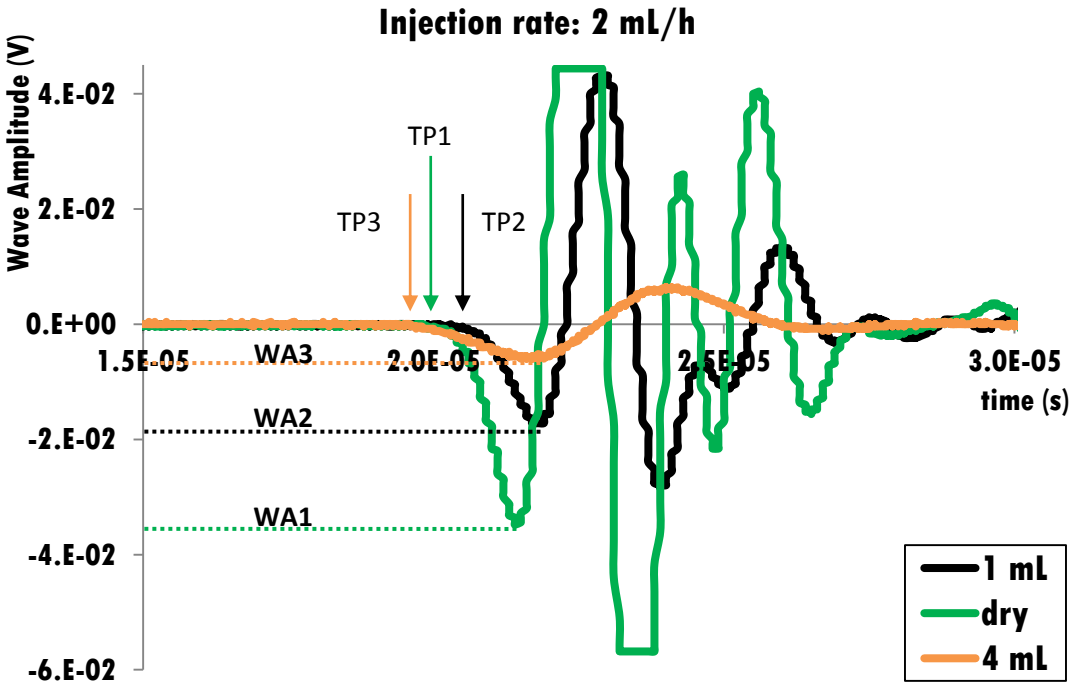

Figure 10 Waveforms for dry sample, 1 and 4 mL of water injected at the injection rate of 2 mL/h. Note the decrease in wave amplitude (from WA1 to WA2 to WA3) and the changes in the P-wave arrival time (increase from TP1 to TP2 and decrease to TP3) as water is continuously injected.

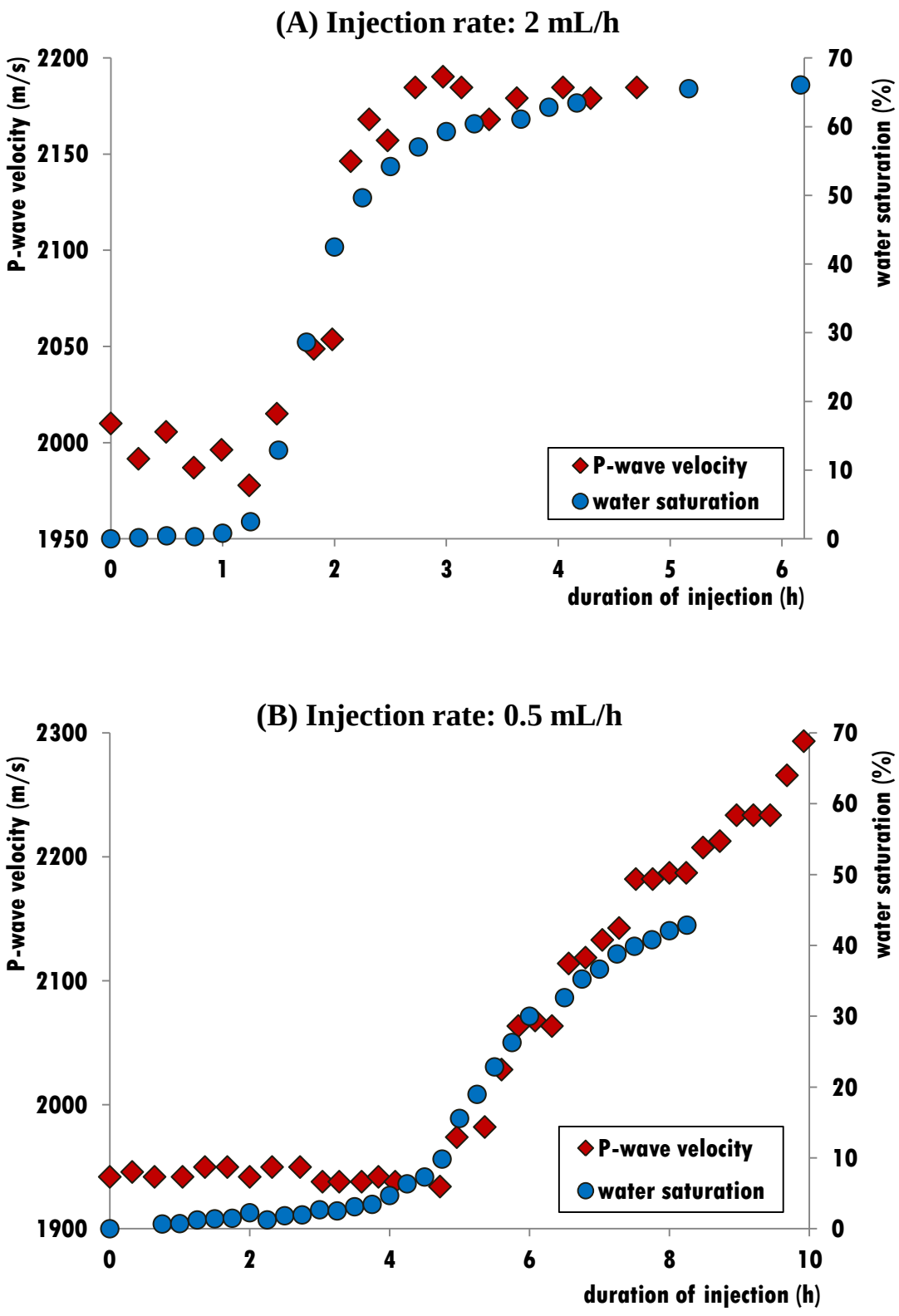

Figure 11 P-wave velocity and water saturation with duration of injection for the **(A)** 2 mL/h (high injection rate) and **(B)** 0.5 mL/h (low injection rate). No CT scans were acquired after 8 hours in (B) but the injection did not stop.

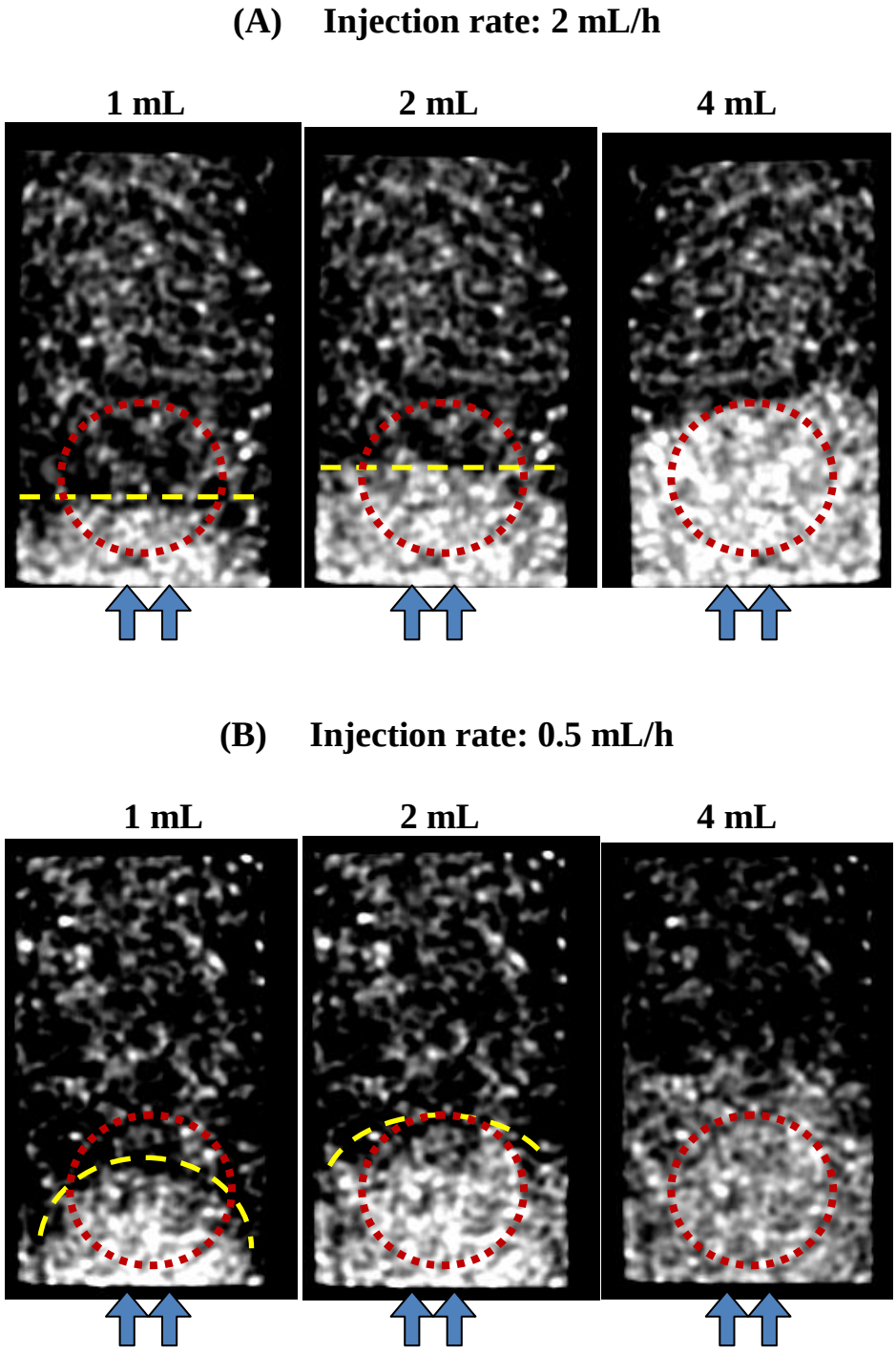

Figure 12 CT scans for 1, 2 and 4 mL of water injected for **(A)** 2 mL/h (high injection rate) and **(B)** 0.5 mL/h (low injection rate). More "white" indicates higher water saturation. Note in (A) a flat saturation front in all moments while in (B) there is a progressive lose of curvature as more water is injected (yellow dashed lines). Blue arrows indicate direction of injection. Red circles represent the area covered by the transducers. All injections were performed on the same sample.

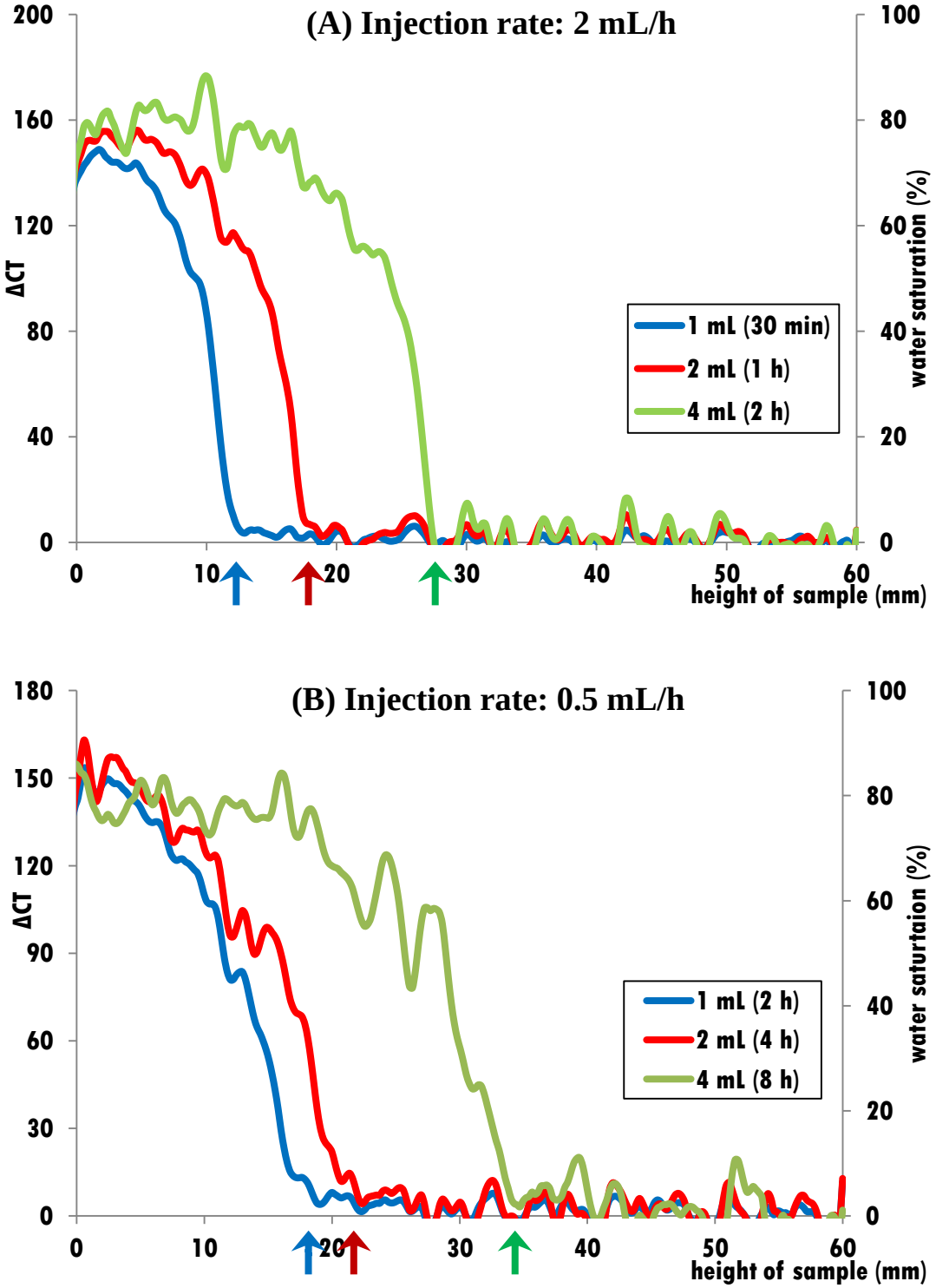

Figure 13 Variation of CT numbers, ΔCT = CT(w) − CT(dry), and water saturation with height of the sample, for the **(A)** 2 mL/h (high injection rate) and **(B)** 0.5 mL/h (low injection rate). Not that for the same amount of volume of water injected, the saturation front is farther up for the low injection rate than for the high injection rate (see coloured arrows).

1.1.2 NATURAL IMBIBITION

The evolution of V_P and S_W for the HIR and LIR experiments was compared to the evolution of those two parameters when performing natural imbition (NI). In this way, the NI rate could be classified as a low or a high injection rate.

S_W was estimated through the volume of water imbibed. The volume of water imbibed is usually estimated by weighing the sample with a scale at several stages of the imbibition (Li & Horne 2010). However, this method cannot be applied to this experiment because of the continuous X-ray CT scanning. All the experimental setup that sits inside the CT scanner ring must be metal-free as X-ray/metal interactions blur the CT scans. Therefore, the total volume of imbibed water was estimated by comparing the CT scans of the dry sample with the consecutive scans of the partially water-saturated sample. $\overline{\mathrm{CT}_{\mathrm{dry}}}$ is the average CT number of the dry sample and $\overline{\mathrm{CT}_2}$ is the average CT number at the following moment. $\overline{\mathrm{CT}_2}$ is a superposition of the CT number for water, $\mathrm{CT_w}$, air, $\mathrm{CT_{air}}$, and $\overline{\mathrm{CT}_{\mathrm{dry}}}$. The contribution of each phase (water, air and dry matrix) is weighed over the sample's volume, V. Thus $\overline{\mathrm{CT}_2}$ is given by

$$\overline{\mathrm{CT}_2} = \frac{\mathrm{V_{H_2O}CT_{H_2O}} + \mathrm{V}\overline{\mathrm{CT}_{\mathrm{dry}}} - \mathrm{V_{H_2O}CT_{air}}}{\mathrm{V}}. \tag{21}$$

Rearranging Equation 21 and noting that for a medical CT scanner $\mathrm{CT_{H_2O}} = 0$ and $\mathrm{CT_{air}} = -1000$, the volume of imbibed water, $\mathrm{V_{H_2O}}$, is

$$\mathrm{V_{H_2O}} = \frac{\overline{\mathrm{CT}_2} - \overline{\mathrm{CT}_{\mathrm{dry}}}}{1000}\mathrm{V}. \tag{22}$$

It is assumed that the pores previously dry are totally filled with water.

The NI rate was estimated by dividing the imbibed water volume by the time interval. The height used to calculate the water-filled volume for each moment was measured directly in the CT scans.

Figure 14 shows the evolution of the estimated imbibition rate and volume of water imbibed with the duration of the imbibition. No CT scans were acquired

between 1 and 3 hours due to technical issues with the medical CT scanner but the injection was not stopped. Two phases are easily distinguished in Figure 14: the initial phase A is characterized by a sharp decrease (increase) in the NI rate (volume of water imbibed) and phase B is characterized by a slowing down of the decrease (increase) of the NI rate (volume of water).The initial fast imbibition slowed down by almost 70% in 1 hour, comparable to an exponential decay. Note, however, that the calculated NI rate is an overestimation. For example, in phase (B), 3 mL of water was imbibed over 3 hours, resulting in a rate of approximately 1 mL/h. The estimated NI rate falls between 2 and 1.5 mL/h (Figure 14). This difference is due to the fact that the pore volume was assumed to be fully saturated with water which was not the case (S_W = 100% is never reached during the natural imbibition). Therefore, the volume of water imbibed is overestimated and, consequently, the imbibition rate. However, the evolution reflects an expected trend: slowing down of the natural imbibition rate as the saturation front advanced in height.

Figure 15 shows the evolution of V_P and S_W for the NI experiment. The trend observed in the evolution of those two parameters is also observed on Figure 11-A for the HIR case: a sharp increase of V_P and S_W and fast stabilization within 1 hour. The similarities in the time-evolution of V_P and S_W between the injection rate of 2 mL/h (HIR, Figure 11-A) and the NI (Figure 15) means that the rate of 2 mL/h is actually not as high as it was initially thought. To accurately establish the time-evolution of V_P and S_W at a high injection rate, an additional forced imbibition experiment was performed at the injection rate of 5 mL/h. Figure 16 shows the resulting time-evolution of V_P and S_W. Though the maximum values reached in V_P were similar between Figure 11-A and Figure 16, $V_P = 2150$ in Figure 11-A was reached after 2h of injection while the same value was reached in Figure 16 within 1h. Stabilization of V_P and S_W was reached sooner which was expected since the saturation front was pushed "faster". Also a flat saturation front was sustained throughout the forced imbibition. This can be seen in the CT scan in Figure 16 and through the steep decrease of ΔCT (at around 30 mm of height), characteristic of a flat saturation front. However, only a maximum S_W of 43% was reached.

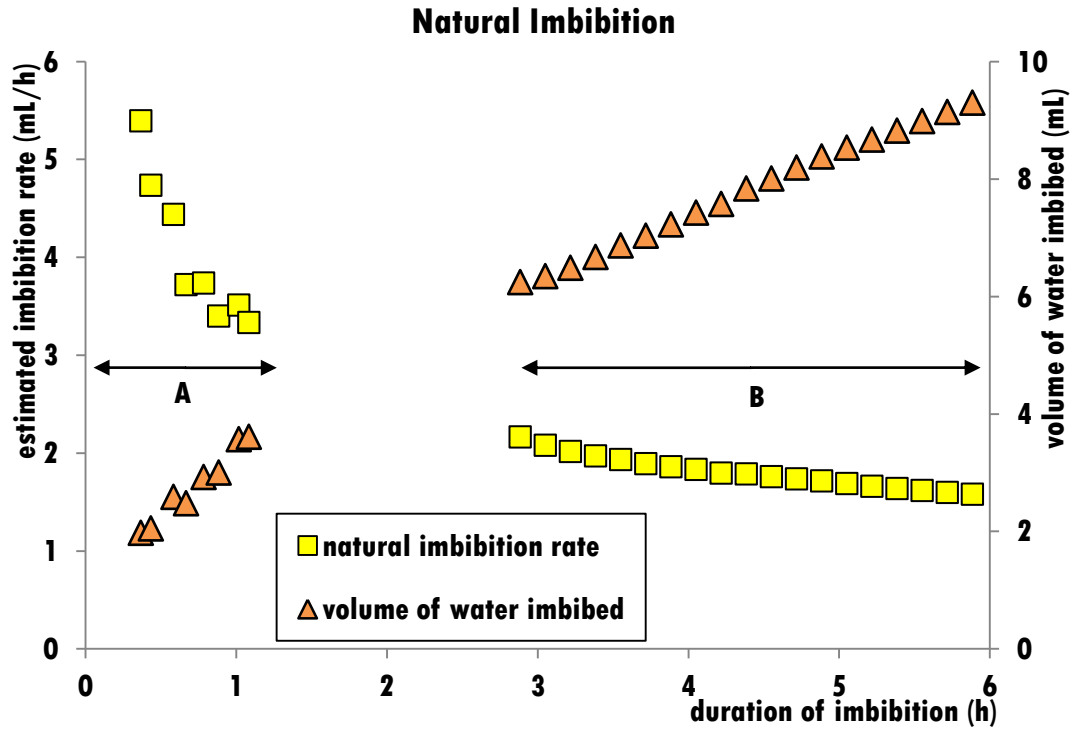

Figure 14 Imbibition rate and volume of water imbibed during the natural imbibition. Note the decrease of the imbibition rate similar to an exponential decay, initially dominated by capillary effects (A) and followed by a phase dominated by gravity (B). No CT scans were acquired between 1 and 3 hours.

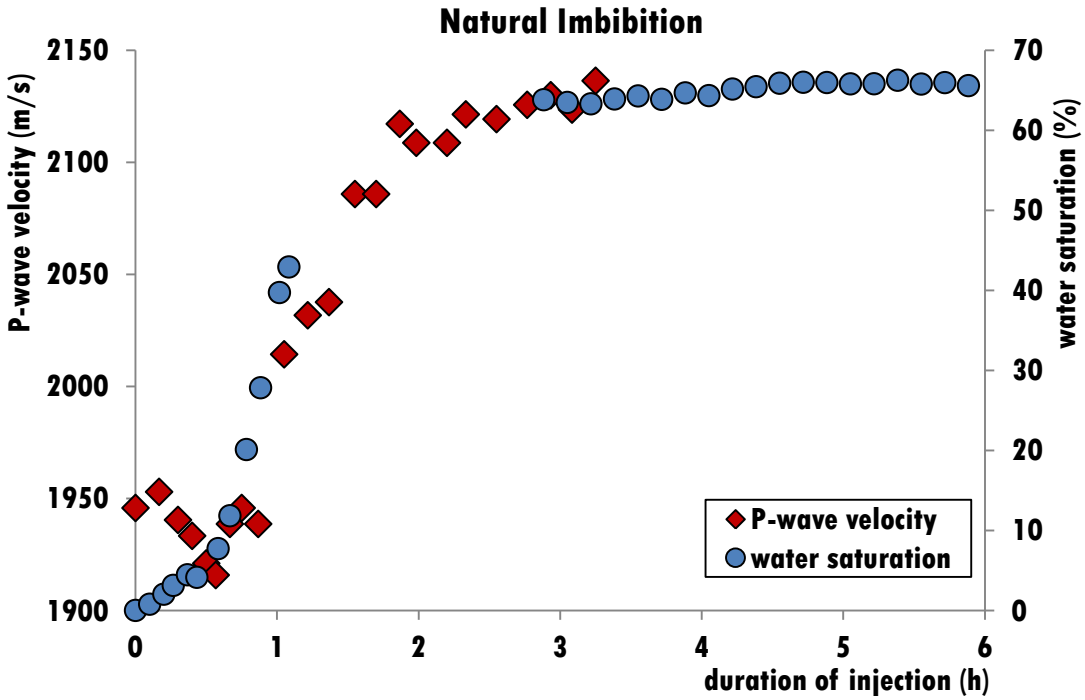

Figure 15 P-wave velocity and water saturation with duration of injection for the natural imbibition. Note the similar pattern to Figure 11-A. No CT scans were acquired between 1 and 3 hours but the injection was not stopped.

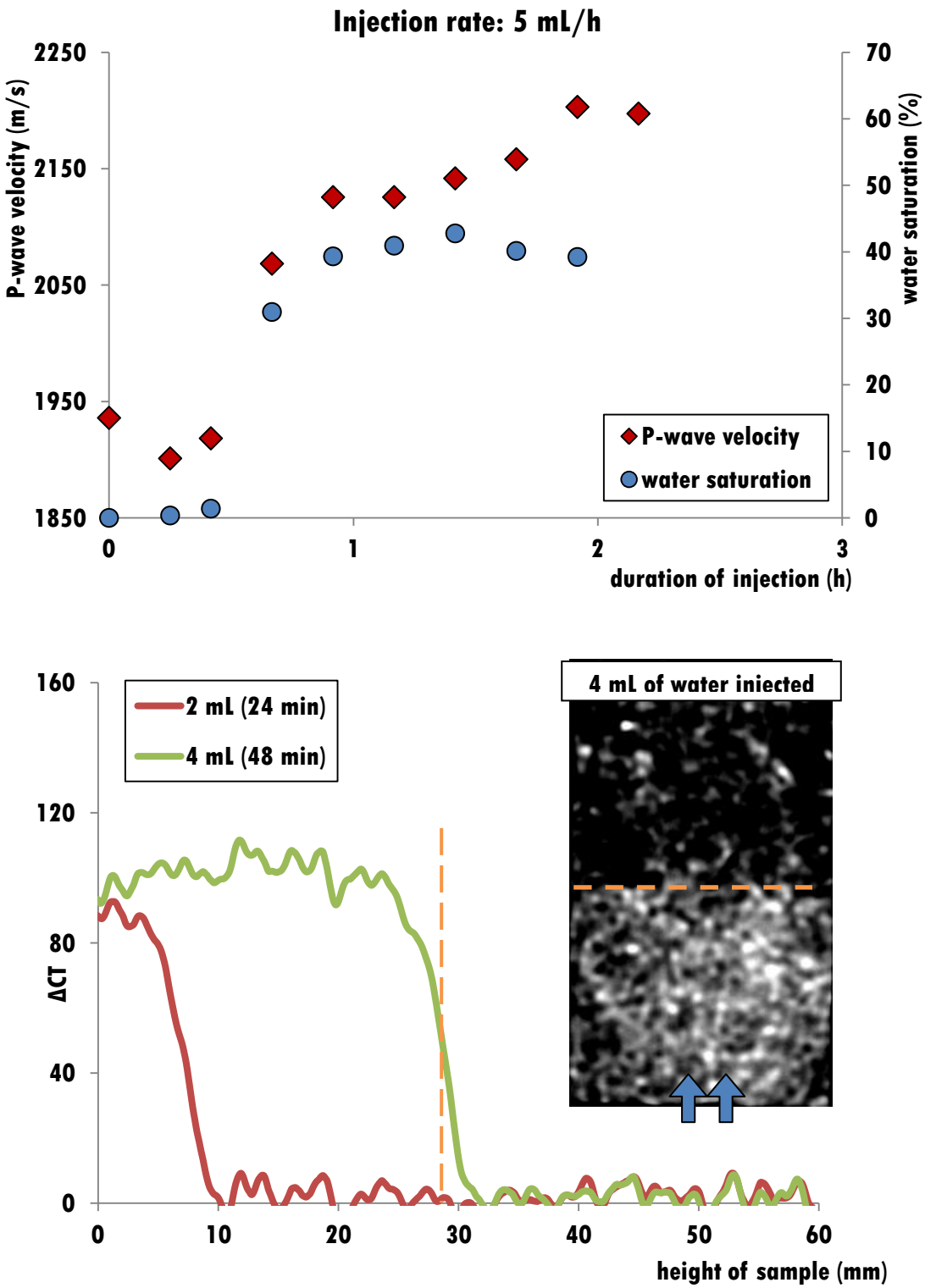

Figure 16 (Top) P-wave velocity and water saturation with duration of injection for the injection rate of 5 mL/h. **(Bottom)** Variation of CT numbers with height of the sample for 2 and 4 mL of water injected. Note the steep slope of ΔCT, characteristic of a flat saturation front as confirmed by the CT scan (orange dashed line), at ~30 mm. Blue arrows indicate direction of injection.

1.2 DISCUSSION

A decrease on P-wave amplitude is observed as soon as water enters the monitored position. Wave attenuation may be induced by trapped fluids and residual saturation in the porous media that causes a local discontinuous phase (Rubino & Holliger 2013; Steeb et al. 2011). Locally there is a mixture of two-phase fluids, water and trapped air that causes a progressive decrease in the P-wave amplitude that persisted with the continuous injection (since the sample was always in partially saturated conditions).

The first drop in V_P seen in Figures 11-A, 16 and 16-Top is related to the approaching saturation front. This velocity reduction is interpreted as a *moisture weakening effect*. The capillary pressure assumes its highest value at low S_W, i.e. at the beginning of the imbibition (Riaz et al. 2007). And therefore, water is able to propagate easily without the assistance of external forces. Ahead of the saturation front there is a small fraction of water (moisture) advancing. This moisture can cause a weakening of the matrix. This reduces the effective bulk modulus and, as a direct consequence, V_P decreases (as established by the Gassmann-Wood, GW, theory). This drop is consistently observed on the imbibitions initiated at high rates but not in the low rate (0.5 mL/h). During the low injection rate, the displacement of the saturation front is slow enough to create equilibrium between neighbouring grains. After the initial drop V_P started increasing steeply and continuously. Here, the increase in water saturation set the necessary conditions for the effective bulk modulus to increase and overcome the weakening effect triggered by the moisture. As a direct consequence V_P increases (GW theory) (Mavko, Mukerji & Dvorkin 2009; Toms et al. 2006). This increase continues until the maximum S_W is reached.

Experimental data suggests that the higher injection rate of 5 mL/h is not the most efficient in displacing the residual fluid (in this case, air). The relatively low value of the final S_W = 43% indicates that many gas bubbles were trapped behind the advancing saturation front. This means that the water does not completely displace the gas from the pores and part of it remains trapped. This is supported by microscopic examination studies showing that the residual gas is surrounded by water and it is unable to escape by ordinary flow (Katz et al. 1966). This is because high rates do not allow enough time for the wetting phase (water) to contact with

the matrix and pore structure for an efficient imbibition. Conversely, the injection rates equal to or lower than the natural imbibition rate lead to a higher S_W, thus providing a more efficient way to displace the residual fluid.

Natural imbibition processes are the result of an ongoing interplay between gravity and capillary forces. These two forces are always present during imbibition processes but one can overcome the other. During vertical imbibition, it is possible to distinguish these forces: initially, the flow is dominated by capillary forces (characterized by a fast imbibition of water), followed by a second stage when the process changes from capillary driven to capillary-gravity driven flow. At this stage, gravity causes a considerable slowdown of the imbibition rate (segregating the flow) but capillary forces are still strong enough to force a slow but continuous flow (Karimaie & Torsaeter 2007).

1.3 CONCLUSIONS OF CHAPTER 1

Laboratory-scale experiments were performed in order to quantify the influence of the injection rate on the evolution of ultrasonic P-wave velocities and water saturation and relate these quantities to the geometry and displacement of the saturation front. The X-ray CT scanning allowed not only a visualization of the saturation front but also provided data to estimate water saturation during each forced injection. The CT scans also provided data to estimate the volume of water imbibed during the natural imbibition and its rate.

The saturation front passing the ultrasonically monitored position was detected through the change in the evolution of the P-wave velocity. This change was characterized by a sudden increase in the P-wave velocity, much sharper for the high injection rate but still noticeable for the low injection rate. The rate at which the P-wave velocity changed was intrinsically related to the type of saturation front: sharp and straight for the high injection rate and dispersive for the low injection rate. The pattern of the evolution of the P-wave velocity mimics the evolution of the water saturation. This result implies that it is possible to continuously and actively monitor saturation fronts through the analysis of the acoustic response and also infer about its geometry.

It was also found that that an injection rate higher than the natural imbibition rate was not efficient in the production of the residual fluid, whereas an injection rate close to the natural imbibition rate was the most efficient. A low injection rate was also efficient in displacing the residual fluid but only over a long period of time. Residual saturation is related to the dynamics of the multiphase flow and will invariably affect seismic-wave propagation (Li, Zhong & Pyrak-Nolte 2001).

Another important outcome of this study was that the same water saturation was related to different P-wave velocities. Acoustic wave propagation appear to be very sensitive to spatial fluid distribution more than to the actual water saturation level (Cadoret, Mavko & Zinszner 1998). Specially, the presence of patchy saturation (fluid clusters at the macroscopic scale) influences how acoustic waves propagate and interact with porous media by creating significant acoustic attenuation and dispersion (Li, Zhong & Pyrak-Nolte 2001; Müller, Gurevich & Lebedev 2010).

CHAPTER 2
VARIABLE INJECTION RATE: SANDSTONE #2[2]

The study of the influence of flow rate in the evolution of V_P and S_W was continued but this time in a different Otway **sandstone.** Its homogeneity and well known mineralogy makes this type of sandstone ideal for fluid flow experiments. The petrophysical properties of the sample are shown in Table 2. Its composition is 90% sandstone and 10% interbedded claystone and coal. This sandstone has similar petrophysical properties to Sandstone #1 but with higher permeability. Again, distilled water was forced by the means of an injection pump into a dry sample. The fluid flow experiment was performed at room temperature and atmospheric pressure. This time, the injection rate was changed during the imbibition. The injection started at a high injection rate (HIR), 5 mL/h, and was kept for approximately 3 hours. Then the injection rate was decreased to a low injection rate (LIR), 0.1 mL/h, and kept constant for approximately 26 hours. Then, the injection was stopped for 16 hours. The injection was restarted at the HIR of 5 mL/h and kept constant for approximately 4 hours (Figure 17). P-waves were acquired by a pair of transducers glued to the walls of the sample, close to the entrance of water (Figure 18-A**).** Note that though Figure 18-A shows two pairs of transducers glued to the sample, only the pair on the right was active. There was no point injection and the water distributed over the whole base of the cylindrical sample. CT scans were acquired simultaneously always in the same scanning plane which resulted in 2D maps of the sample (Figure 18-B). The sample was in a horizontal position, i.e. the direction of injection was perpendicular to the direction of gravity. This chapter is organized as follows. In Section 2.1, the temporal evolution of the P-wave velocity and water saturation is presented and discussed. The CT scans were analysed to extract information about fluid distribution and geometry of the saturation front. In Section 2.2, the most important results of this fluid flow experiment are discussed and related to pore-scale phenomena. Section 2.3 concludes this chapter by

[2] The main results of this Chapter were published in Geophysical Prospecting, n. 60, pages 572–580, 2012. See Appendix B for the published version.

pinpointing the implications of the results on the present knowledge of velocity-saturation relationships in rocks.

OTWAY SANDSTONE #2	
Length (cm)	**7.43**
Diameter (cm)	**3.80**
Porosity (%)	**16.7**
Permeability (mD)	**66.7**

Table 2 Main petrophysical characteristics of the Otway Sandstone #2.

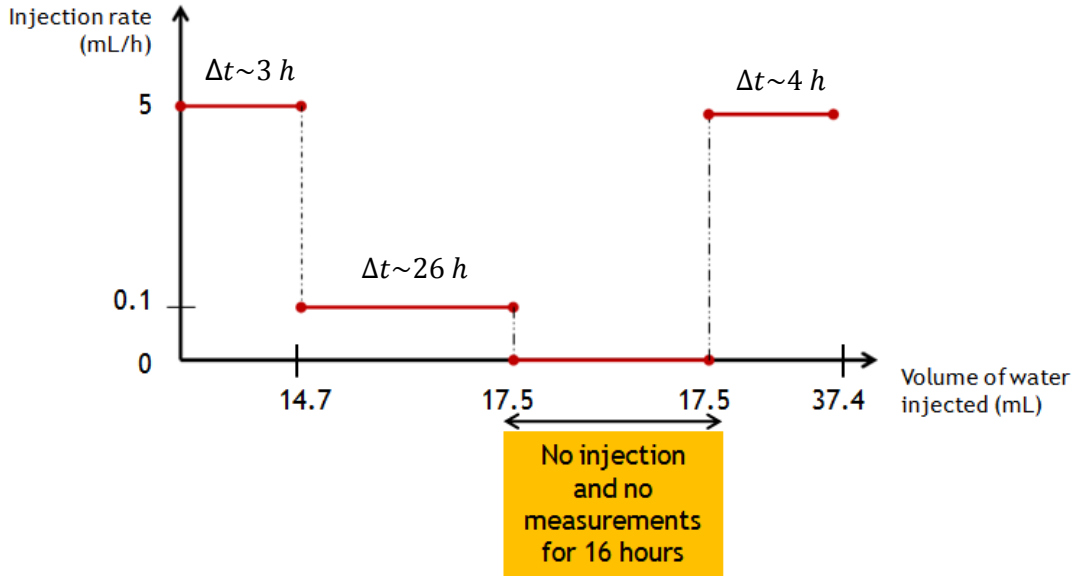

Figure 17 Time-frame for the fluid flow experiment of the Otway Sandstone #2, total volume of water injected and injection rates.

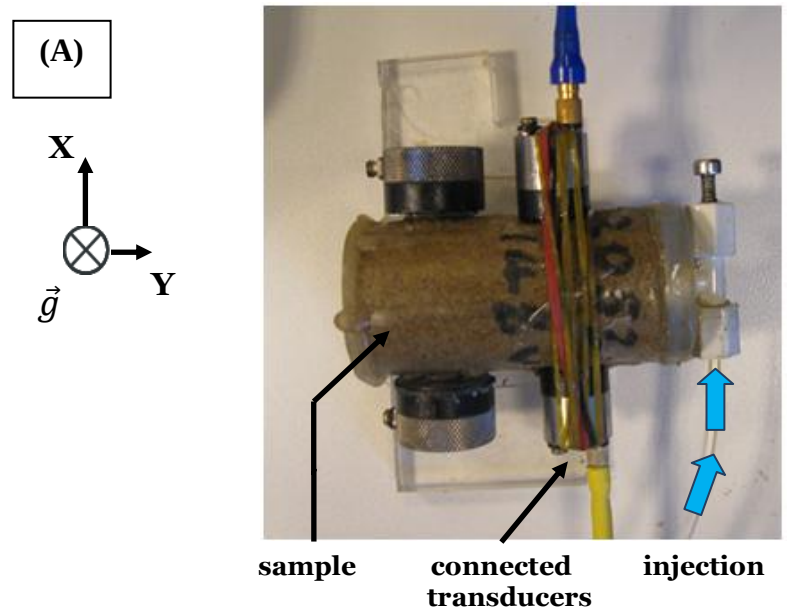

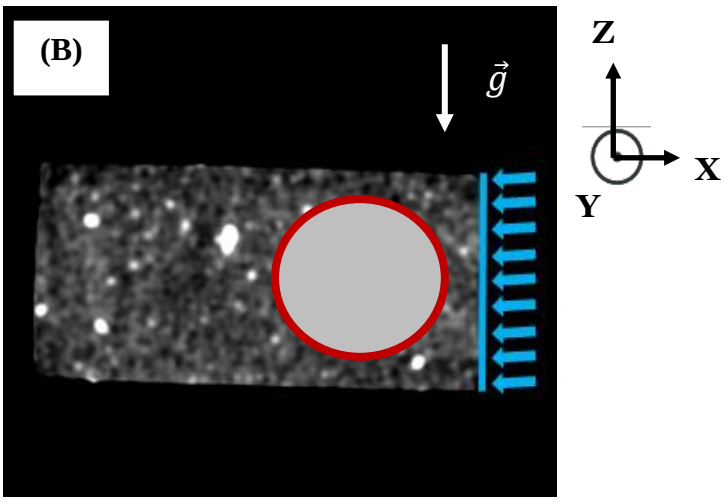

Figure 18 (A) Sample set for horizontal injection with connected transducers. **(B)** CT scan of the dry sample. Red circle marks the position of the transducers on the XZ scanning plane. Blue arrows indicate direction of injection.

2.1 RESULTS & DISCUSSION

2.1.1 GEOMETRY OF THE SATURATION FRONT

Figure 19 shows different CT number profiles for 15 and 17 mL of water injected at the HIR of 5 mL/h and LIR of 0.1 mL/h, respectively. Note the sharp decrease of the CT number at 50 mm for the HIR representing a straight displacement of the saturation front (orange dashed line) while the LIR profile was much broader, ending at 20 mm (green dashed line). Information about the geometry of the saturation front was obtained by comparing the CT scans of Figure 20 (in a black and white configuration, result of the digital process described in Figure 5) with the CT profiles in Figure 19. More particularly, at the HIR, the saturation front is flat mimicking a piston-like displacement of fluid (Figure 20-A). At the LIR, the saturation front is now curved (Figure 20-B). It is known that the flow rate has a significant impact on immiscible-phase displacement (Blunt & Scher 1995; Meleán, Broseta & Blossey 2002). Meleán, Broseta & Blossey (2002) show that at low flow rates, capillary effects broadens the saturation front while at high flow rates these effects are overcome by the pressure induced by the injection pump, which results in a sharper saturation front.

It is possible through the CT scans to estimate the velocity of the saturation front (height of the saturation front divided by the time it took to reach that height from the beginning of the experiment). The height of the saturation front was measured directly in the CT scans and the time when each scan was taken was automatically registered by the CT scanner system. During the first 3 hours of injection, at the HIR, the saturation front advanced at the velocity of 0.7 cm/h. Five hours after decreasing the injection rate to the LIR, the velocity of the saturation front decreased to 0.2 cm/h. At this stage, the geometry of the saturation front was still flat (CT scan not shown). At the moment depicted in Figure 20-B, 20 hours at the LIR, the velocity of the saturation front at the centre and close to the walls is 0.2 cm/h and 0.1 cm/h, respectively. This “slowing down” close to the walls can be interpreted as a consequence of air-trapping. In an epoxy-sealed sample, the

mobility of the fluid near the walls is limited. There are fewer channels (directions) for the air to move ("pushed" by the advancing water) as opposed to the centre of the sample where it has more "freedom" (space) to displace air. This increases hydraulic resistivity near the walls and slows down the advancing water close to the boundary.

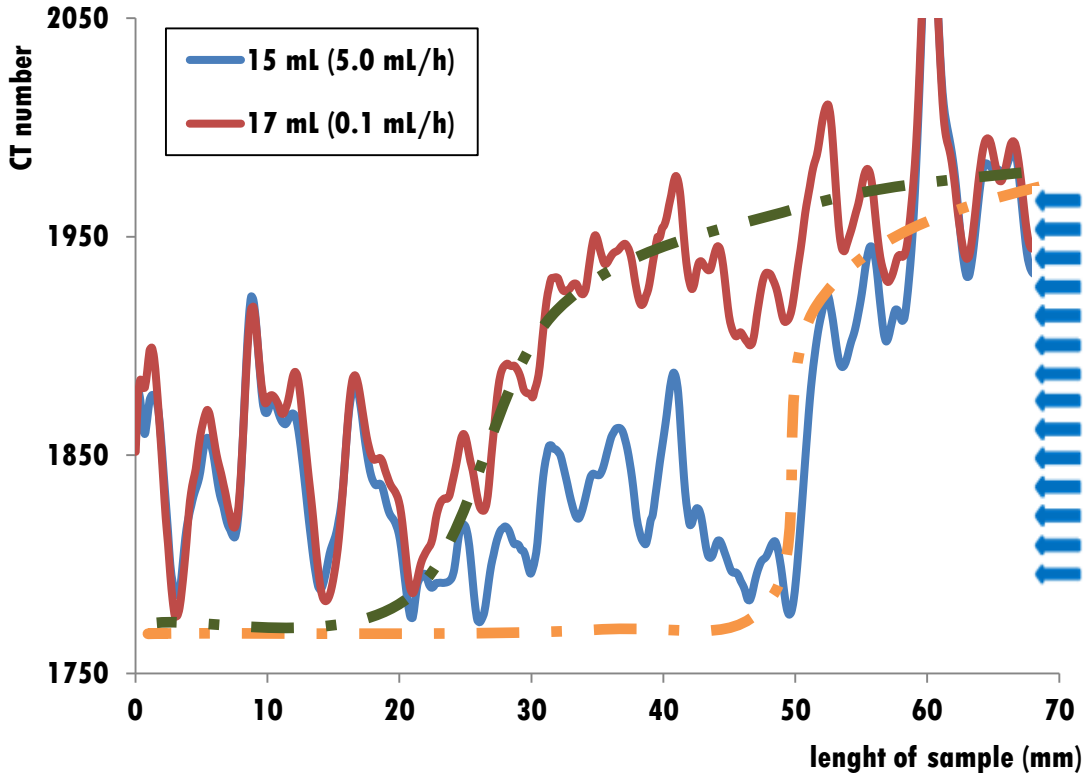

Figure 19 CT number profiles for 15 mL of water injected at the high injection rate (HIR) of 5 mL/h and for 17 mL of water injected at the low injection rate (LIR) of 0.1 mL/h. At the HIR, there is a sharp profile at ~50 mm while at the LIR, there is a dispersive profile. High peaks between 0 and 20 are related to the presence of minerals that are characterized by high CT numbers. Blue arrows represent direction of injection.

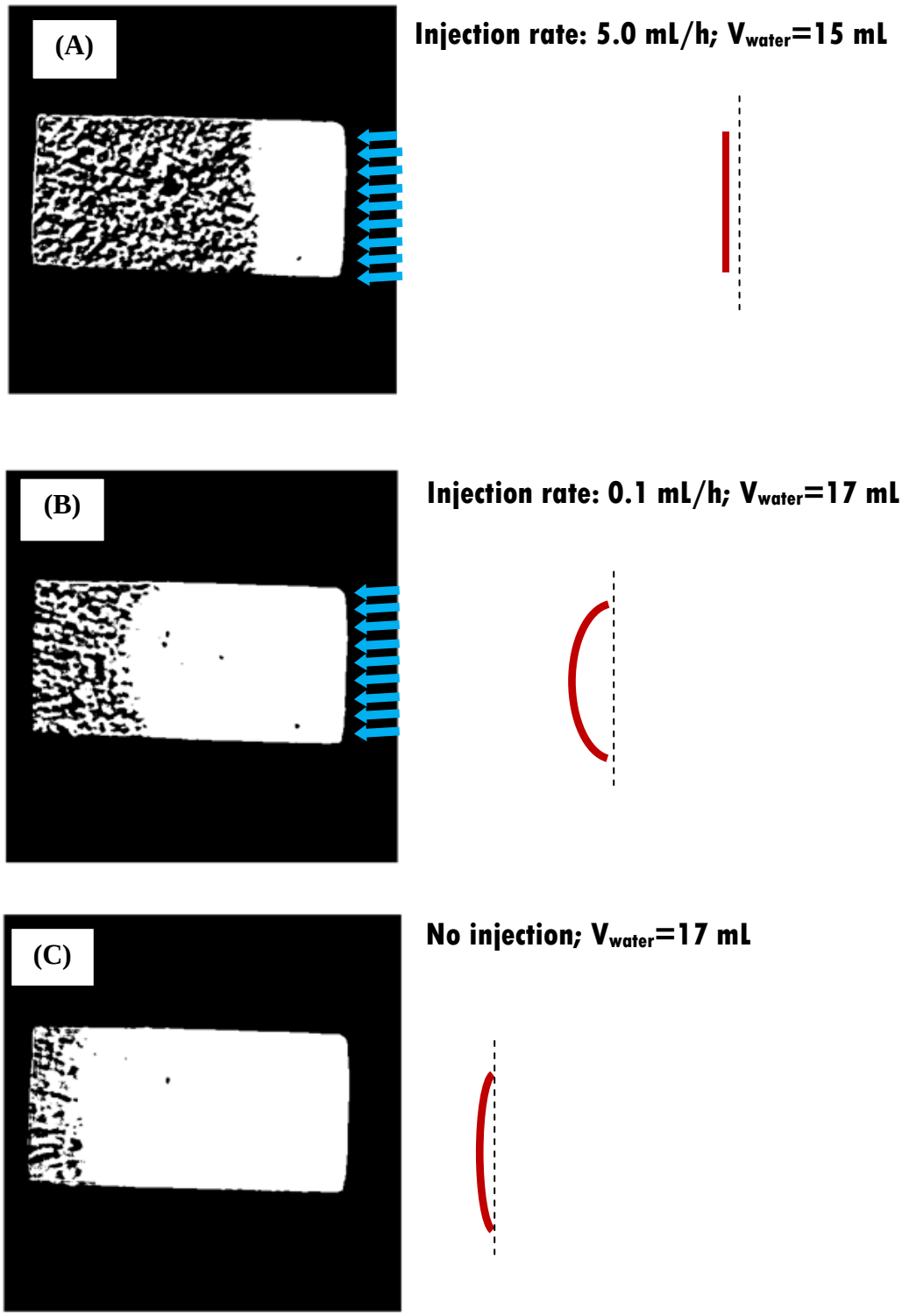

Figure 20 Binarized CT scans: **(A)** after 3 hours at the high injection rate of 5 mL/h, **(B)** 20 hours after decreasing the injection rate to 0.1 mL/h and **(C)** first scan before restarting the injection at the rate of 5 mL/h. Also shown: injection rate, volume of water injected and shape of the saturation front (red lines). Blue arrows indicate direction of injection. Note that the white areas ahead the water front are noise resulting from the image processing.

2.1.2 EVOLUTION OF THE WATER SATURATION

Figure 21 shows the evolution of the water saturation, S_W, with volume of water injected. S_W increased continuously up to 66% in the first 3 hours at the HIR. After decreasing the injection rate to the LIR of 0.1 mL/h, S_W decreased from 65% to 53%, reflecting a considerable redistribution of fluid prompted by the decrease of the injection rate. At the end of the 26 hours at the LIR, S_W increased by 10% because water kept entering and filling the pores that were previously empty. During the LIR, capillary forces are the driving force behind water movement and since small pores have higher capillary forces, they will be preferentially filled (Katz et al. 1966). The decrease of S_W to 55% t the end of the 16 hours of non-injection is related to spreading (diffusion) of the existing fluid in the pore network. The fluid has moved considerably further to the left as it can be seen in Figure 20-C though no "new" water had been introduced. Note that the sample was horizontal, with the direction of injection perpendicular to gravity. When the injection was restarted at the HIR, S_W increased continuously for the next 2h30 reaching the final value of 67%.

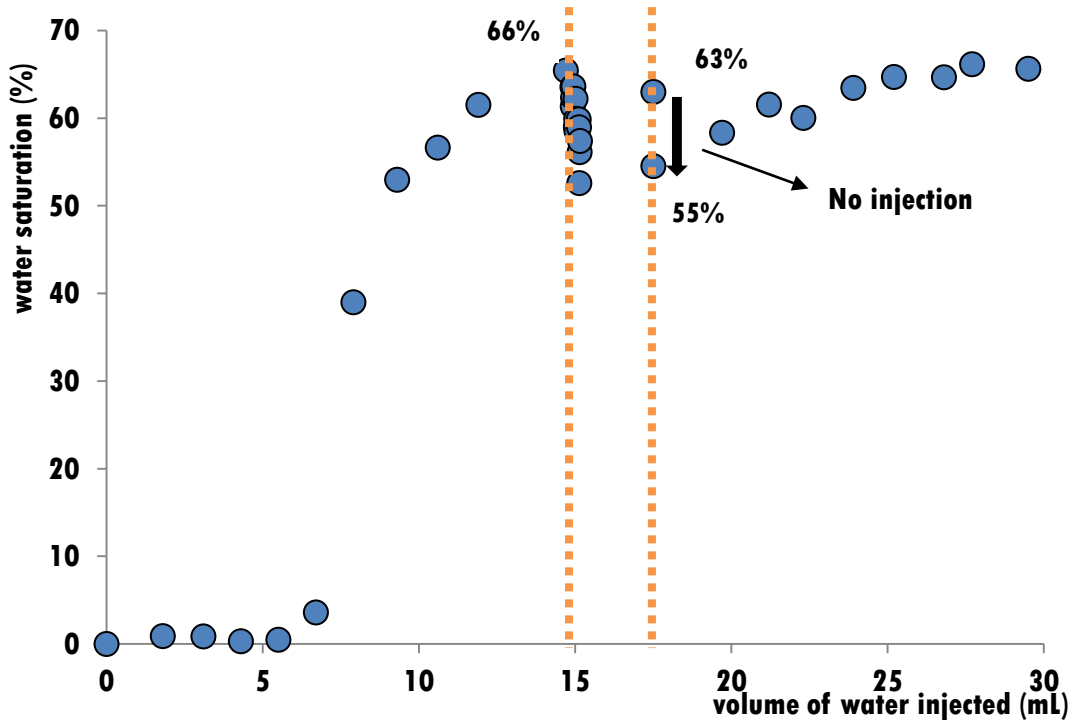

Figure 21 Water saturation (S_W) with volume of water injected. During the 16 hours of non-injection S_W decreased by 8%. Dashed lines represent the moments when (first) the injection rate was decreased from 5 mL/h to 0.1 mL/h and (second) when it was stopped and restarted at 5 mL/h.

2.1.3 ACOUSTIC RESPONSE

The evolution of V_P with total volume of water injected is shown in Figure 22 and in detail for the first 6 hours of injection in Figure 23.

The first drop in the evolution of V_P at the initial HIR was also observed in Chapter 1 and, as discussed before, it is due to the presence of moisture ahead of the saturation front that weakens the grains' cement and as a consequence the bulk density decreases, decreasing V_P (GW theory) (Figure 23, stage A). When the saturation front reached the monitored position, a decay in V_P of 50 m/s is observed (Figure 23, stage B). When the injection rate was decreased, V_P decreased immediately 95 m/s (in 30 minutes) to the minimum value of 2005 m/s (Figure 23, stage C). This decrease was followed by a sudden increase that continued for the next 25 hours of injection, reaching the maximum V_P of 2354 m/s (Figure 23, stage D). At the end of the 16 hours of non-injection V_P had decreased to 2291 m/s. When the injection restarted at the HIR, V_P fluctuated considerably (average: 2250 m/s) for the final 2h30 of injection.

These stages reveal a strong dependence of V_P with the change of injection rate. Upon decreasing the injection rate from the HIR to the LIR, V_P decreased immediately and sharply. This behaviour seems to be connected to the partially saturated conditions of the sample ($S_W = 66\%$, Figure 21) before decreasing the injection rate. This means that locally there are still 24% of pores filled with air. When the injection rate is decreased, the pore pressure decreases too and the air is "free" to expand and move. After 1 hour, more empty smaller spaces are filled with the water that keeps entering the sample and V_P responds by increasing continuously. The oscillation effect that follows when the injection is restarted at the HIR reflects the chaotic redistribution of 55% of local water (a combination of water and air filling 45% of empty spaces) followed by stabilization.

An interesting result, already observed in Chapter 1, is that the same S_W can register different V_P. For this experiment, for example, S_W =76% relates to V_P = 2087 m/s for 14 mL and 2384 m/s for 17 mL of water injected. A significant difference that emphasizes how fluid distribution is a key factor in influencing the resulting V_P.

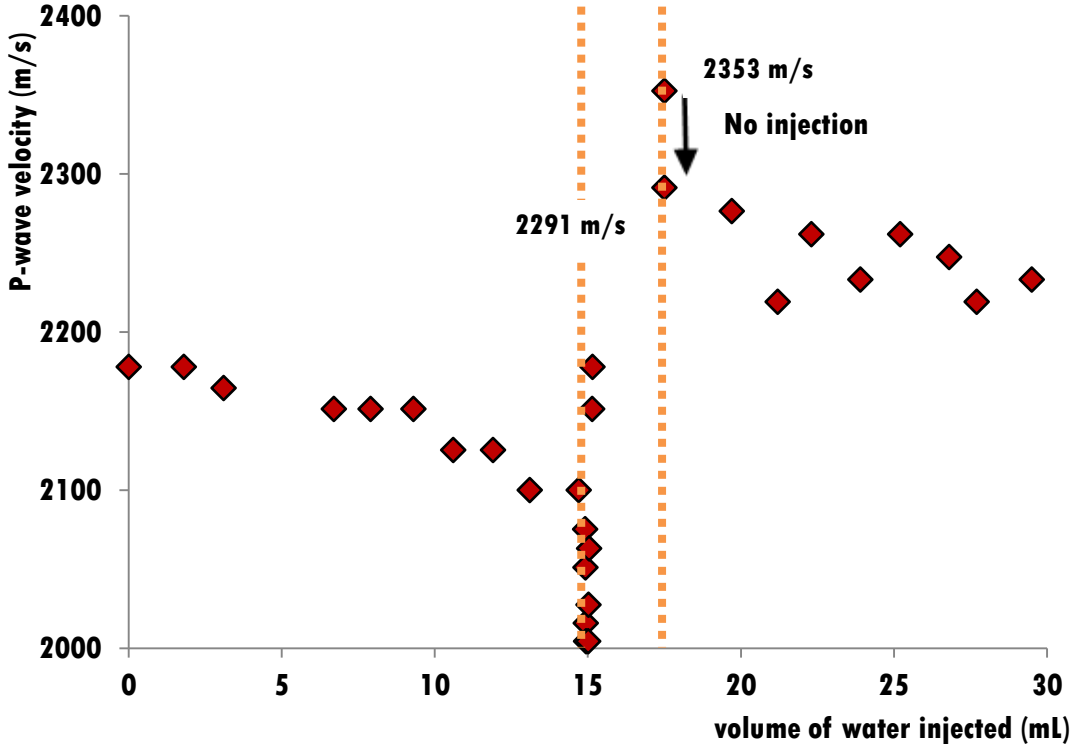

Figure 22 P-wave velocity (V_P) with volume of water injected. Note the decrease of V_P by 62 m/s when the injection was stopped for 16 hours. Dashed lines represent the moments when (first) the injection rate was decreased from 5 to 0.1 mL/h and (second) the injection was stopped and restarted at the rate of 5 mL/h.

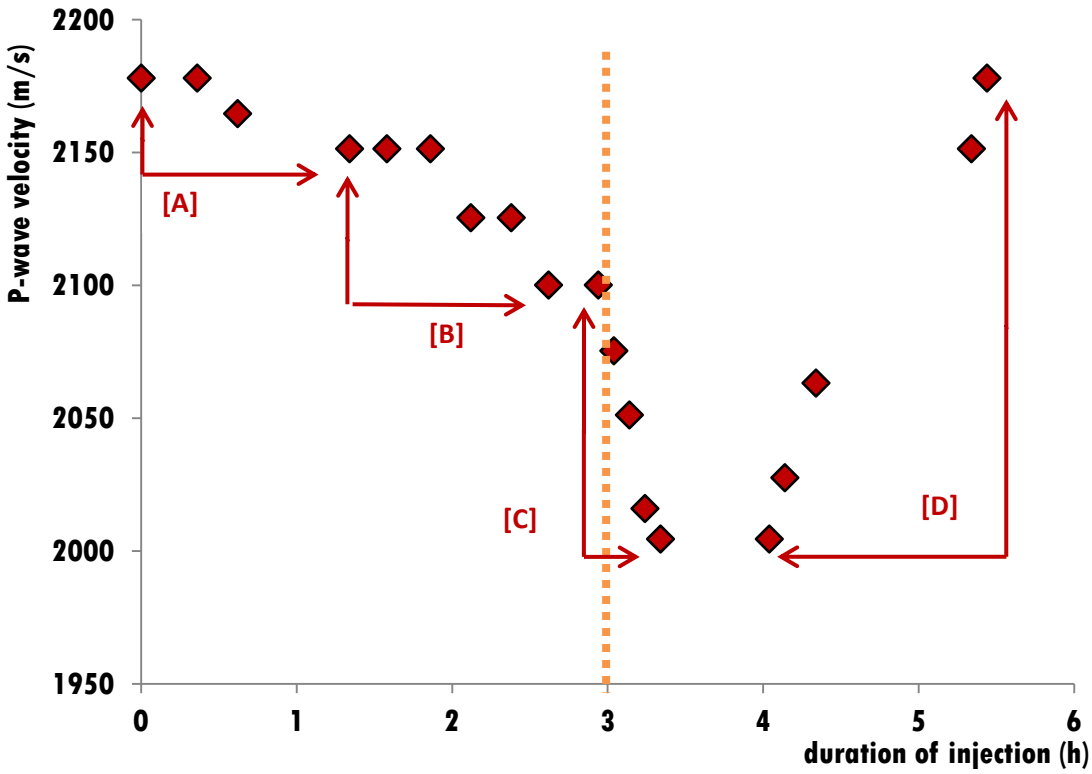

STAGE	DESCRIPTION	ΔV_P per time (m/s/min)
A	Initial decrease "moisture front"	0.23
B	Saturation front reached the monitored position	0.86
C	Decrease of the injection rate	3.96
D	2h30 after the decrease of the injection rate: sudden increase of V_P	2.06

Figure 23 Detail of the variation of the P-wave velocity (V_P) with duration of injection in the first 6 hours of injection. [A] to [D] represent the stages when the evolution of V_P changed significantly. Dashed line represent the moment when the injection rate was decreased from 5 to 0.1 mL/h.

2.2 CONCLUSIONS OF CHAPTER 2

The most important results are:

1. Changing the injection rate has a significant impact in the acoustic response. Particularly:
   a. A fast decrease of the P-wave velocity after decreasing injection rate;
   b. A decrease of the P-wave velocity after stopping the injection rate for a significant period of time;
   c. An oscillation followed by stabilization when the injection was restarted at the higher rate.

Overall, the change on injection rates implies a reorganization of fluids that may not be reflected in the final value of the saturation but it is reflected in the acoustic response.

2. It was established experimentally that decreasing the injection rate promotes the creation of a curved front;
3. Though the resolution of the CT scans does not allow a microscopic analysis of the fluid distribution, the fact that at the same level of water saturation rlates to diffferent P-wave velocities reinforces the idea that acoustic waves are extremely sensitive to fluid distribution.

The influence of fluid distribution in acoustic velocities has been observed experimentally (Knight & Noelen-Hoeksema 1990; Cadoret, Marion & Zinszner 1995). But this is the first time it is experimentally related to changing injection rates.

4. The presence of the saturation front in the acoustically monitored position was detected through a change in the evolution of the P-wave velocity and the water saturation.

CHAPTER 3
VARIABLE INJECTION RATE: LIMESTONE[3]

To better understand the pore-scale phenomena that undergo with changing injection rates, the methodology of Chapter 3 was applied to a different type of rock, namely a limestone. The intention was to confirm if the acoustic response and evolution of water saturation with the change of injection rates observed in Chapter 2 was exclusive of sandstones. The simultaneous acquisition of acoustic waves and 2D CT scans was performed in a Savonnières **limestone** (a weakly layered oolitic limestone from France). The experiment also included:

1. The study of the influence of gravity in the acoustic response and fluid distribution by positioning the sample vertical and horizontal, i.e. with the direction of injection parallel and perpendicular to gravity, respectively;
2. Inferring about physical properties (porosity and interconnectivity of the sample) through the CT scans and their influence in fluid distribution.

Though an important hydrocarbon reservoir rock, limestones have sporadically been studied with emphasis on their physical and elastic properties when dealing with fluid flow experiments. Cadoret, Mavko & Zinszner (1998) studied wave-attenuation in partially saturated limestones under different saturation methods and different fluids. Berryman, Berge & Bonner (2002) used the monitoring of P- and S-waves to infer about porosity and fluid saturation in several types of limestones. Assefa, McCann & Sothcott (2003) measured the P- and S-wave velocity in dry and water saturated limestones with the intention of relating reservoir characteristics, like porosity and permeability, to seismic properties. Zhang et al. (2004) performed water-flooding in two samples of limestones with different vuggy porosity sizes. Interconnectivity and permeability were inferred through the CT scans.

All the mentioned work aided to the understanding of the evolution of acoustic velocities in the presence of water but none of them performed simultaneous

[3] The main results of this Chapter were gathered in a manuscript accepted for publication in Geophysical Prospecting, January 2013.

acquisition of acoustic waves and X-ray CT scans. This is due to several technical difficulties:

1. The low contrast in acoustic velocities between dry and water- or partially-saturated limestones. Since limestones are characterized by a stiff, low compressibility matrix they generate less contrast in acoustic impedance. To solve this issue, the record of P-waves required sensitive acoustic transducers and an acquisition system of good resolution.
2. The relative small change between the CT numbers when the sample is saturated and dry ($\frac{CT_{sat}-CT_{dry}}{CT_{dry}}$) makes difficult to assess which areas are saturated by direct visualization of the CT scans This issue was overcome by applying a threshold algorithm to the raw CT scans to enhance the contrast between dry and wet zones. This algorithm was a clickable option at the image software *ImageJ*.

The P-wave arrival times between dry and water-filled areas are more distinguishable than the ones between water- and oil-saturated areas (in this last case, the change in P-wave arrival time may not even be measurable) (Lumley 2001). In addition, the contrast in the CT scans is low if we inject water in oil or water saturated samples. Therefore, we chose to inject solely distilled water into a dry sample. This also allowed using the same sample in several experiments without significant structural damage between imbibitions.

This chapter is organized as follows. First, the experimental procedure is described (Section 3.1). Next, a structural analysis of the sample based on the CT scans is presented (Section 3.2). In Section 3.3, results are presented regarding (1) the advancement of the saturation front and its dependence on the structure of the sample; (2) the evolution of the P-wave velocity and water saturation with the presence of water and with the change of injection rates. It is followed by the study of the influence of gravity in the evolution of those two parameters. In Section 3.4, the connection of the evolution of the P-wave velocity, water saturation and fluid distribution to physical-driven processes is discussed. Section 3.5 concludes the chapter by pinpointing the most important results and how they relate to results found in the previous chapters (1 and 2).

3.1 METHODOLOGY

The main petrophysical properties of the limestone are shown in Table 3. Figure 24 shows a high resolution reflected light photograph of the polished rock surface showing oolitic and coated grains and the vuggy porosity that characterizes the sample. It is a 98% calcite limestone, of fine, round, closely woven grains with many vesicles[4].

The sample was set for two positions:

1. First, in a horizontal position so that the direction of the injection was perpendicular to gravity. In the following, it will be denoted as the horizontal injection experiment, or in short **HIE**.
2. Second in a vertical position with the injection parallel to gravity. It will be referred as the vertical injection experiment, or in short **VIE**.

HIE and VIE are needed in order to understand the role of gravity forces in the evolution of the P-wave velocity and water saturation. Both HIE and VIE started at the high injection rate (HIR) of 2 mL/h. This rate was then decreased to the low injection rate (LIR) of 0.2 mL/h after approximately 3 hours for the HIE and 4 hours for the VIE. This rate was kept constant for approximately 19 hours (HIE) and 14 hours (VIE). Then, the injection rate was increased back to the HIR of 2 mL/h until the end of the injection. P-waves were monitored at two positions: one close to the point of injection, position C, and the other in the middle of the sample, position M. Figure 25 shows the limestone set for the VIE and a CT scan of the dry sample with the circles marking the position of the transducers on the YZ scanning plane.

All experiments were performed on the same sample. By only injecting distilled water (at room temperature), with no added chemicals (no salt or X-ray contrast agent), possible complications from chemical reactions are avoided. The experiments were performed at room temperature and atmospheric pressure (no axial or confining pressure is applied to the sample).

[4] www.haussmannstone.com/catalog/project-materials/Savonnieres

SAVONNIÈRES LIMESTONE	
Length (cm)	**7.81**
Diameter (cm)	**3.84**
Porosity (%)	**26.5**
Pore Volume (mL)	**23.9**
Permeability (mD)	**91.5**

Table 3 Main petrophysical characteristics of the Savonnières Limestone.

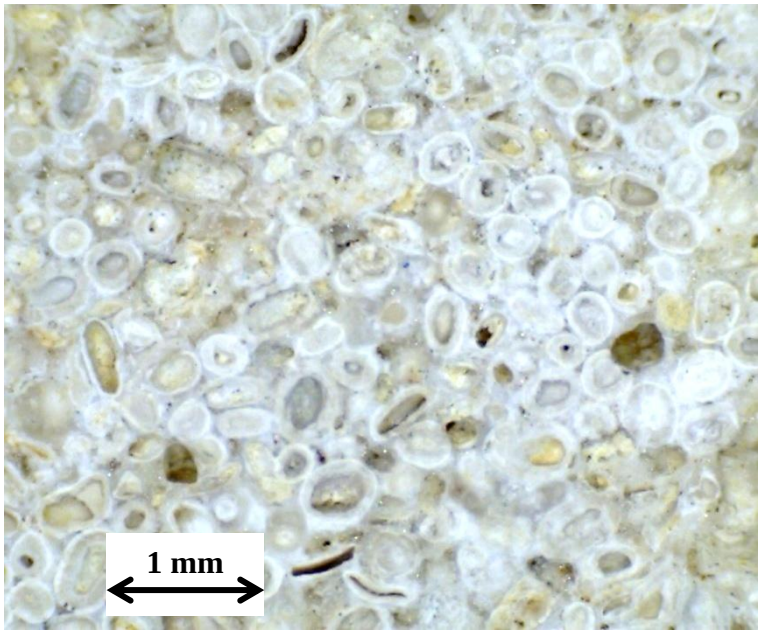

Figure 24 Microscopic view of the vuggy porosity of the Savonnières Limestone.

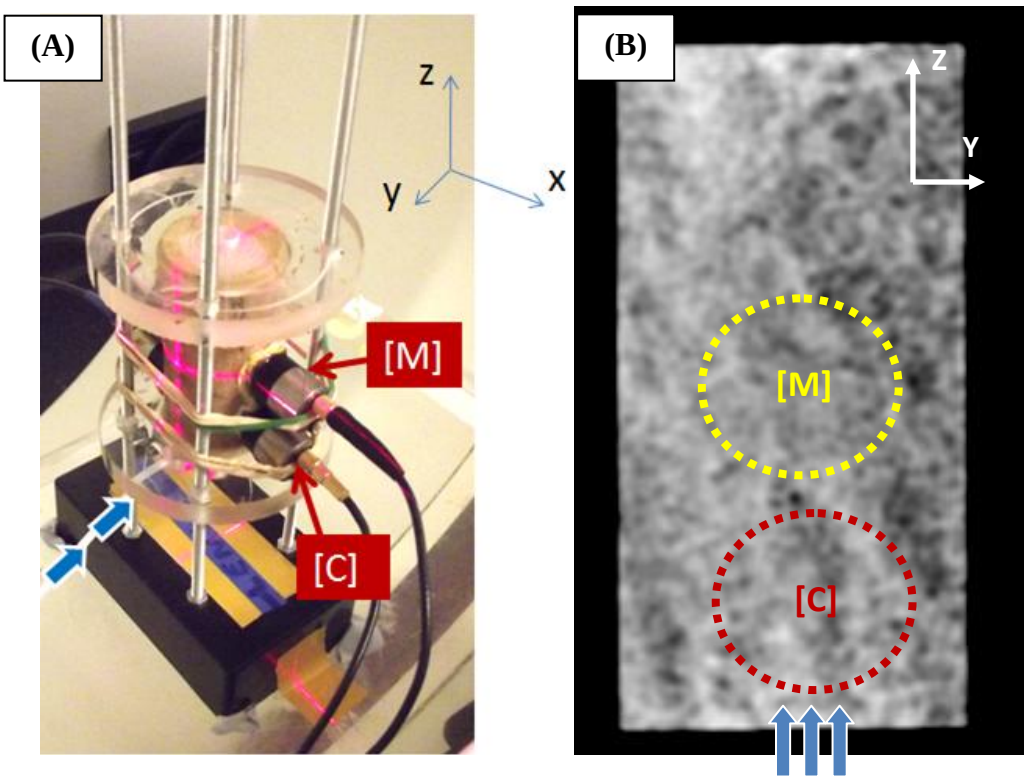

Figure 25 (A) Limestone connected to two pairs of transducers: position C, close to the point of injection, and position M, in the middle of the sample. **(B)** CT scan of the dry sample set for the vertical injection experiment. Red and yellow circles mark the position of the transducers on the YZ scanning plane. Blue arrows indicate direction of injection.

3.2 STRUCTURAL ANALYSIS FROM X-RAY CT

Limestones are sedimentary rocks that can be formed directly by precipitation of calcite or by accumulation of organic sediments creating very heterogeneous rocks. The structural heterogeneity of the limestone was observed through direct inspection of the CT scans: the right side of the CT scan was darker than the left side (a contrast in the grey-scale gradient that remained with the injection) (Figure 25-B). This indicates that the right side of the sample was more porous than the left side. To quantify this heterogeneity, the sample was divided in 3x4 sections of the same size (Figure 26-A). The average porosities of each section were estimated by comparing the CT scan of the sample when it was fully water-saturated and when it was dry. The fully water saturation was achieved with the help of a drying-oven. The sample was totally immersed in a tray full of water and through vacuum the air inside the sample was extracted and replaced by water. This was done continuously over two days.

To estimate the porosity ϕ of each section, $CT_w = CT_{\text{full saturated}}$, and $S_W = 1$ are replaced in Equation 15:

$$S_w = \frac{CT_{fullsat} - CT_{dry}}{\phi \times 1000} = 1. \quad (23)$$

Therefore, the porosity ϕ of each section is given by:

$$\phi = \frac{CT_{fullsat} - CT_{dry}}{1000}. \quad (24)$$

The error in estimating the porosity is 2% (following Equation 17-19).

A porosity map is shown in Figure 26-B. The lowest porosities are in average at the left side of Figure 25-B, as it was inferred initially by direct observation of the CT scans.

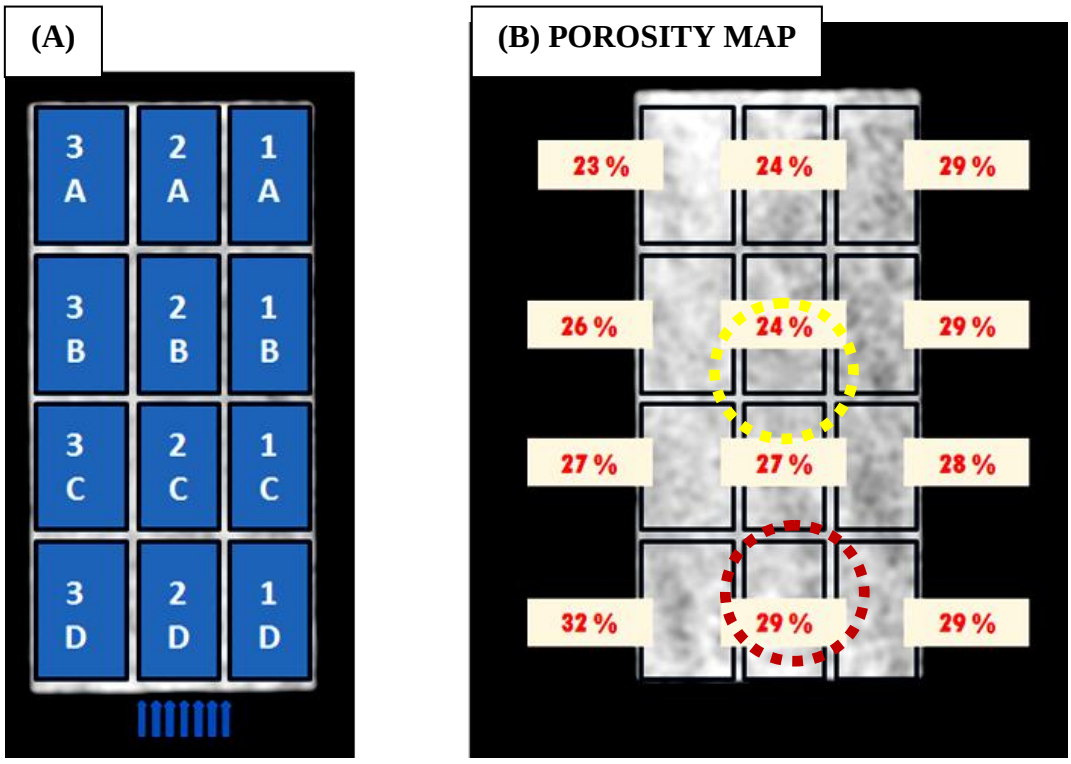

Figure 26 (A) Sample divided in 4 rows (A to D) x 3 columns (1 to 3). **(B)** Porosity map. Note the darker right side of the CT scan associated to sections of higher porosity. Red and yellow circles mark the position of the transducers in position C and M, respectively.

3.3 RESULTS

3.3.1 ADVANCEMENT OF THE SATURATION FRONT

Figure 27 presents a sequence of binarized CT scans for the first 4 hours of the initial injection at the HIR for the VIE. The difference between the dry CT scan and the water-saturated CT scan is small so the background image was subtracted to better enhance the areas filled with water. The image processing is explained in Section 2, Figure 5. The red and yellow circles represent the area covered by the transducers in position C and M, respectively. The following stages are highlighted:

[A] Before the injection (dry sample);

[B] After injecting 2.1 mL of water: the saturation front reached the ultrasonically monitored position C;

[C] After injecting 3.3 mL of water: the saturation front passed the position C and was approaching position M;

[D] After 4.3 mL of water injected: the saturation front did not advance much in height when compared to [C]. This is because the water spread laterally, increasing the initial curvature, before advancing in height;

[E] At 6.8 mL of water injected: the saturation front had longed passed the monitored position C and was starting to reach position M.

An initial curvature of the saturation front due to point injection is observed in Figure 27-B and an asymmetry of the saturation front is observed in Figures 27-C and 27-D. Both features disappeared as the injection progressed (Figure 27-E). The initial asymmetry of the saturation front (Figure 27-C) confirms the sample's structural heterogeneity discussed in the Section 3.2. This feature constrained the definition of a flat, piston-like saturation front. The asymmetry of the saturation front was also present in the HIE (data not shown).

The differences in local porosity (Figure 26) and their effect on the advancement of the saturation front were inferred by plotting the evolution of S_W with duration of injection, per column or per row. Figure 28-A shows the evolution of S_W with

duration of injection for column 1, for the first 8 hours of VIE, with the decrease of injection rate at 225 minutes (orange dashed line). This plot gives information about the time it takes for the saturation front to reach each section, i.e. at which moment S_W started increasing. The water detection threshold is defined as the moment in time (and volume of water injected) when S_W started increasing from 2% (Equation 19). More particularly:

1. The presence of an inflexion point due to the change of injection rate (orange line in Figure 28) for rows 'D' and 'C'. This inflexion is not present in row 'B' as there is not enough water (S_W = 20%) to "feel" the effect of the change of injection rate. In row A, water has not yet reached this section.
2. The change in S_W after decreasing the injection rate is more pronounced for row 'D', ΔS_W = 14%, than for row 'C', ΔS_W = 11%. S_W is higher for 'D' and its evolution was moving towards stabilization. Therefore, more water was "disturbed" and displaced by the change of the injection rate.
3. For column 1, as expected, the lower row 'D' "feels" the water first, t = 15 min after the beginning of the injection, followed by row 'C' (t = 50 min), then row 'B' (t = 145 min) and finally row 'A' (t = 330 min). The increase of time between rows 'C' and 'B' when compared to rows 'B' and 'A' reflects the influence of gravity that pulls the water downwards, slowing down the advancement of the saturation front.

Figure 28-B shows the evolution of S_W with the duration of the injection for row B. There is a significant time delay between sections: the saturation front reached section '3B' 35 minutes after reaching sections '1B' and '2B'. This difference enhances the structural heterogeneity of the sample that impedes the saturation front from advancing straight and parallel to the base of the sample. There is also time delays for the HIE (data not shown). They are, in general, influenced by gravity effects where the injected water, for each column, fills the lower rows first and then the upper rows.

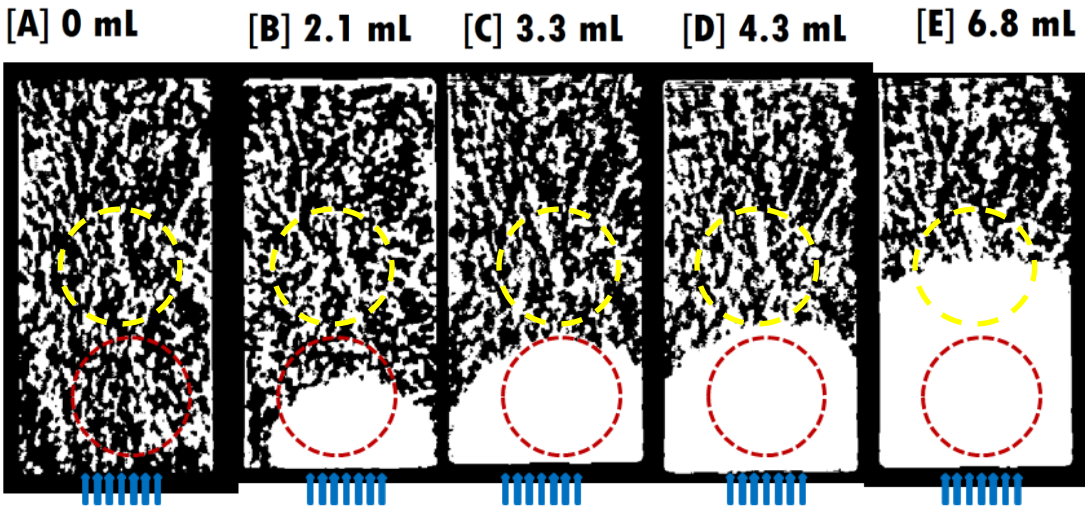

Figure 27 Binarized CT scans of the first 4 hours of injection at the rate of 2 mL/h. Red and yellow circles represent the area covered by the transducers in position C and M, respectively. Blue arrows indicate the direction of injection. Note that the white areas ahead the saturation front are noise resulting from the digital image processing.

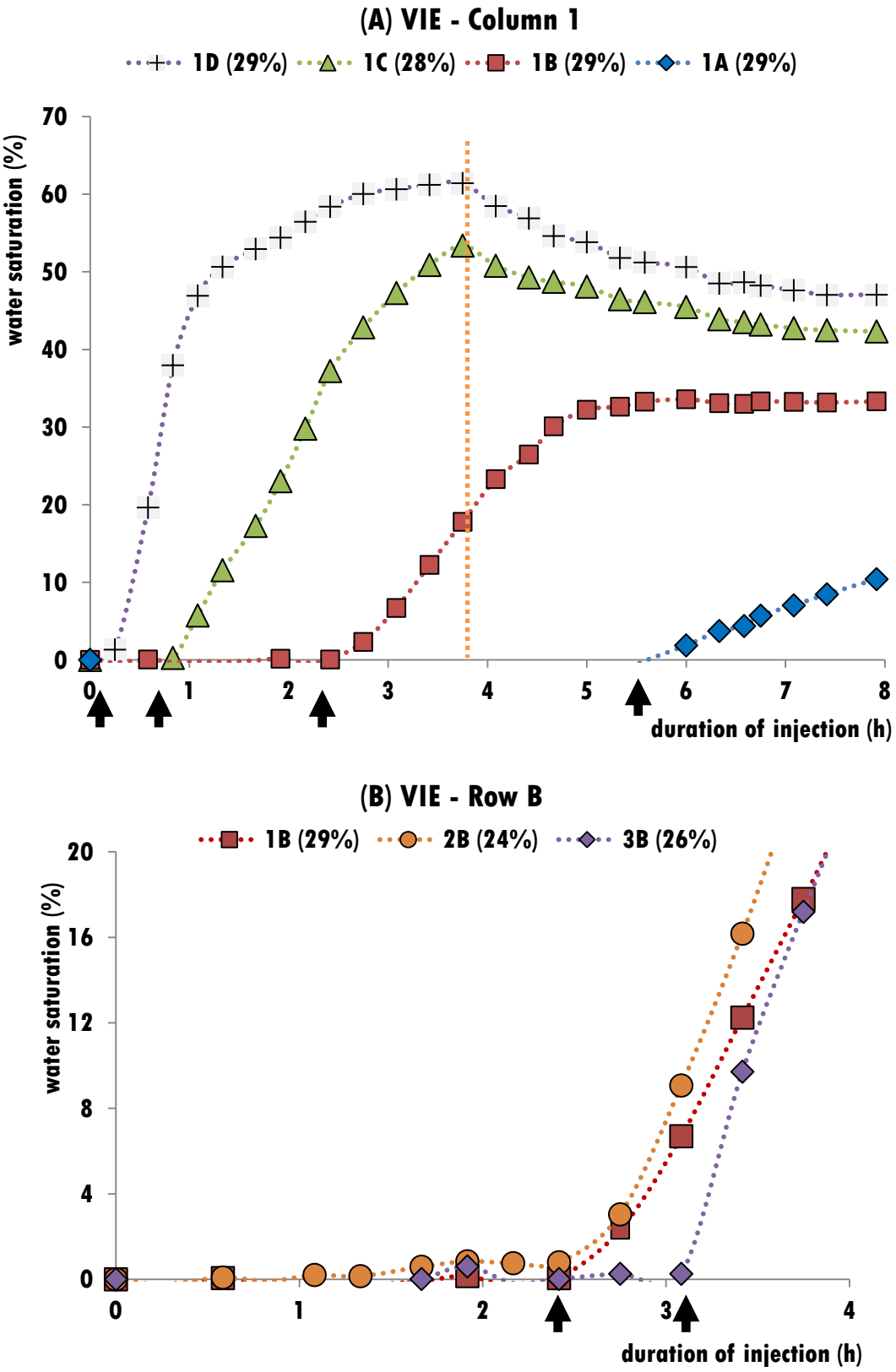

Figure 28 Water saturation with duration of injection for **(A)** column 1 and **(B)** row B for the first 8 and 4 hours, respectively, of the vertical injection experiment (VIE). Orange line in (A) represents the moment when the injection rate was decreased. Black arrows indicate the moment when the water saturation started increasing for each section. Porosities of each section are also shown. Note the time delay between sections 1B-2B and 3B of 35 minutes.

3.3.2 EVOLUTION OF THE WATER SATURATION

The evolution of S_W for VIE is shown in Figure 29 for the ultrasonically monitored positions C and M. S_W increases continuously after the saturation front reached the ultrasonically monitored positions. When the injection rate was decreased from the HIR of 2 mL/h to the LIR of 0.2 mL/h: (1) S_W decreased immediately from 60% to 45%, at position C. It remained close to this value until the end of the injection period at the LIR; (2) at position M, S_W stopped increasing immediately and remained constant at 37%.

The different behaviour in the evolution of S_W after decreasing the injection rate between the monitored positions C and M is influenced by the position of the saturation front. At position C, a high value of S_W (60%) was reached before the injection rate was decreased while at position M, S_W was much lower, 37%. As soon as the injection rate was increased back to the HIR S_W increased about 11% for both positions. This initial sudden increase is followed by a steady increase, more pronounced for position M. These rate-dependent changes in saturation occur despite the fact that the total amount of water in the sample is always increasing, and therefore they must reflect the way the water redistributes in the heterogeneous pore space of the limestone: the system will be closer to capillary and gravity equilibrium at slow rates than it is at fast rates (as observed in Chapter 1).

When the evolution of S_W is plotted for all the columns and rows of Figure 25, a list of the S_W reached at the end of the experiment for each section can be tabled. This analysis shows if the water was evenly distributed in the sample. The results for VIE are presented in Table 4. Overall, the highest final S_W was reached in the sections of lowest porosity (sections ‘3A’, ‘3B’ and ‘2B’) and the lowest final S_W were reached at the sections of higher local porosity (sections ‘1A’ and ‘3D’) (see Figure 26). Microstructural observation of the oolitic Savonnières limestone suggests an explanation for the higher saturation in less porous parts of the rock. Regions with lower porosity have pores that are more uniform, on average smaller and preferentially are invaded by spontaneous imbibition of water whereas the more porous parts have large and poorly connected mouldic pores that trap air and remain incompletely filled as water invades upwards.

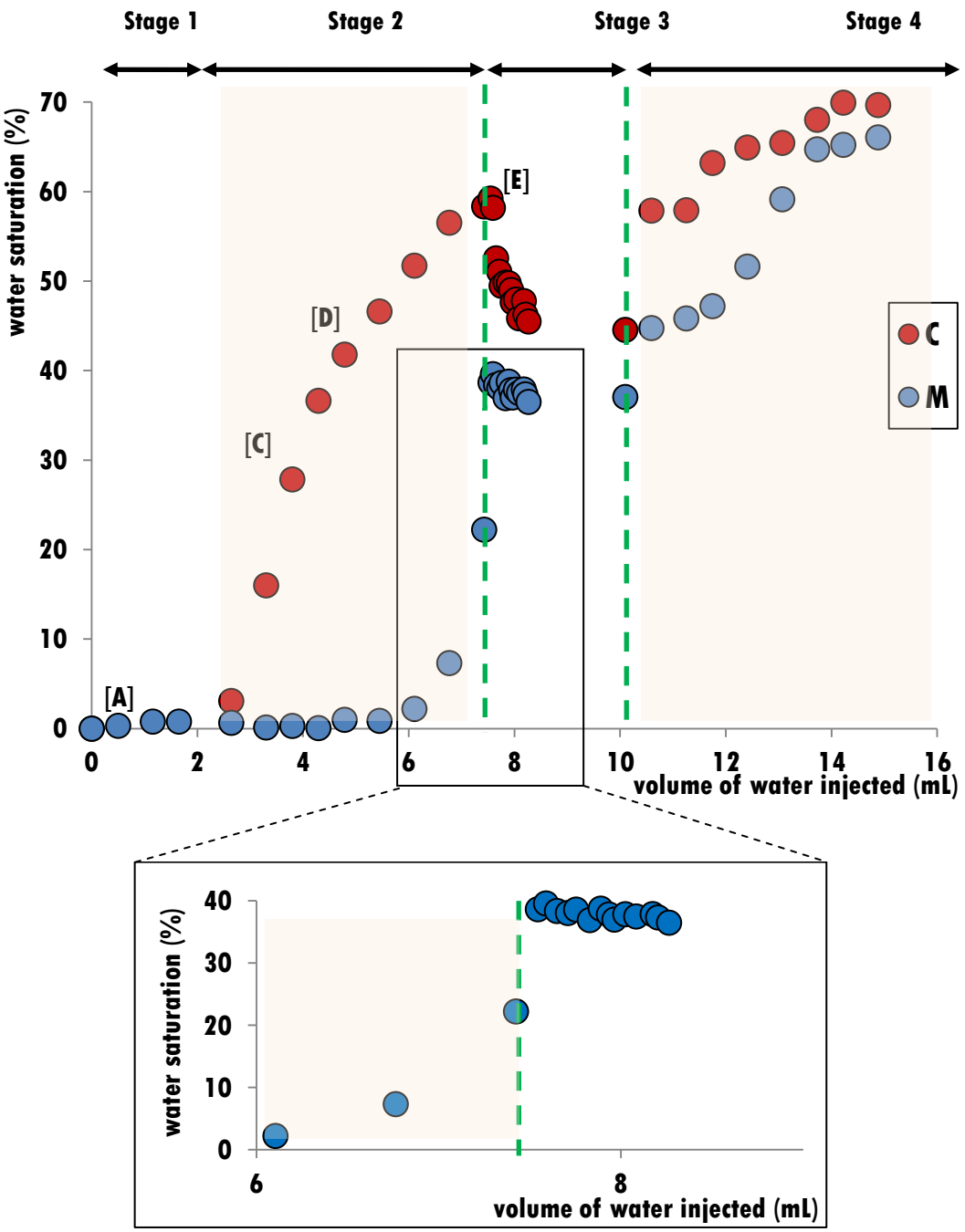

Figure 29 Water saturation with volume of water injected for the vertical injection experiment (VIE), positions C and M. [A] to [E] represent the moments depicted in Figure 27. **In the detail box:** there is no change in water saturation for position M after decreasing the injection rate. Green dashed lines mark the moment when the injection rate was (first) decreased and (second) increased.

VIE FINAL WATER SATURATION (%)		
3A 73	2A 75	1A 59
3B 65	2B 75	1B 62
3C 63	2C 65	1C 63
3D 55	2D 74	1D 63

Table 4 Final water saturation (S_W) reached for each section (rows A to D; columns 1 to 3) in the vertical injection experiment (VIE). Note the lowest S_W at section 3D, the more porous section (see Figure 25-B).

3.3.3 ACOUSTIC RESPONSE

Figure 30 shows the P-waveforms recorded before injection and after injecting 6.8 mL of water at the HIR. There is a significant decrease in the P-wave amplitude: a decrease of 65%, between the wave-amplitude for 0 mL (WA1) and the wave-amplitude for 6.8 mL of water injected (WA2). For the same period, there is an increase in P-wave arrival time resulting in a decrease of 26 m/s in P-wave velocity (V_P). The decrease in P-wave amplitude and change in P-wave arrival time are indicatives of the presence of partial fluid saturation in the pore space.

When applying Equation 20, the average V_P error results in 7 m/s, reflecting the high precision of our experimental measurements.

Figure 31 shows the evolution of V_P with volume of water injected, for positions C and M, for the VIE. When the saturation front reached position C (after injecting 2.1 mL of water, Figure 26-B) V_P quickly decreased from the initial value of 3392 m/s. After 3.3 mL of injected water (Figure 26-C) V_P quickly increased as the saturation front crossed the monitored position. This pattern of decreasing V_P with the approach of the saturation front (the wet-dry interface) and increasing as the saturation front was crossed the monitored position also occurred for position M.

It is also important to note that the difference of 110 m/s in V_P between positions C and M for the dry sample is an expected feature and part of the baseline differences due to the heterogeneous porosity of the limestone sample (confirm Figure 26-B).

The influence of changing injection rates (from the HIR to the LIR and back to the HIR) on the acoustic response can be observed in Figure 31, for positions C and M, for VIE:

1. Decreasing the injection rate decreased V_P for both monitored positions: At position C the decrease was immediate, from 3403 m/s to 3377 m/s. It lasted for 2hr 30min and was followed by a sharp increase. At position M the decrease of V_P only happened 1 hour after the decrease of injection rate. This decrease was sharp, from 3275 m/s to 3221 m/s.

2. V_P increased when the injection rate was increased. At both monitored positions the initial increase was immediate and followed by a constant evolution for position C and a slight decrease for position M.

The evolution of V_P seen in Figure 31 was also present for the HIE (data not shown). The same response to the presence of water and to the change of injection rate was observed (check Figure 33).

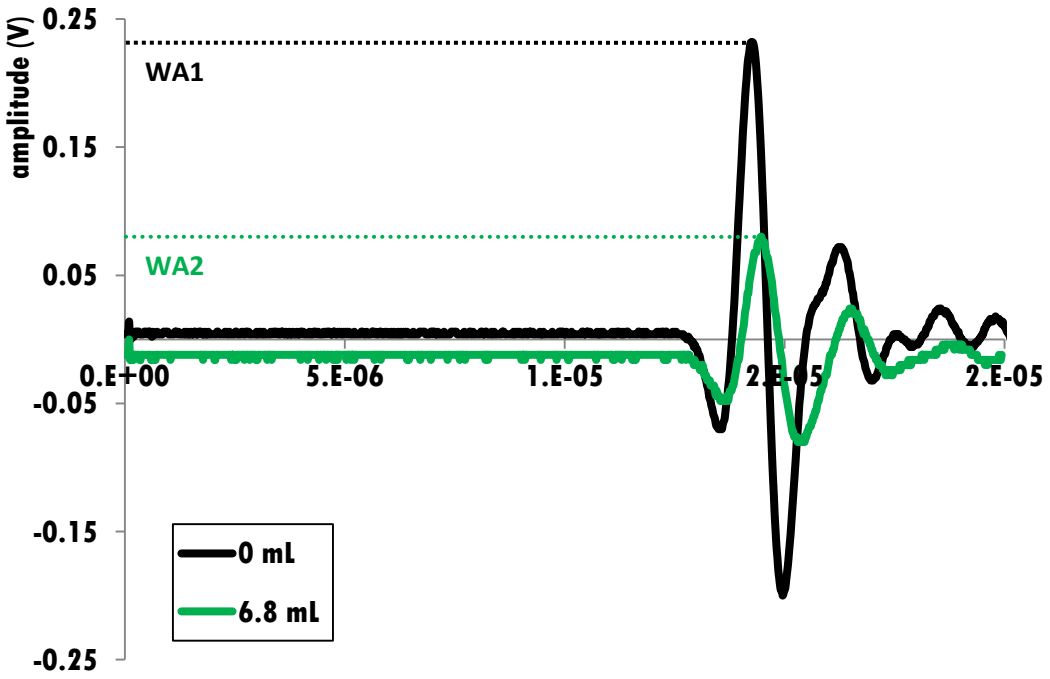

Figure 30 Waveforms for the P-waves recorded before injection (black line) and after injecting 6.8 mL of water (green line). The decrease of wave-amplitude (from WA1 to WA2) reflects the presence of water.

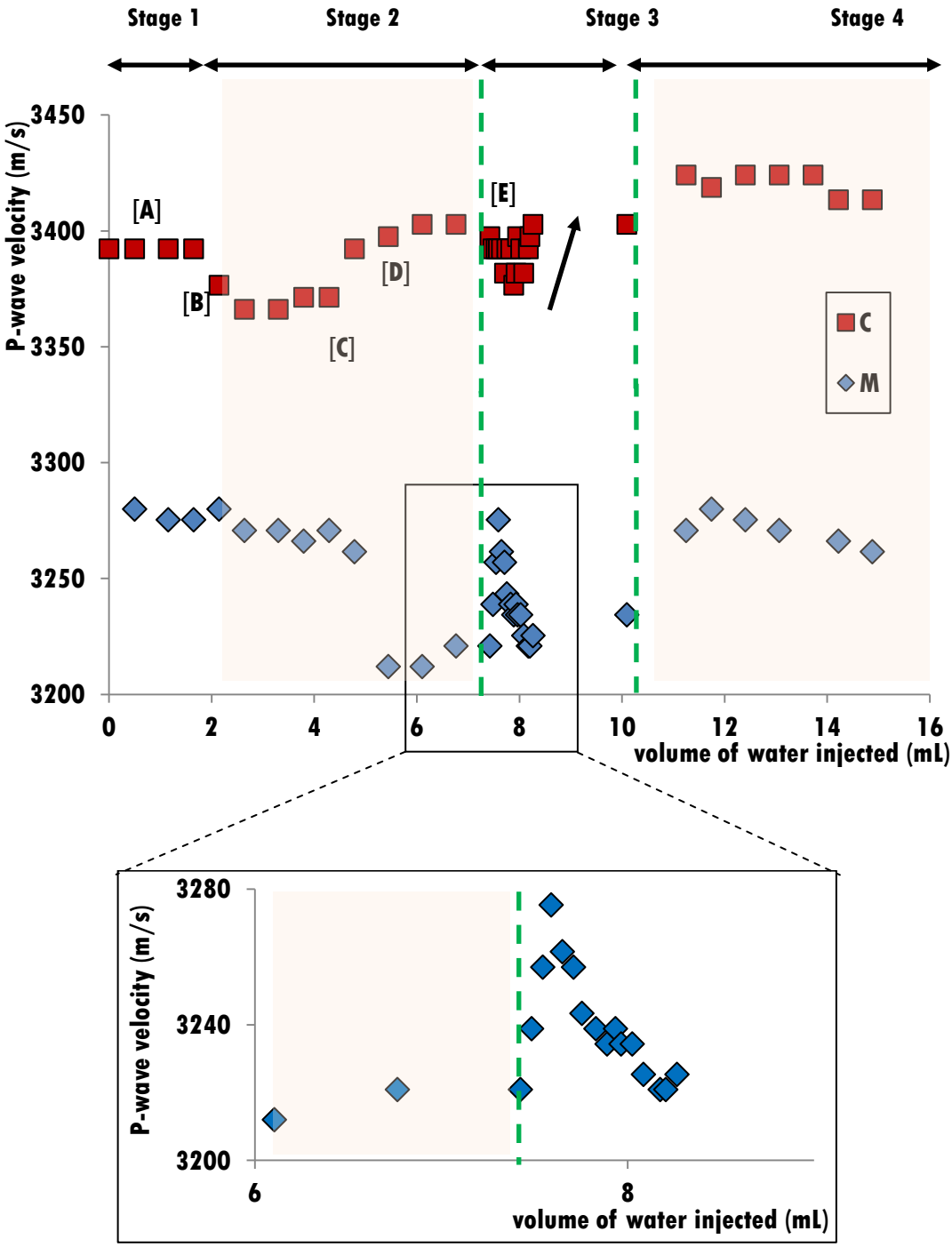

Figure 31 P-wave velocity (V_P) with volume of water injected for the vertical injection experiment, positions C and M. [A] to [E] represent the moments depicted in Figure 27. **In the detail box:** there is a "delayed response" in position M to the change of injection rate: only 1 hour after decreasing the injection rate, V_P started decreasing. Green lines mark the moment when the injection rate was decreased and increased.

3.3.4 INFLUENCE OF GRAVITY IN THE EVOLUTION OF THE WATER SATURATION & THE P-WAVE VELOCITY

Figure 32 shows the evolution of S_W with volume of water for VIE and HIE, for monitored positions C and M. The following observations can be made:

1. For both positions, the presence of water is detected 30 minutes sooner for the HIE;
2. At position C, S_W started increasing at 1.5 mL and 2.6 mL of injected water for HIE and VIE, respectively.
3. At position M, after decreasing the injection rate, S_W stabilized at 37% for the VIE but kept increasing up to 49% for the HIE.
4. When the injection rate was decreased back to the HIR, S_W increased fast in the first 2 hours for the VIE while the increase was slower for the HIE.

Figure 33 shows the evolution of V_P with volume of water injected for HIE and VIE, for positions C and M. A difference in the acoustic response with the direction of injection is also observed. More particularly:

1. In the beginning of the experiment, the decrease in V_P due to the entrance of the saturation front occurred sooner for the HIE. It promoted a stronger increase HIE (V_P increased 72 m/s) than for VIE (it increased 40 m/s);
2. When the injection rate was increased back to the HIR, V_P increased fast for VIE and slower for HIE (also seen for S_W, Figure 32).

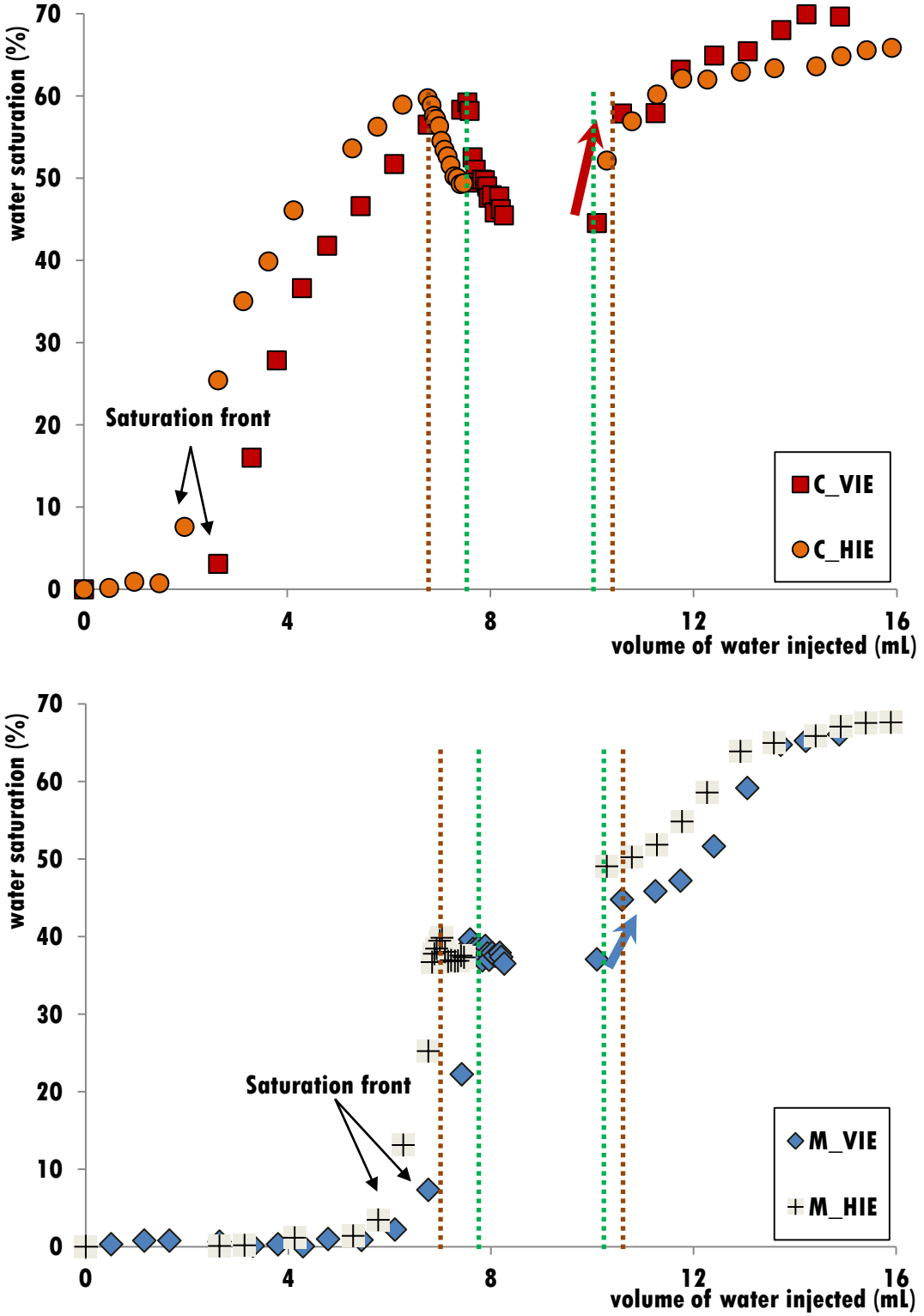

Figure 32 Water saturation (S_W) with volume of water injected for the vertical (VIE) and horizontal injection experiment (HIE), for positions C and M. Note that the presence of water is "felt" sooner for HIE (for both positions) (black arrows). Also note that the increase of S_W with the increase of injection rate is initially sharper for the VIE (red and blue arrows). Brown and green lines mark the moments when the injection rate was (first) decreased and (second) increased HIE and VIE, respectively.

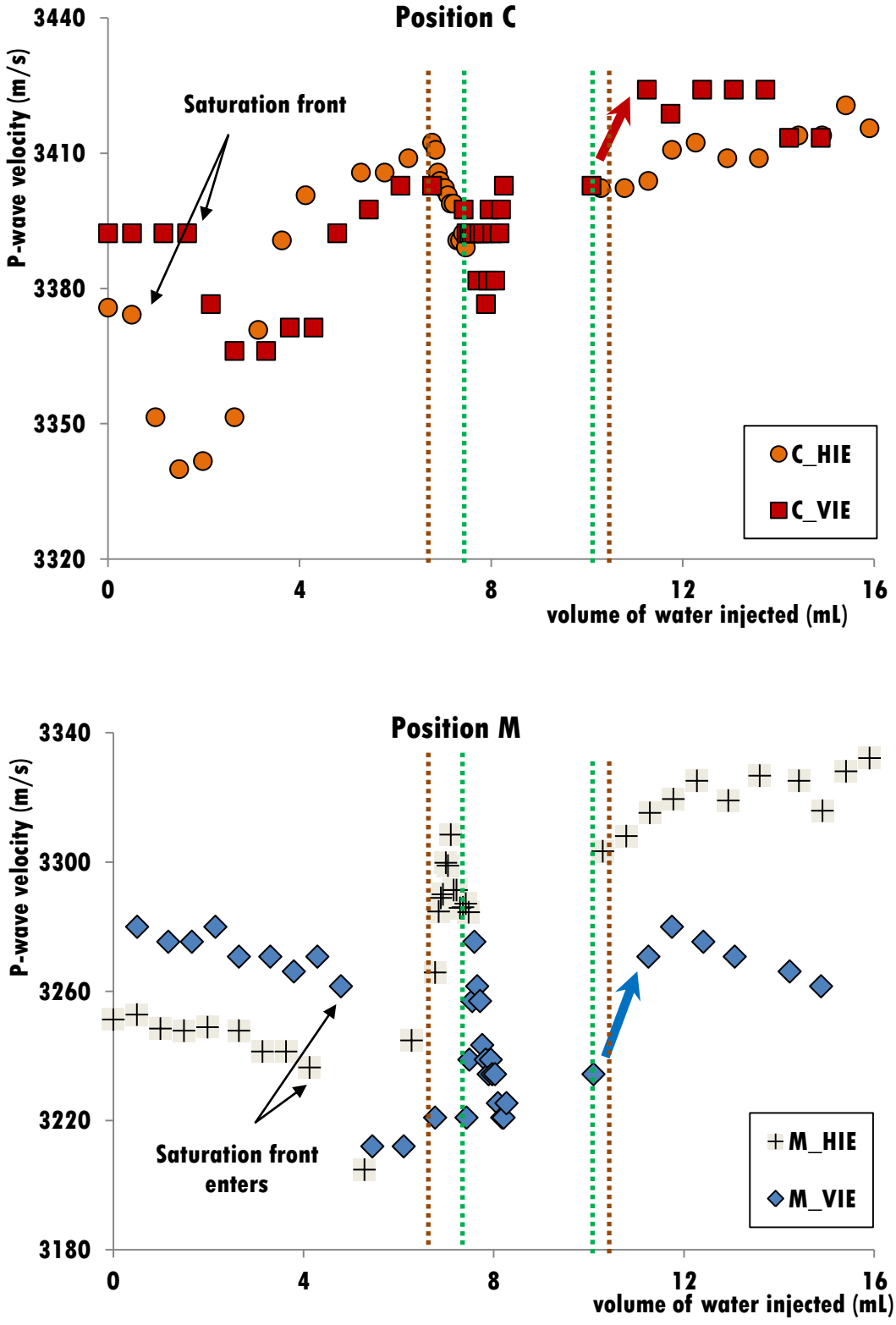

Figure 33 P-wave velocity (V_P) with volume of water injected for positions C and M, for the vertical (VIE) and horizontal injection experiment (HIE). Note that the presence of water is "felt" sooner for the HIE (for both positions) (black arrows). Also the increase of V_P with the increase of injection rate is initially sharper for VIE (blue and red thick arrows). Brown and green lines mark the moments the injection rate was (first) decreased and (second) increased for HIE and VIE, respectively.

3.4 PHENOMENOLOGICAL INTERPRETATION

In order to interpret the observations described in the previous sections regarding the evolution of acoustic wave velocities and water saturation, the following concepts are applied: (1) macroscopic capillary pressure (the difference in pressure across the interface between two immiscible fluids, p_c) and its dependence on saturation; (2) fluid-patch membrane stiffness due the presence of capillary forces (Tserkovnyak & Johnson 2003). The latter can be combined with the Gassmann-Wood (GW) theory (Mavko, Mukerji & Dvorkin 2009; Toms et al. 2006). These concepts allow modelling the observed saturation and ultrasonic velocity dependence on the injected fluid volume in a qualitative yet consistent manner.

3.4.1 FLUID FLOW REGIME

Capillary effects are important if the relative contribution of capillary forces with respect to viscous and gravity forces reach a certain level. At the macroscale, an estimate of the relative importance of these effects is given by the capillary number C_a (e.g., Riaz et al. 2007)

$$C_a = \frac{\mu_w U}{\gamma} \tag{25}$$

with $U = \frac{4Q}{\pi D^2}$. μ_w is the viscosity of the injected fluid (for water, 10^{-3}Pa. s) and U is the injection velocity. The latter depends on the injection rate Q, the diameter of the sample D (3.84 cm) and the interfacial tension between air and water γ ($72 \times 10^{-3} \frac{N}{m}$ at 25°C). $C_a \sim 2 \times 10^{-9}$ is obtained for the high injection rate (Q = 2 mL/h) and $C_a \sim 2 \times 10^{-10}$ for the low injection rate ($Q = 0.2$ mL/h). Both capillary numbers are much less than 10^{-5} and therefore capillary effects should be taken into account (Ding & Kantzas 2004).

Though capillary forces arise at fluid-fluid interfaces on the pore scale, they give rise to a macroscopic expression. In steady-state flow the macroscopic capillary pressure, C_a, is the difference between the macroscopic pressures of the non-wetting phase (air) and wetting phase (water). The macroscopic capillary pressure is inherently related to the saturation (Perkins 1957). A generic capillary pressure-saturation (CPS) relation is depicted in Figure 34 to better understand the interplay between macroscopic capillary pressure and saturation. It predicts that p_c is high when the water saturation is small and decreases with increasing water saturation. In a dynamic (non-steady state flow) saturation experiment, as performed in this study, p_c is not exactly given by the macroscopic pressure difference so a dynamic equation for the saturation changes should be used instead (Udey 2012). However, even in such an advanced theory, a CPS relation needs to be assumed.

The macroscopic expression of the capillary forces can also impact ultrasonic velocities. In a porous medium with air and water heterogeneously distributed, macroscopic fluid patches can be formed (Toms-Stewart et al. 2009; Lebedev et al.

2009). The surface-tension at the air-water interface at the pore scale gives rise to an overall stiffening of the fluid patch at the macroscale. A macroscopic surface tension (per unit area), the membrane stiffness W, can be formulated as (Tserkovnyak & Johnson 2003)

$$\mathrm{W} = \mathrm{s}\frac{\gamma}{\mathrm{k}} \tag{26}$$

where k is the permeability and s is a shape factor (accounting for the pore space geometry). In the context of macroscopic fluid patches, the membrane stiffness W gives rise to fluid patch stiffness

$$\widetilde{\mathrm{W}} = \mathrm{W}\phi^2\frac{\mathrm{V}}{\mathrm{A}} \tag{27}$$

where ϕ is the porosity and A/V is the specific surface of the fluid patches, that is their interfacial area per unit volume. As $\widetilde{W}$ increases, the GW undrained bulk modulus also increases (Tserkovnyak & Johnson 2003). Hence, the ultrasonic wave velocity increases. While s, k, γ and ϕ are assumed to be constant (which is only approximately correct for the limestone sample), a re-organization of the macroscopic fluid patches accompanied with a specific surface change can lead to either a decrease or increase of the P-wave velocity. Only if the patches become very small (the resulting specific surface would be very large) then the macroscopic effect of capillary forces on the acoustic velocity will vanish ($\widetilde{W} \to 0$) and the GW undrained bulk modulus will be recovered.

Apart from the capillary number, there are other characteristic numbers that define the flow regime. The viscosity ratio, M, the ratio between the viscosities of the displaced phase (residual fluid) and displacing phase (injected fluid), classifies the stability of the fluid flow. Flow stability is an essential requirement for the development of an efficient displacement of the residual fluid (Yortsos & Huang 1986). In water imbibition,

$$M = \frac{\mu_{displaced\ phase}}{\mu_{displacing\ phase}} = \frac{\mu_{air}}{\mu_{water}} \tag{28}$$

If $M > 1$, the fluid displacement is unstable and fingering occurs. In our case $M \ll 1$ $\left(M \sim 10^{-5}/10^{-3} = 10^{-2}\right)$. Therefore our fluid displacement is stable (Riaz et al. 2007). This is visually confirmed by the CT scans of the saturation front (Figure 27).

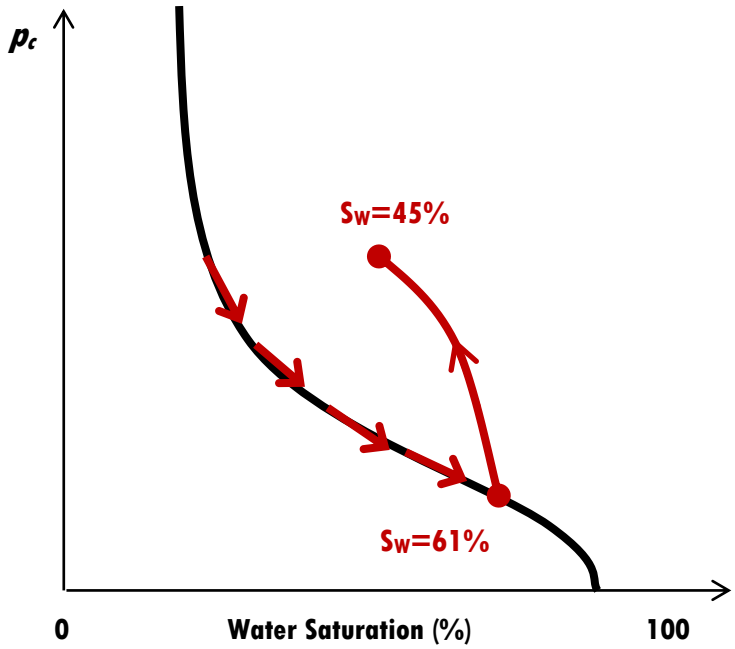

Figure 34 Qualitative behaviour of the macroscopic capillary pressure (p_c) - saturation relation. p_c decreases with increasing water saturation, S_W, during the initial imbibition (following the red arrows). After decreasing the injection rate, p_c decreases with increasing S_W, from 61% to 45%. Adapted from Katz et al. 1966.

3.4.2 EVOLUTION OF THE P-WAVE VELOCITY & THE WATER SATURATION

Four distinct stages can be observed in the evolution of the P-wave velocity (V_P) and the water saturation (S_W) at the two ultrasonically monitored positions C and M. All the stages were observed on both HIE and VIE. The results of the VIE are used as a representative example.

Stage 1

As the saturation front, visible in the X-ray CT scans, approaches (but has not yet penetrated) position C, V_P decreases by 26 m/s (Figure 27 and 31, between points [A] and [B]).

This velocity reduction can be interpreted as a *moisture weakening effect*. The macroscopic capillary pressure assumes its highest value at low S_W, i.e. at the beginning of the imbibition. Then, a small fraction of water is sucked up in thin capillaries and creates a minute amount of saturation ('moisture') ahead of the saturation front, thereby creating a capillary fringe. This moisture causes a weakening of the limestone matrix in the capillary fringe and results in a skeleton bulk modulus decrease. Thus V_P decreases.

At the monitoring position M, the same behaviour can be observed after some delay.

Stage 2

When the saturation front penetrates position C, an initial decrease of V_P is observed (Figure 27 and 31, between points [B] and [C]), followed by a steady increase (Figure 27 and 31, between points [C] and [E]).

At this stage, the change of V_P reflects the competition between the increase in the effective fluid density and in the effective fluid bulk modulus. Both increase with increasing S_W. First, V_P decreases as the increase in fluid density is more impacting than the increase of the bulk modulus. Thereafter, the increase of V_P is dominated by the increase of the bulk modulus. This behaviour is predicted by the GW theory.

There were no attempts to model this results but the effect is well described in other publications (e.g. Toms et al. 2006).

Stage 3

Now the injection rate was changed from $Q = 2$ mL/h to $Q = 0.2$ mL/h. This is a ten-fold decrease. At position C, near the base of the sample, S_W decreases continuously while V_P first decreases and then increases until the velocity prior to the injection rate change is recovered (Figure 29 and 31). This behaviour can be explained as follows. Decreasing the injection rate decreases the macroscopic capillary pressure in the region behind the front and hence decreases the saturation (red path in Figure 34). This is due to the redistribution of the water and air until a new quasi-static equilibrium is reached. Some of the water that entered the larger pores at the higher injection rate will drain back downwards under gravity, while other portions of water will migrate into surrounding smaller pores by spontaneous imbibition (and this flow can be upwards). Moreover, the trapped gas that has super-atmospheric pressure will change configuration so as to attain atmospheric pressure equilibrium again. These bubbles of air must of course expand in that process, reducing the local water saturation. The change of saturation can be envisaged as a spatial shift of the capillary fringe. A continuous reduction in saturation at levels close to the injection point, even when water continues to be pumped in slowly, suggests that the net movement of water from position C, at least over several hours, is upwards, making the capillary fringe wider when the injection rate is small than it was when the injection rate was ten times higher. The driving force for this reconfiguration is a combination of capillary suction from small pores becoming wetted by water at the top of the fringe plus expulsion of water from the decompression of trapped air pockets. The initial stage of this saturation reduction causes a decrease in the effective fluid bulk modulus and thus a decrease of the undrained bulk modulus. According to the GW theory V_P decreases (as observed in Figure 31).

The velocity increase that then follows (while S_W keeps decreasing) is more intriguing. It cannot be explained by simple effective medium theory but it can be explained with the concept of fluid-patch membrane stiffness in the presence of

capillary forces. The redistribution of water and air during the capillary fringe shift can be associated with the creation of larger air patches. This is due to coalescence of patches facilitated by the decrease in the capillary pressure gradient. Larger patches imply a decrease in the fluid patch specific surface and, according to Equation 27, an increase in the membrane stiffness. This leads to an increase in the GW undrained bulk modulus and hence to an increase in V_P (even though S_W decreases, Figures 29 and 31). However, an increase of fluid patch sizes could not be seen in the CT scans because of the low spatial resolution of the CT scans.

At position M, higher in the sample, a different V_P vs. S_W behaviour is observed. V_P first increases sharply and then decreases, returning to the original velocity prior to the injection rate change. Remarkably, S_W remains practically constant at approximately 39%. Though the decrease of the injection rate implies a decrease of S_W (since the macroscopic capillary pressure increases, Figure 34), the relatively large distance to the saturation front (as compared with position C) implies the existence of small capillary pressure gradients. Hence, there is a negligible change of S_W. All the effects seen in the ultrasonic waveforms must be the result of relatively subtle readjustment of fluid contents from larger to smaller pores within the capillary fringe. Interestingly, there is a sharp increase in V_P followed by a more gradual decrease (see detail box in Figure 31). In the light of Equation 27, this would imply that initially the patch sizes increase so that V_P increases and then the patch size become smaller and smaller until the capillary effect vanishes and the GW velocity is recovered. Again, the quality of the CT scans precludes the direct observation of such patch size changes.

Stage 4

Now the injection rate is switched back to the original value, $Q = 2$ mL/h. Both, S_W and V_P increase at positions C and M (Figure 29 and 31). Towards the end of the experiment, S_W at both positions becomes comparable. V_P is then almost independent of the injected water volume; however they attain different values at the two monitoring positions that can be related to the different baseline values in the dry state. The increase of S_W and $V_P$is related to the increase of volume of water accompanied with an increase of the effective fluid bulk modulus according to the

GW theory (analogue to the behaviour of Stage 2). Again, these states at the two positions C and M will be in dynamic equilibria, i.e. they will have a different configuration, size and internal pressures of the entrapped air bubbles than in the no-flow case where capillary and gravity forces are balanced in static condition (note that any trapped air is still out of gravity equilibrium, so all unsaturated states are metastable in this respect). If there were no entrapped air at either of the positions then the ultrasonic responses under static and dynamic conditions would be indistinguishable, and in the case of very high S_W, where the air is present in only a few scattered bubbles, large differences in ultrasonic waveforms between static and dynamic conditions would not be distinguishable either.

It is interesting to note that all four stages described here have been observed on sandstones (Chapter 2). This gives us some confidence that the observations are not an artefact of the current experiment but might reflect generic behaviour of rock-fluid interactions.

3.4.3 INFLUENCE OF GRAVITY

The influence of gravity is visible when the pattern of the evolution of S_W and V_P for vertical (VIE) and horizontal (HIE) position are compared (Figures 32 and 33). The following generalization can be made:

1. The saturation front reaches the ultrasonically monitored position first on the horizontal configuration. When this happens, both S_W and V_P change their evolutionary progress.
2. At low injection rates, higher values of S_W and V_P are reached on the horizontal configuration;
3. The increase of S_W and V_P when the injection rate was increased was higher for the vertical configuration.

These features are connected to the geometry of the saturation front. In VIE, the saturation front is more compact due to the influence of gravity while it tends to be more diffusive when the direction of injection is perpendicular to the gravity (HIE). In the VIE, the gravity decreases the pressure gradient created by the injection rate, working as an opposite force to capillarity forces. In the HIE, there is a horizontal component in the resulting force due to the pressure gradient that helps capillarity forces surpass gravity forces and transport the water farther ahead. When the injection rate was decreased, for VIE, S_W and V_P increased immediately and kept increasing for 1 hour, followed by a constant evolution. For HIE, there was a slow continuous increase of S_W and V_P up to the end of the experiment. This is due to a less compact saturation front that created a more gradual response in S_W and V_P due to the change of injection rate.

3.5 CONCLUSIONS OF CHAPTER 3

It was clear from the experiments that acoustic wave velocities are very sensitive to the change of the injection rate and that small variations in water saturation can create significant changes in the acoustic response (at ultrasonic frequencies). A decrease of the P-wave velocity in the beginning of the imbibition was observed as the saturation front approached the monitored positions. This was followed by an increase in P-wave velocity as the saturation front started crossing the monitored position. Decreasing the injection rate decreased the P-wave velocity and water saturation, immediately and for a significant period of time. After a while, the P-wave velocity starts increasing while the saturation keeps decreasing. Increasing the P-wave velocity, increase both the P-wave velocity and water saturation. All these features were observed in previous work on a sandstone. Here, the magnitude of the effect was more pronounced (Chapter 2).

A decrease in P-wave amplitude was observed with the presence of water and remained with the continuous injection of water. This behaviour was also observed for the sandstone in Chapter 1.

The direction of injection relative to the direction of the gravity force influenced the fluid distribution and, consequently the evolution of the acoustic wave velocity and water saturation. When the sample was horizontal, the saturation front was more diffusive while the vertical injection promoted a denser, more compact saturation front. The advancement of a more compact saturation led to more abrupt changes in the values of the water saturation and the P-wave velocity while the diffusive saturation front created smoother transitions.

There is a strong variability in porosity and permeability due to the structural heterogeneity of the limestone, which led to an inhomogeneous water distribution. The evolution of the capillary pressure and relative permeability is very influenced by local porosity and permeability variations. Though, generally, the water permeability increase with the imbibition of water, the displacement is only possible when there is communication between neighbouring pores. It is evident from the CT scans, that significant parts of our sample were not hydraulically connected. The structural analysis showed that areas of low porosity reached high water saturations. This discrepancy enhances how important it is to consider not only the porosity but

also the spatial distribution and connectivity of the pores. The porosity and permeability measured using conventional techniques is an average over the whole sample volume and alone they cannot predict the ability of the sample to store and conduct the injected fluid. This is important as connectivity and spatial distribution of the pore-network are relevant features when dealing with reservoir quality indicators such as oil and gas production or CO_2 storage efficiency. X-ray CT scanning is, therefore, an essential tool in evaluating connectivity of the porous network of a rock.

.

CHAPTER 4
VARIABLE INJECTION RATE: SANDSTONE #1

All the stages described in Section 3.4.2 for the limestone were also observed on the Otway Sandstone #2 of Chapter 2. However, the methodology of Chapter 2 was different from the methodology of Chapter 3. Mainly: (1) the injection was stopped for a considerable period of time in the sandstone experiment and (2) the sandstone was in a horizontal position (i.e. with the direction of injection perpendicular to gravity). To be able to compare the response of the P-wave velocity and the water saturation with the change of injection rate between the limestone and the Sandstone #1, the same methodology of Chapter 3 was applied to Sandstone #1 (initially used in Chapter 1 for constant injection rate experiments).

The **sandstone** in study was set for vertical position, i.e. with the direction of injection parallel to gravity. Distilled water was injected at the high injection rate (HIR) of 2 mL/h for approximately 3 hours. Then, the injection rate was decreased to 0.1 mL/h (low injection rate, LIR) and kept for approximately 24 hours. After, the injection rate was increased back to the HIR of 2 mL/h until the end of the experiment.

4.1 RESULTS & DISCUSSION

Following the steps in Section 3.4.1, the fluid flow regime of this experiment was classified. The capillary numbers for each injection rate are:

- $Q = 2\ mL/h,\ C_a \sim 2 \times 10^{-9}$
- $Q = 0.1\ mL/h, C_a \sim 1 \times 10^{-10}$

All $C_a < 10^{-5}$ and therefore this fluid flow is dominated by capillary forces (Ding & Kantzas 2004). The viscosity ratio is $M \ll 1$ and the fluid displacement is stable.

Figure 35 shows a sequence of CT scans for the first 3 hours at the HIR. Here, the position of the saturation front relative to the ultrasonically monitored position C was observed (only position C was monitored). Figures 36 and 37 show the evolution of V_P and S_W with volume of water injected, respectively. The same 4 stages described in Chapter 3 are distinguishable:

Stage 1: As the saturation front approached the monitored position (Figure 35, between 0 and 1.8 mL of water injected), V_P decreased by 53 m/s (Figure 36).

Stage 2: When the saturation front started crossing the monitored position, V_P increased with increasing S_W after 1.8 mL of water injected (Figure 35).

Stage 3: When the injection rate was decreased from the HIR to the LIR, V_P and S_W decreased immediately. V_P decreased instantly but slowly, 36 m/s in 2h30 (Figure 35 and 36, between green lines). The initial decrease of V_P was followed by a sudden increase while S_W kept decreasing down to 51% (Figure 37). The redistribution of fluid caused by the change of injection rate prompted higher values of V_P at the end of Stage 3.

Stage 4: V_P and S_W increased slightly but steadily when the injection rate was increased.

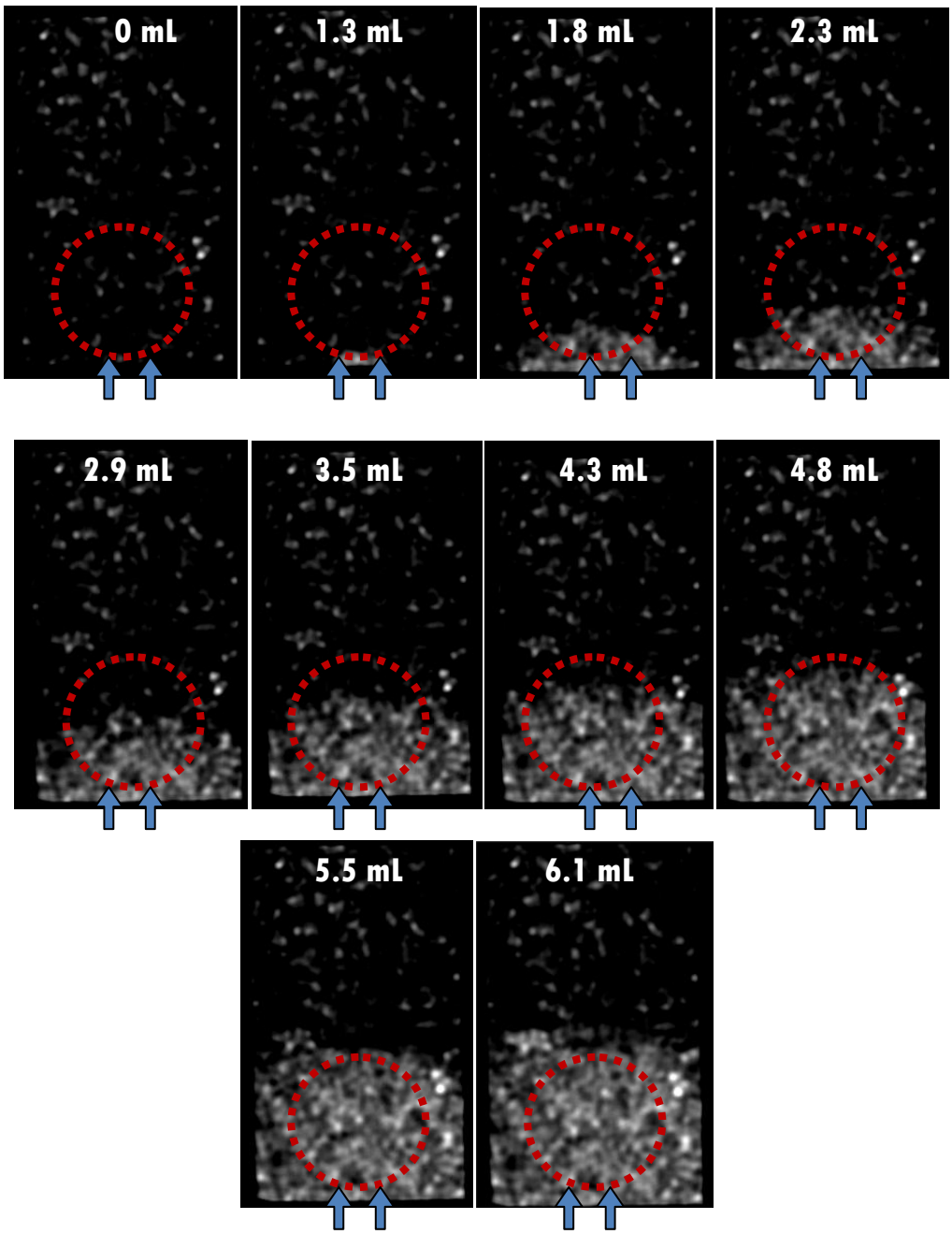

Figure 35 Sequence of CT scans from dry sample to 6.1 mL of water injected at the HIR. Red circle represent the area covered by the transducers in the CT scanning plane. Blue arrows indicate the direction of injection. No digital image processing was made, only contrast enhancement for better display of the saturation front.

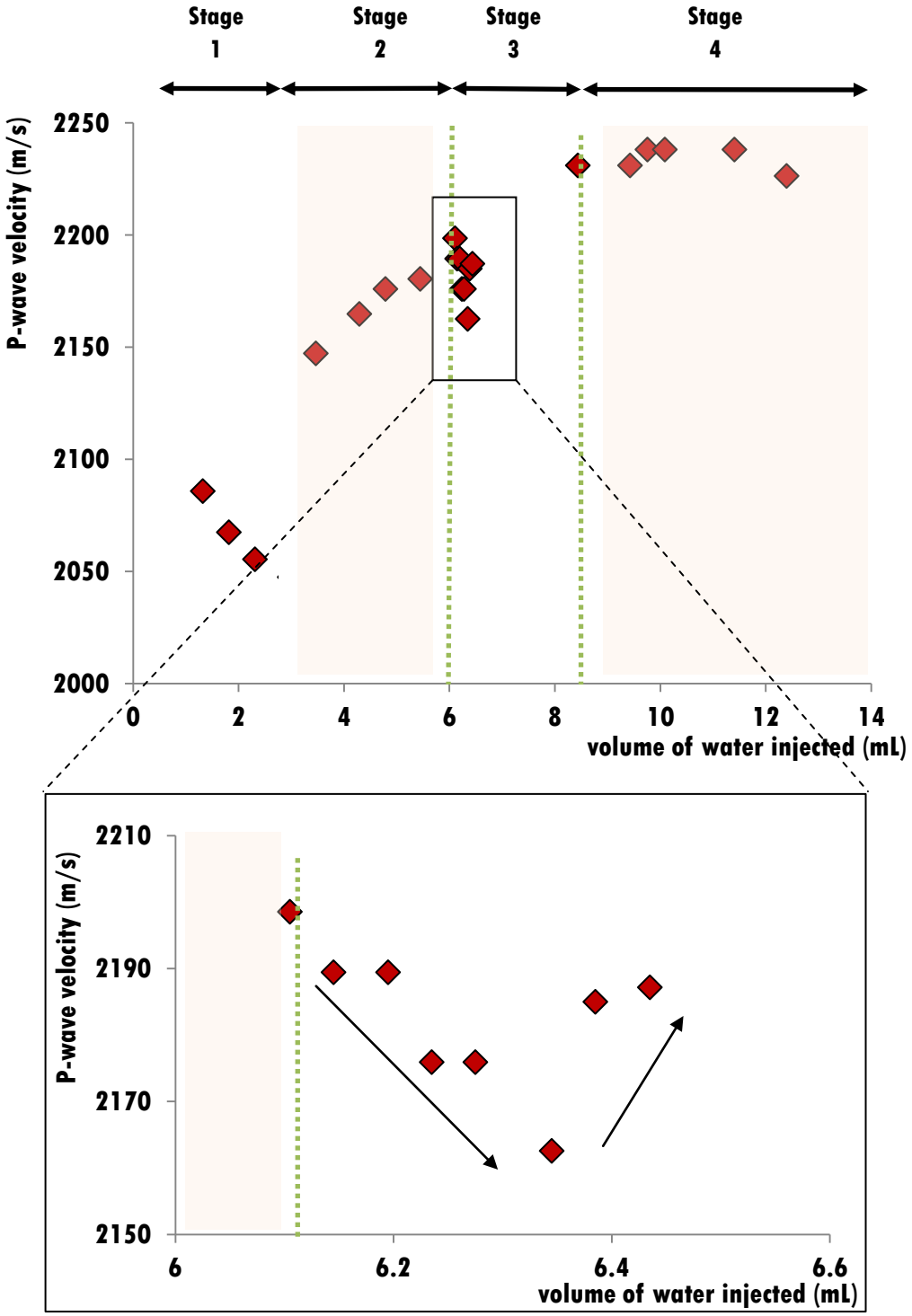

Figure 36 P-wave velocity (V_P) with volume of water injected. Note the initial decrease of V_P due to the approaching saturation front. **In the detail box:** decreasing the injection rate decreases V_P for 2h30min followed by a sudden increase. Green lines represent the moments when the injection rate was (first) decreased and (second) increased.

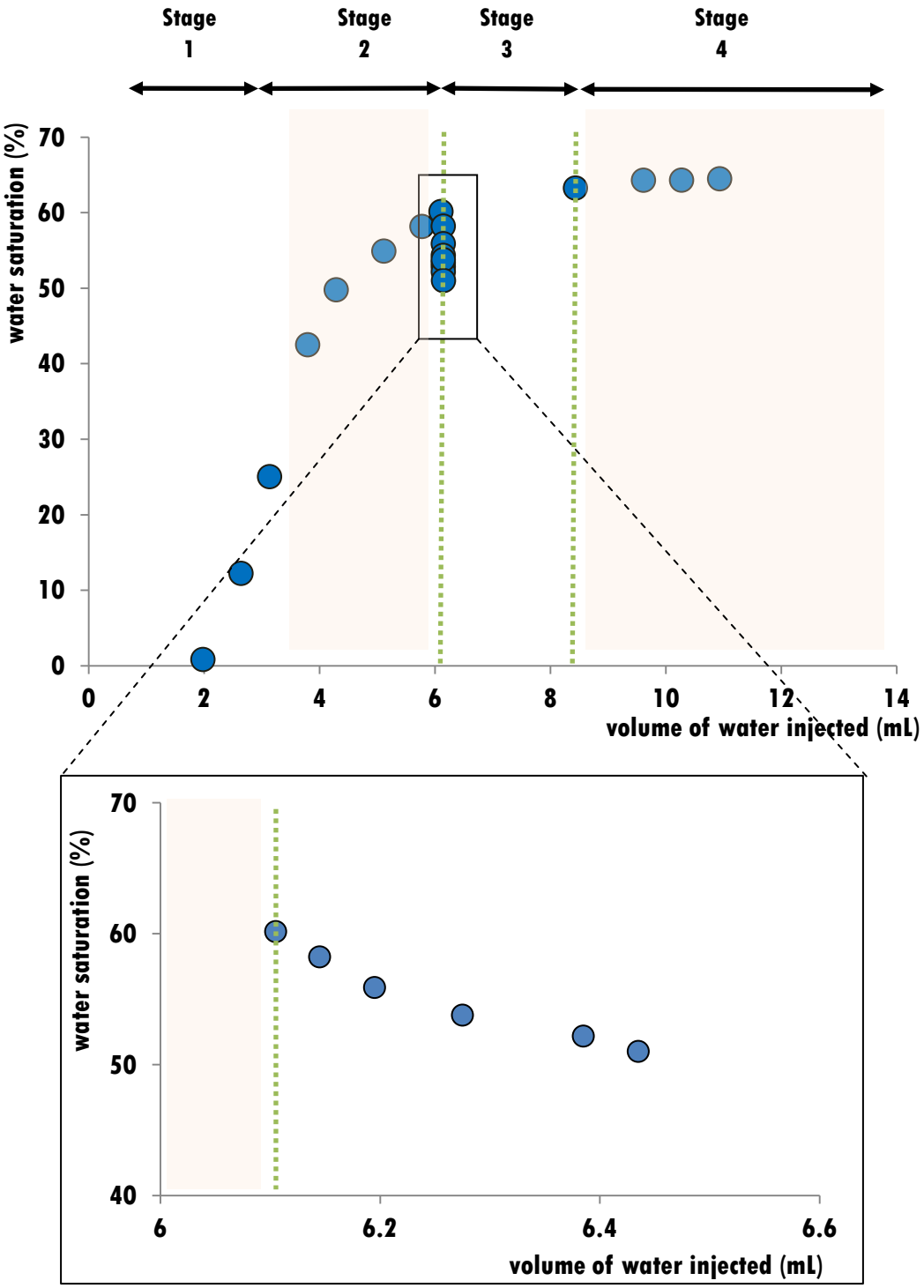

Figure 37 Water saturation (S_W) with volume of water injected. **In detail box:** decreasing the injection rate decreases S_W. Green lines represent the moments when the injection rate was (first) decreased and (second) increased.

4.2 CONCLUSIONS OF CHAPTER 4

All the stages described in Chapter 4 match the stages found in Chapter 2 (Sandstone #2) and Chapter 3 (limestone). A decrease in P-wave amplitude with the presence and continuous injection of water was also observed (data not shown).

Differences between Sandstone #1 and #2 were also spotted. Sandstone #1 presented variations higher in absolute value for the P-wave velocity and therefore the decrease and increase with decreasing and increasing of the injection rate, respectively, was more pronounced. Though with similar petrophysical properties the higher variations in Sandstone #1 might be due to softer, more compressibility matrix.

I.2 SUMMARY OF PART I

Forced imbibition in reservoir samples was performed at ambient conditions in order to study the evolution of the P-wave velocity and water saturation and fluid distribution with (1) the presence of the injected fluid at (2) different injection rates. The methodology of simultaneously acquiring acoustic waves and CT scans was useful in matching the intrusion of water with specific responses of both the P-wave velocity and water saturation. In all the performed fluid flow experiments, capillary effects had a significant dominance. The displacement of the saturation front was stable, i.e. the saturation front was planar, no fingering occurred as it was observed in the CT scans.

All the experiments showed a dependence of the acoustic response and the evolution of water saturation with the presence of water and with the injection rate. Moreover, for both sandstones (Chapter 2 & 4) and limestones (Chapter 3), a similar pattern was observed in the evolution of the P-wave velocity and water saturation with the change of injection rate. More particularly, four stages of rock-fluid interaction were distinguished. The first stage is related to the presence of a moisture front that caused the weakening of the rocks' matrix, resulting in a decrease of the P-wave velocity. The second stage is related to the intrusion of the saturation front in the ultrasonically monitored position. Initially, the P-wave velocity decreased and then started increasing while the water saturation kept increasing. Here, a competition between the increase in the effective fluid density (leading to a decrease of P-wave velocity) and in the effective fluid bulk modulus (leading to an increase in P-wave velocity) is in play. At the third stage, upon decreasing the injection rate, both the P-wave velocity and water saturation decrease immediately. After a while, the P-wave velocity increased while the water saturation kept decreasing. This could be related to changes in pore pressure that allowed air bubbles and water patches to re-distribute and spread (decreasing the local bulk modulus, decreasing the P-wave velocity) and then coalesce (increasing the bulk modulus, increasing the P-wave velocity). At the last (forth) stage, when the injection rate was increased, the P-wave velocity and water saturation increased steadily. This increase is directly related to the increase in volume of water leading to an increase of the effective fluid bulk modulus (similar to stage 2).

Another overall outcome (for both variable and constant injection rate and for sandstones and limestones) is that the same water saturation can match to different P-wave velocities. This reflects how acoustic wave propagation is sensitive to spatial fluid distribution, more than to the actual water saturation.

In Chapter 1, specific evolution of the P-wave velocity and water saturation at different injection rates were spotted. The high injection rate promoted a flat, compact saturation front and a fast increase in P-wave velocity and water saturation while the low injection rate promoted a diffusive saturation front and both, P-wave velocity and water saturation, increased slowly as water was injected. The natural imbition revealed a pattern on the evolution of P-wave velocity and water saturation similar to the high injection rate, sustaining a flat saturation front. For the natural imbibition there was a continuous decrease of the imbibition rate revealing that at a certain point gravity forces overcome capillary forces.

An injection rate much higher than the natural imbibition rate is not the most efficient in the production of the residual fluid whereas an injection rate close to the natural imbibition rate is the most efficient. A low injection rate is efficient at expelling the residual fluid (in this case, air) but only over a long period of time.

In Chapter 3, the CT scans of the limestone revealed structural heterogeneities that influenced the fluid distribution. A flat, piston-like displacement was not observed. Surprisingly, areas of low porosity reached high water saturations and areas of high porosities reached low water saturations. This discrepancy enhances how important it is not only the number of voids but also their spatial distribution and connectivity.

Two positions along the limestone's length were acoustically monitored to study how the evolution of the P-wave velocity is invariably related to the position of the saturation front. For the position closest to the point of injection, the decrease of P-wave velocity and water saturation with the decrease of injection rate was immediate. For the position further from the point of injection, the response of the P-wave velocity to the decrease of injection rate was delayed by almost one hour. At the moment the injection rate was changed, the saturation front had not yet reached this position. Hence, there is a negligible change of water saturation that continued with the continuous slow injection rate. However, there is an influence in

the P-wave velocity due possibly to the presence of water ahead of the saturation front (driven by capillary forces).

The influence of gravity on the type of the saturation front was also studied by comparing vertical- and horizontal-oriented injection, i.e. when the direction of injection was parallel and perpendicular to gravity, respectively. When the injection was vertical, the saturation front was compact (higher local water saturation) while it was more diffusive (lower local water saturation) in the horizontal configuration.

There is an important difference between the sandstone and limestone experiments: the change in the P-wave velocity with the presence of water and due to the change of injection rate is higher in absolute values for the sandstones than for the limestone. This behaviour is explained by the stiffer, less compressibility matrix of the limestone in comparison with the softer, more compressibility matrix of most sandstones. Sandstones are granular and, except where very strongly cemented by quartz overgrowths, low water saturations are mainly located in the grain contact regions where pore apertures are thin, making them sensitive to stress. Many sandstones also contain clays in the load-bearing contact regions and this further amplifies this sensitivity. Many limestones, rather than being composed of incompletely cemented grains, have a mouldic type of porosity and a relatively solid carbonate mineral skeleton and this why it is typically more challenging to observe 4-D seismic responses in carbonate reservoirs than in clastic reservoirs. The Savonnières limestone studied is of this mouldic type, but it also contains regions of microporosity that gives it a moderate level of sensitivity to stress and a relative complex response to changes in water saturation.

PART II
TESTS UNDER CONFINING PRESSURE

II.1 MOTIVATION

The tests performed in Part I were productive in providing good quality and quantity data regarding water imbibition in dry samples at ambient conditions. It was also successful in applying the method of simultaneous X-ray CT scanning and acoustic monitoring. They were also important in the study of phenomenological events in fluid flow experiments. However, for quantitative analysis, *in situ* conditioned simulations must be performed. The next step was to perform the same simultaneous acoustic monitoring and image acquisition method but with the samples **under confining pressure**. For that purpose, a pressure cell was built, made of polyether ether ketone, frequently named as "PEEK", a robust thermoplastic able to endure high pressures. PEEK is also, importantly, transparent to X-rays making it suitable for the image acquisition method. An acoustic wave monitoring system is also part of this cell. Two transducers of frequency were glued to the walls of the cell, in the middle of its length. The potential of the pressure cell was explored regarding: (1) the **injection of oil** in dry samples (and compare it to the water injection in Part I) and (2) **the study of** the acoustic response and fluid distribution in **carbonate rocks**.

Acoustic monitoring has a key role in reservoir characterisation, especially in the detection of reservoir fluids, delineate their distribution and follow their displacement during production and recovery processes. However, reservoirs are a very heterogeneous and multi-phase media (a combination of air, water and/or gas) creating complex fluid distribution and thus generating competing wave reflections, attenuations and dispersions (Li, Zhong & Pyrak-Nolte 2001). Therefore, for simplification purpose, the injection of oil in dry samples was performed and the P-wave velocity/fluid saturation dependence was compared to the evolution presented in Part I (injection of water in dry samples).

The viscosity of the oil was taken in consideration in the experiments. Oil offers more resistance to flow than water. Therefore, the fluid flow experiments should be performed on samples with high porosity and permeability. Low permeability prevents the oil to flow and consequently a high pore pressure is imposed and fractures can be formed. Then, the structure of the sample will be compromised and

porosity will change throughout the imbibition. Then several additional controlling factors for acoustic propagation that are beyond the scope of our experiments will be in place. Also, adequate solid rocks for oil injection are difficult to find in nature because natural high porosity and permeability rocks (over 1 D) tend to be very sandy and grainy (non-consolidated rocks). They are not suitable for under-pressure experiments as they would disintegrate easily and change significantly their density and porosity. Therefore, **synthetic sandstones** made of a compressed mixture of sand, water and cement were used. They are suitable for experiments dealing with the injection of oil since they are rocks well consolidated yet with high permeability (~10 D) and porosity (~30%) and their composition is well known. The synthetic sandstones used, called "CIPS" (Calcite *In situ* Precipitation System) were chosen due to their high permeability (K_l = 9 and 10 D for CIPS #1 and CIPS #2, respectively). This facilitated the experiments in terms of (1) time of performance (fast imbibition of the injected fluid) and (2) the injected fluid (under-pressure) easily travelled the sample without inducing structural damages (as opposed, for example to tight, low-permeable sandstones were the fluid would have to "break" in into the sample to create pathways). A detail description of the preparation of these artificially cemented sandstones can be found in Yang et al. 2012.

Carbonates are sedimentary rocks made of particles (composed >50% carbonate minerals) embedded in a cement. As they are formed by precipitation or by accumulation and lithification of fragments of pre-existing rocks or remains of organisms, they can be very heterogeneous in mineralogy and in texture and it is quite usual that they present sedimentary structures like bedding or layering. Carbonate rocks form at least 60% of the world's known hydrocarbon reservoirs therefore rock characterization and acoustic wave velocity analysis of carbonates are very important in the petroleum reservoir characterization and seismic exploration. However, their complex porosity, lithology and texture derived from their formation makes them particularly challenging when performing acoustic wave monitoring during fluid flow experiments. Mainly, their stiff matrix makes them less responsive to the compression induced by the passing acoustic wave moreover in the presence of partial fluids as they weaken the acoustic signals (Lumley 2001). As a consequence, not may acoustic monitoring studies have been

performed on carbonates even less those that combined X-ray CT scanning (see Chapter 3 for a literature review). Therefore, it was part of this thesis to provide velocity-saturation relationships on carbonates and relate them to fluid distribution (as done in Part I) with added pressure effect.

Since this was the first time the methodology of simultaneous acoustic monitoring and X-ray CT scanning was applied to carbonates in our laboratory using the PEEK cell, the fluid flow experiments were simplified by injecting water into dry samples at constant injection rates. The water/air density contrast allowed distinguishing the P-wave arrival time of several partially water-saturated phases. KCl was added to the distilled water to improve the CT contrast between the carbonates' matrix and pore network (Rangel-German & Kovscek 2002). Pore pressure was applied at the later stages of the "salty" water injection to aid the full saturation of the samples.

Part II is structured as follows: first, the methodology applied to water and oil injection in samples under confining and pore pressure is explained in Section II.1. Results of the fluid flow imbibitions performed on two synthetic sandstones and three carbonates are presented and discussed in Chapter 5 and Chapter 6, respectively, of Section II.2. The most important results of the under-pressure tests and how they complement the results of Part I are discussed in Section II.3.

II.2 METHODOLOGY

Figure 38 shows the experimental setup in the table of the X-ray CT Scanner. It includes (1) the PEEK cell, (2) a pressure pump through which hydraulic oil was pumped into the PEEK cell up to a pre-defined confining pressure and (3) an injection pump where the pore pressure and the injection rate were set. The oscilloscope and the pulser/receiver were outside the CT scanner room. In this way, the record of the P-waves was done without having to enter the room and stop the X-ray CT scanning.

The X-ray beam does not have enough energy to scan along the long axis of the sample as it happened it Part I. Therefore the system could only be set for horizontal injections (direction of injection perpendicular to gravity). So, only radial or angled scans could be performed. The scan over an angle was chosen (represented by θ in Figure 39) so the longitudinal displacement of the saturation front could be visualized. The angle θ is between the long axis, $\vec{L}$, and the scanning axis of the X-ray beam, $\vec{B}$ (Figure 39). This resulted in ellipse-shaped CT scans (Figure 40). As in the experiments of Part I, the table of the CT scanner did not move, resulting in 2D CT scans of the same area.

To estimate the saturation of the injected fluid, Equation 15 (for water injection) and 16 (for oil injection) were applied. The saturation was averaged over a circular area in the middle of the CT scan, representative of the area monitored by the transducers in the CT scanning plane (red circle in Figure 40). In the configuration shown in Figure 39, the direction of injection was perpendicular to the gravity vector and the fluid propagated from left to right of the CT scans in Figure 41. The "whiter" areas indicate the presence of water (higher CT numbers).

The samples were placed inside the PEEK cell and were subject to lateral confining pressure and pore pressure. The confining medium in the cell was hydraulic oil and the samples were isolated from this medium by means of a rubber sleeve. The cell could reach up to 10 MPa, simulating pressure conditions of rocks situated at the subsurface (~12 MPa of effective pressure). A pair of transducers was glued to the surface of the cell to monitor P-waves. Calibration of the cell is explained in detail Appendix A.

Experiments were performed in two **synthetic sandstones**, CIPS #1 and CIPS #2, and three **carbonates**, CB #1, CB #2 and CB #3. The main petrophysical characteristics of the samples are shown in Table 5: length (l) and diameter of the sample (D); bulk volume (V_b); weight (W); pore volume (V_{pore}); confining pressure (P_{conf}) at which the porosity (ϕ) and permeability (K_l) were measured.

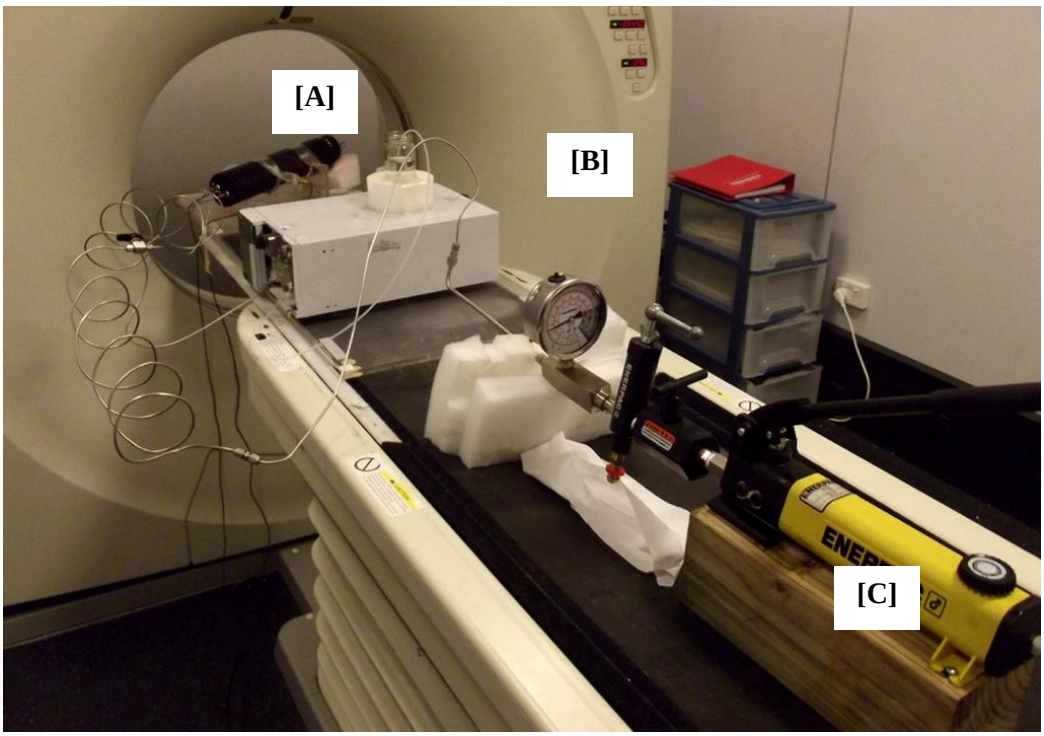

Figure 38 Experimental setup of Part II: **[A]** PEEK cell; **[B]** injection pump and **[C]** pressure pump. The pulser/receiver and the oscilloscope set outside the X-ray CT scanner room.

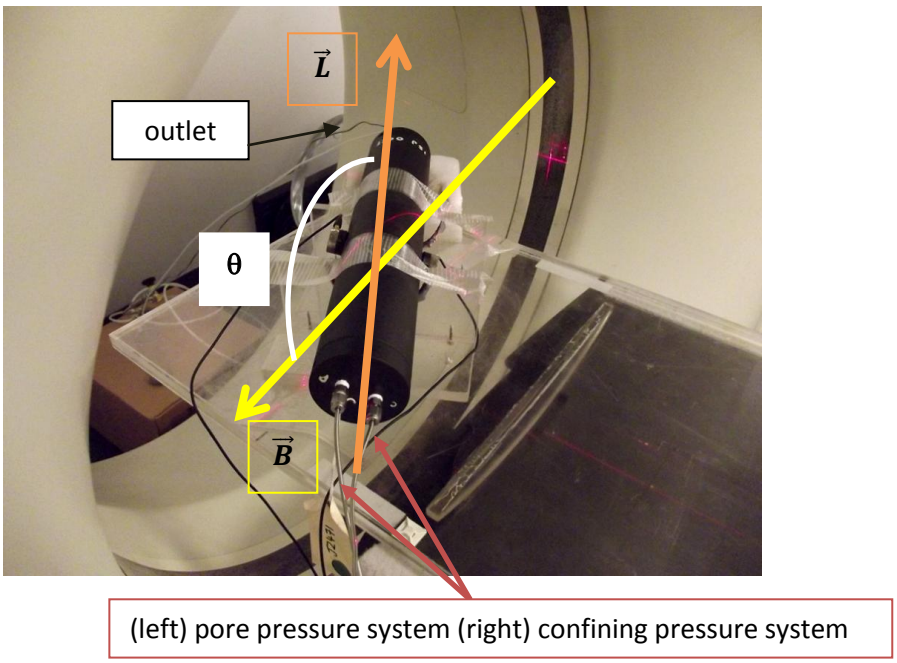

Figure 39 PEEK cell, connected to a pair of transducers, fixed to the CT scanner table in an horizontal position. $\vec{L}$ is the axis along the length of the cell and $\vec{B}$ is the axis of the directed X-ray beam. θ is the angle between them. The outlet controlled the exit of the injected fluid.

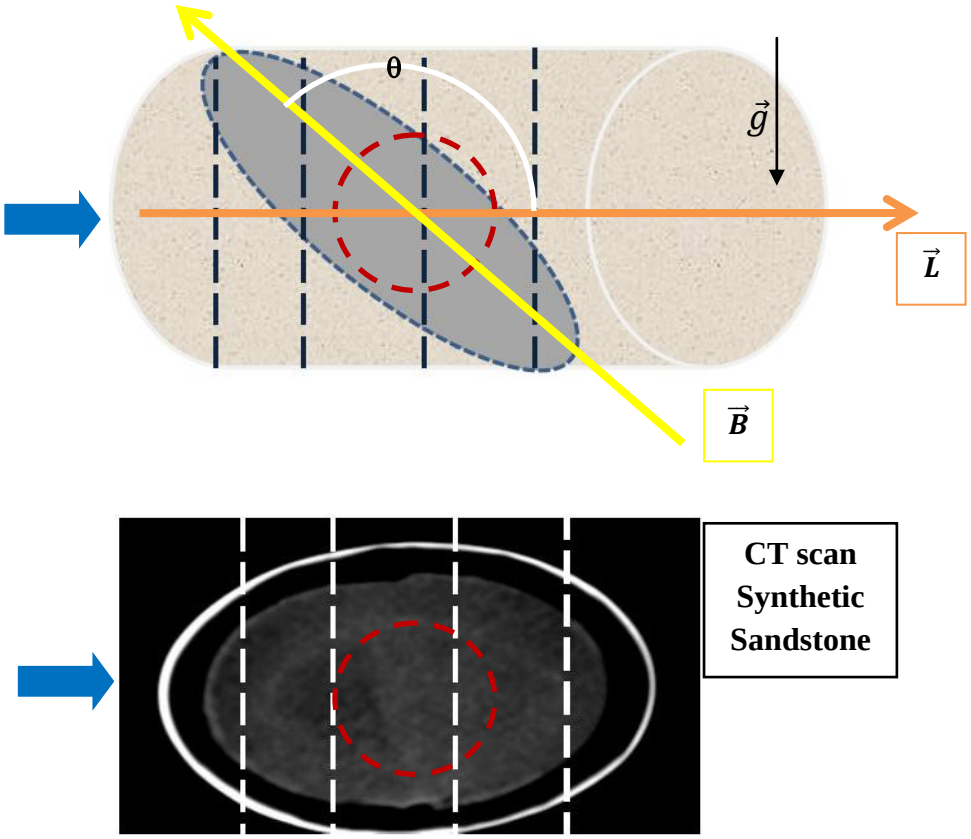

Figure 40 The angled CT scanning results in an ellipse-shaped scan. Blue arrow indicates the direction of injection (perpendicular to the gravity vector, $\vec{\mathbf{g}}$). $\vec{L}$ is the axis along the length of the cell and $\vec{B}$ is the axis of the directed X-ray beam. θ is the angle between them. Red circle, located in the middle of the scanned object, represents the acoustically monitored position where the local saturation was estimated.

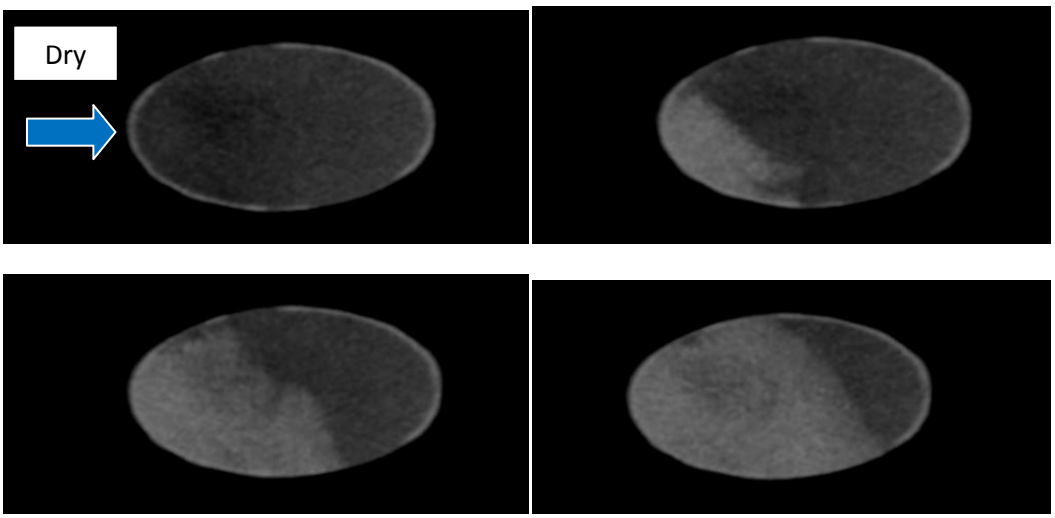

Figure 41 Sequence of CT scans of a synthetic sandstone, starting when the sample was dry. Water propagates from left to right of the CT scan, as a piston-like displacement. The CT numbers increase with the presence of water, "whitening" the areas they fill. Blue arrow indicates direction of injection.

	L (cm) D (cm)	V_b (cm^3)	W (g)	V_{pore} (cm^3)	P_{conf} (psi)	ϕ (%)	K_l
CIPS #1	7.75 3.85	90.2	172.7	21.9	498	24.3	9 D
CIPS #2	7.50 3.85	87.3	162.4	24.0	489	27.6	10 D
CB #1	7.15 3.81	81.6	161.3	20.9	532	25.7	52 mD
CB #2	6.64 3.80	75.4	154.1	17.6	531	23.4	5 mD
CB #3	7.31 3.81	83.1	154.8	25.3	529	30.3	38 mD

Table 5 Main petrophysical properties of the synthetic sandstones (CIPS) and carbonates (CB).

II.3 RESULTS & DISCUSSION

CHAPTER 5
SYNTHETIC SANDSTONES

Different methodologies were applied to each sample:

CIPS #1

This was a trial test to see if the experimental setup and methodology worked properly and provided good data. Solely distilled water was injected. The first goal was to study the influence of fluid distribution on the evolution of the P-wave velocity and water saturation. The injection started at the rate of 2 mL/h and confining pressure at 5 MPa. Then, the injection was stopped for 17 hours. Next, *forced saturation* was performed with the intention of saturating the sample to 100% water saturation. For this, the injection rate was increased considerably to 20 mL/h with no pore pressure applied and confining pressure kept at 5 MPa.

CIPS #2

This sample was used for the particular injection of oil. A light oil was used, density 0.92 g/cm^3 and viscosity 33×10^{-3} Pa. s (to compare: water's density is 1 g/cm^3 and viscosity is $1 \times 10^{-3}\ Pa.s$). The average CT number of this light oil is $\overline{CT} = -160$ (note that $\overline{CT_{water}} = 0$ and $\overline{CT_{air}} = -1000$). The evolution of P-wave velocities and fluid saturation was studied with the sample under confining pressure and water and oil were injected. The evolution of those two parameters was then compared for two different fluids. The experiment was done in 2 phases:

- **Phase 1, Water Injection:** First, water was injected in a dry sample at the rate of 3 mL/h and the confining pressure 5 MPa. No pore pressure was applied (the outlet was open to ambient pressure). CT scans and P-waves were recorded simultaneously at several moments of the injection. This first part ended when the water exited the outlet. This was followed by performing forced saturation. The outlet was closed and the maximum pore pressure was set to 3 MPa while the confining pressure was increased to 8 MPa. This resulted in an effective pressure of 5 MPa, which was the same as the in first part of Phase 1. The injection rate was very high, 60 mL/h, to allow a fast saturation, in this case,

within 1 hour. The sample was then dried in an oven-vacuum for two days at 50˚C, followed by one day in vacuum without heating.

- Phase 2, Oil Injection: With the sample dry, the light-oil experiment was initiated. The same steps of the initial injection in Phase 1 were performed. However, after stopping the injection at approximately 8 hours, the experiment was only restarted after 12 hours. During this non-injection period, the system was in a relaxed state, no confining or pore pressure was applied. Then, the forced saturation was performed under the same conditions as Phase 1. The last CT scan was assumed to represent the stage at which the sample was 100% oil saturated. The P-wave dependence with pressure was recorded when the sample was dry and fully-saturated. In this way, the P-wave velocity dependence with pressure was evaluated and compared to the effect of the presence of fluids in the sample.

It was the initial purpose of this experiment to inject a heavy oil, with density and viscosity close to the ones found in reservoirs. However, the high viscosity of this type of oils was incompatible with our injection pump. The pump was not strong enough to displace the oil and most of the oil clanged to the walls of the injecting tube and did not move. This lead to several technical issues that were not resolved within the timeline of this project. Therefore, a light-oil with lower viscosity was chosen.

5.1 CIPS #1

Figure 42 shows the P-waveforms for (1) dry sample, (2) at the end of the injection at the rate of 2 mL/h (low injection rate, LIR), (3) before the injection was restarted at 20 mL/h (high injection rate, HIR) and (4) when the experiment ended. After 4 hours of injection at the LIR, the P-wave amplitude decreased considerably, by 60%, when comparing the amplitudes of the first positive peak between the blue line (dry sample) and the green line (after injecting 8 mL of volume of water). The P-wave amplitude decreased during the 17 hours of non-injection while the P-wave arrival time remained the same. Right before restarting the injection at the HIR, P-wave was recorded (purple line in Figure 42). At the end of the injection at the HIR, the fast imbibition of water induced an increase of the P-wave amplitude.

Figure 43 shows a sequence of CT scans from the beginning of the injection at the LIR to the end of the HIR. The entrance of the water was inside of the sample and not at the extreme left of the CT scan (as explained in Figure 41, it was expected that the displacement would go from left to right of the CT scan). At the end of the LIR, the fluid distribution was quite sparse, spreading over most of the scanned area (Figure 43-D). Only when the HIR was restarted, did the water fill the scanned position considerably ("brighter" white, i.e. more water accumulation). Here, the water spread preferentially in the directions of the borders of the CT scan. This sequence of CT scans shows that this high permeable sample, $K_l = 9\ D$, there had preferential pathways for the water to move that directed the fluid from inside of the sample to the borders.

Figure 44 shows the evolution of V_P and S_W with duration of injection. The evolution of S_W can be separated in two phases: steep increase, 29% *per* hour followed by a slower increase 7% *per* hour. The first step is due to the fact that the water filled the ultrasonically monitored position continuously for the first two hours and then it started entering peripheral areas, mainly following the direction of injection. This can be verified in Figure 45. When Figure 43-C is subtracted from Figure 43-B, a bright white lunar-shaped area stands out. This represents the area that was filled with water in those two hours of injection. Then, upon starting the injection at the HIR, S_W increased 25% *per* hour influenced by the high volume of water entering the sample. The increase slowed down considerably after reaching

S_W = 90%. The penetration of the saturation font into the monitored position (Figure 43-B and 43-B) influenced the evolution of the acoustic response: there was a "skip" in the continuous decrease of V_P, i.e., V_P increased by 19 m/s. After that, the decrease continued up to the end of the LIR, resulting in a decay of 407 m/s from the V_P when the sample was dry ($V_{P,dry}$ =3160 m/s). When the injection was stopped for 17 hours, V_P and S_W increased slightly, 32 m/s and 11%, respectively (Figure 44-E). Upon restarting at the HIR, the response of V_P was immediate and accentuated. V_P increased 201 m/s in 50 minutes, then increased sharply up to the final value of 3185 m/s.

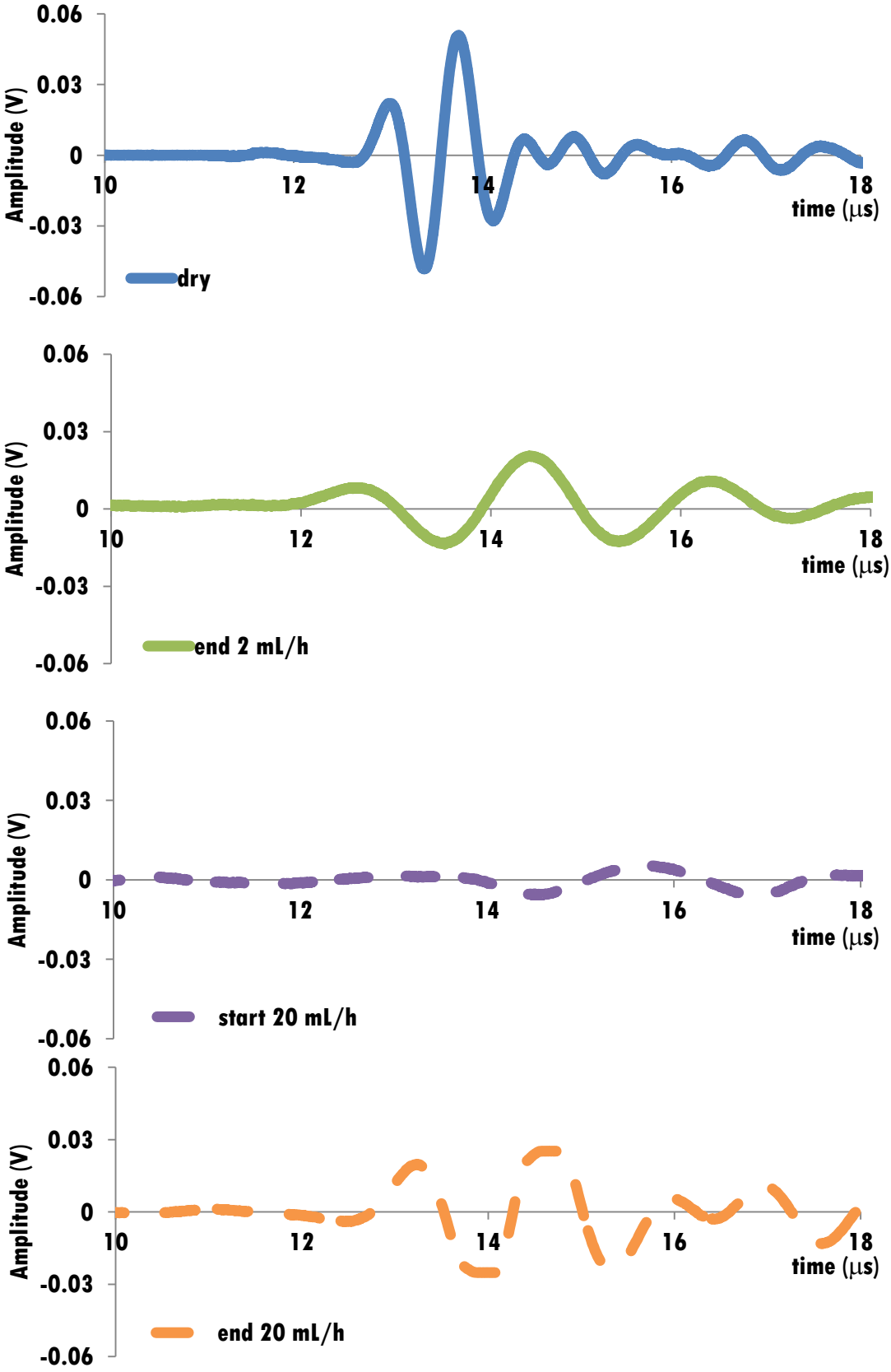

Figure 42 P-waveforms at the beginning and end of the injection at the rates of 2 and 20 mL/h, confining pressure: 5 MPa, no pore pressure. The same vertical scale is displayed for all plots to compare wave amplitudes.

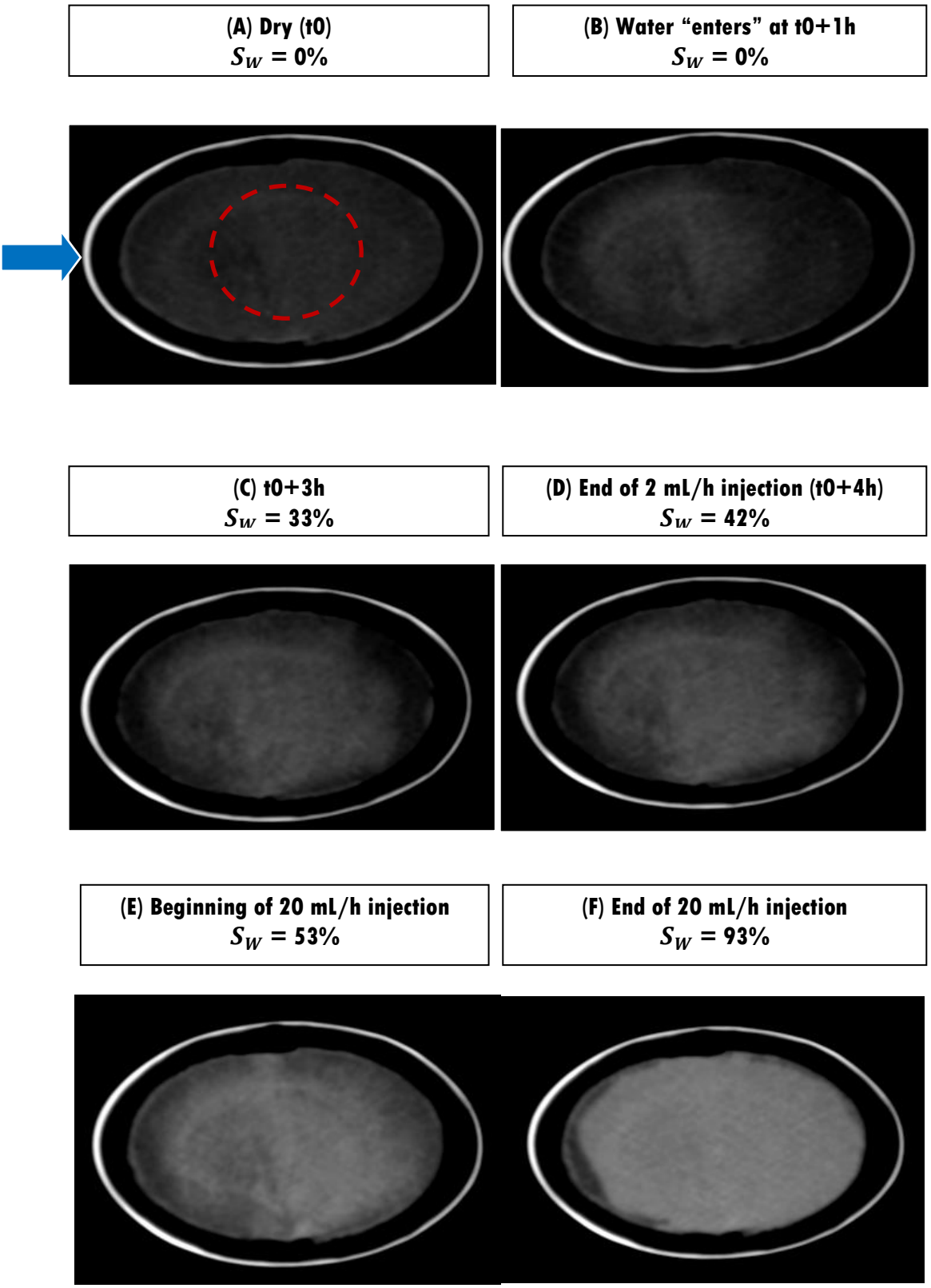

Figure 43 CT scans of CIPS #1 at the injection rates of 2 and 20 mL/h. Confining pressure: 5 MPa. Water saturation (S_W) also shown. Red circle represents the ultrasonically monitored position. Blue arrow indicates the direction of injection.

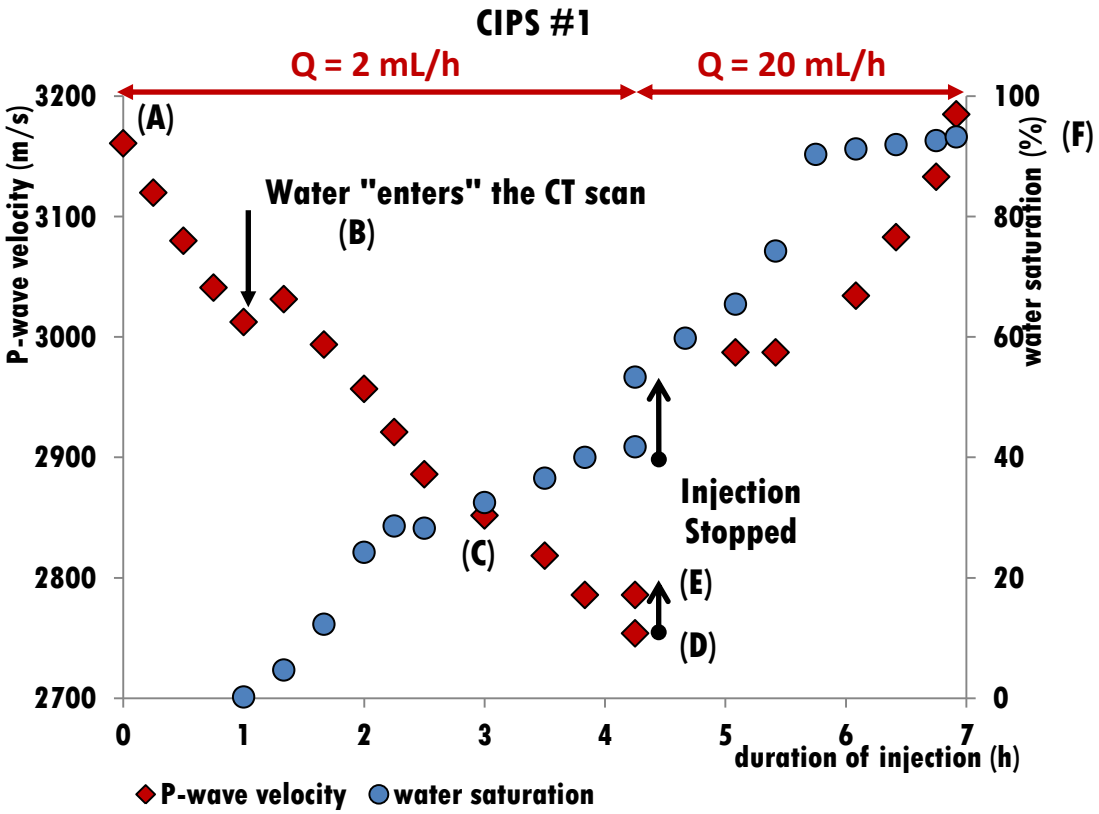

Figure 44 P-wave velocity and water saturation with duration of injection, with confining pressure at 5 MPa, for CIPS #1. Injection started at 2 mL/h, it was stopped for 17 hours and restarted at the rate of 20 mL/h. (A) to (F) are the moments depicted in Figure 43.

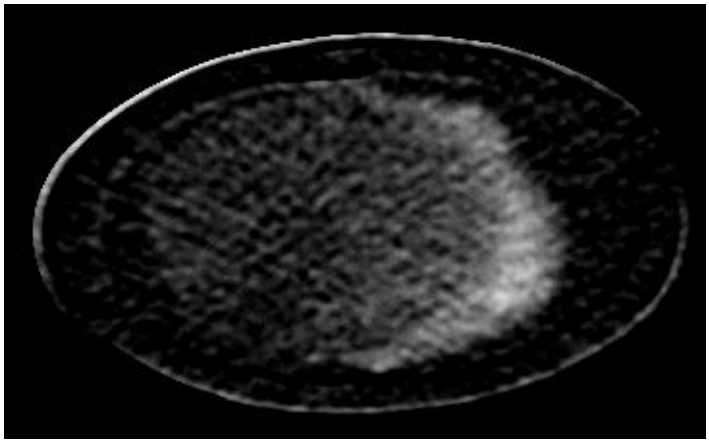

Figure 45 Difference between the CT scan (C) and (B) of Figure 43. The white lunar-shape on the right side represents the volume of water that entered the sample between those moments.

5.2 CIPS #2

Figure 46 shows the evolution of the P-wave velocity (V_P) and water saturation (S_W) with duration of injection for Phase 1 (water injection in a dry sample). The initial injection rate was 3 mL/h and at the confining pressure was set to 5 MPa. The moment the saturation front reached the ultrasonic monitored position is the moment when V_P started decreasing at 1h30. The decrease is continuous, at the rate of 15 m/s/h. The forced saturation happened at 7h30min, at the high injection rate of 60 mL/h and at the confining and pore pressure of 8 and 3 MPa, respectively. V_P and S_W responded to the forced saturation by increasing suddenly, by 80 m/s and 43%, respectively.

V_P decreased with the increase of the volume of fluid injected (saturation) for both water and oil injection. However for the water injection, V_P decreased only 60 m/s in 4 hours for CIPS #2 while for the same period of time, it decreased 400 m/s for CIPS #1. It is an interesting result since both synthetic sandstones have similar porosity and permeability and the same V_P when the samples were dry. This seems to be connected to the different amount of water imbibed during the same period of time by each sample: $S_W = 42\%$ for CIPS #1 and $S_W = 29\%$ for CIPS #2. The GW theory establishes that high P-wave velocities are associated to high water saturations because of the increase of the effective fluid bulk modulus.

Figure 47 shows a sequence of CT scans for Phase 2 (oil injection in a dry sample). The saturation front advanced from left to right until the sample was fully oil-saturated (Figure 46-E). This portrays the same fluid displacement and advancement of the saturation front of the water injection (data not shown). The lighter areas depict the presence of oil (by increasing the CT number of each voxel). An initial tendency of the fluid to distribute on the lower part of the sample was spotted, likely influenced by gravity (in this case, perpendicular to the direction of injection). Through each CT scan, the displacement of the saturation front was matched to a specific evolution of V_P and oil saturation (S_O).

Figure 48 shows the evolution of V_P and S_O with duration of injection for Phase 2. The moments (A) to (E) of Figure 47 are highlighted:

(A) The V_P when the sample is dry, S_O = 0%, is 3377 m/s (Figure 47-A and 48-A).

(B) At approximately 1 hour after the beginning of the injection, there is a slight decrease of 12 m/s on V_P (Figure 48-B). This is due to the entrance of an oil that was left in the injecting tube from a previous experiment. This effect is felt for 1 hour, after which V_P is constant until the light-oil penetrates the monitored position.

(C) The penetration of the saturation front into the monitored position (at 3h30 min, Figure 47-C) is reflected by the sudden decrease of V_P with S_O = 22%. The initial imbibition of oil was slower when compared to water due to the initial penetration of the heavy-oil that delayed the entrance of the light-oil. However, after the oil front penetrated the monitored position, S_O increased at the rate of 13% per hour, faster than the evolution of S_W (8% per hour). The faster local imbibition of oil in Phase 2 when compared to water in Phase 1 expresses the effect of the oil's higher wettability (Morrow & Mason 2001) when compared to water. Oil is more likely to remain inside the pore network than water that easily flows away through connected pores (this is a high permeable sample, K_1 = 10 D). This is also reflected in the higher oil saturation (S_O = 78%) reached during the same period of time, 8 hours (S_W = 57%).

(D) At approximately 7 hours of injection, V_P and S_O seemed to have reached a plateau at $V_P = 3257$ m/s and $S_O = 74\%$. When the oil injection was stopped for 12 hours, S_O and V_P changed very little. This is because without the external pressure applied (due to the injection rate), the oil offers greater resistance to move (due to its viscosity) and is reflected by the no change in those two parameters.

(E) The forced saturation happened at the injection rate of 60 mL/h and at the confining and pore pressures of 8 and 3 MPa, respectively. At the end of the forced saturation (Figure 48-E), V_P increased 100 m/s and S_O increased 22%.

Figure 48 also shows the P-wave velocity dependence with confining pressure, $V_p(p_c)$ for dry and oil-saturated sample. For both, $V_p(p_c)$ is clearly linear. The increase in p_c closes open pores and/or fractures. This may lead to the expulsion or compression of fluids increasing the rock's bulk modulus and, according to the GW theory, V_P increases. The V_P at 5 MPa is close for both dry and 100% saturated but

the increase is more pronounced for the dry sample (66 m/s) than for when the sample is oil-saturated (48 m/s). This is because air is much more compressible than oil, offering virtually no resistance to the increase in p_c. The effect of the presence of water (fluid effect) creates higher variations in V_P.

Figures 49 and 50 show the P-waveforms recorded at several stages of the imbibition of Phase 1 (water injection) and 2 (oil injection). The entrance of water in the dry sample caused a slight increase in the P-wave arrival time and decrease in wave-amplitude. However, at the end of the injection at 3 mL/h, the wave-amplitude had decreased significantly. The forced saturation caused an increase in wave-amplitude and in V_P comparable to the values obtained when the sample was dry. The entrance of oil in the sample hardly changed the P-wave amplitude but there was a slow, steady decrease. Upon the start of the forced saturation and after stopping injection for 12 hours, there was no visible change in wave-amplitude but the P-wave arrival time had decreased (increase in V_P).

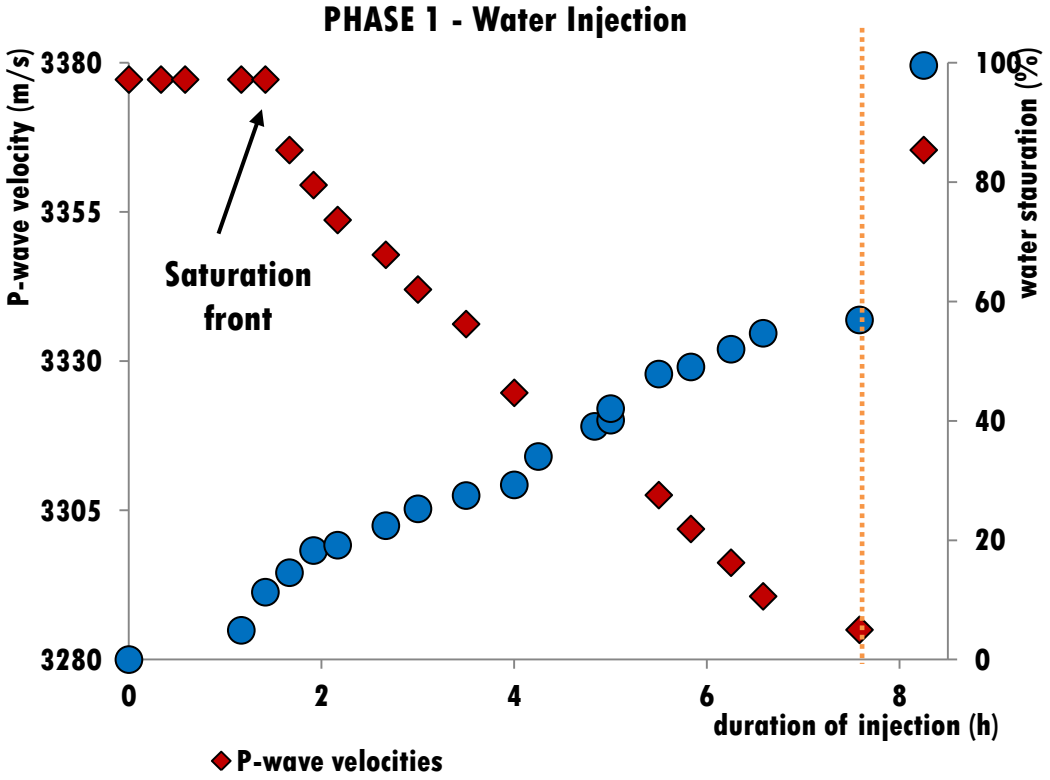

Figure 46 P-wave velocity and water saturation with duration of injection at the rate of 3 mL/h for Phase 1 (water injection in a dry sample) for CIPS #2. Orange line represent the moment when the forced saturation was started (injection rate: 60 mL/h, confining pressure: 8 MPa, pore pressure: 3 MPa).

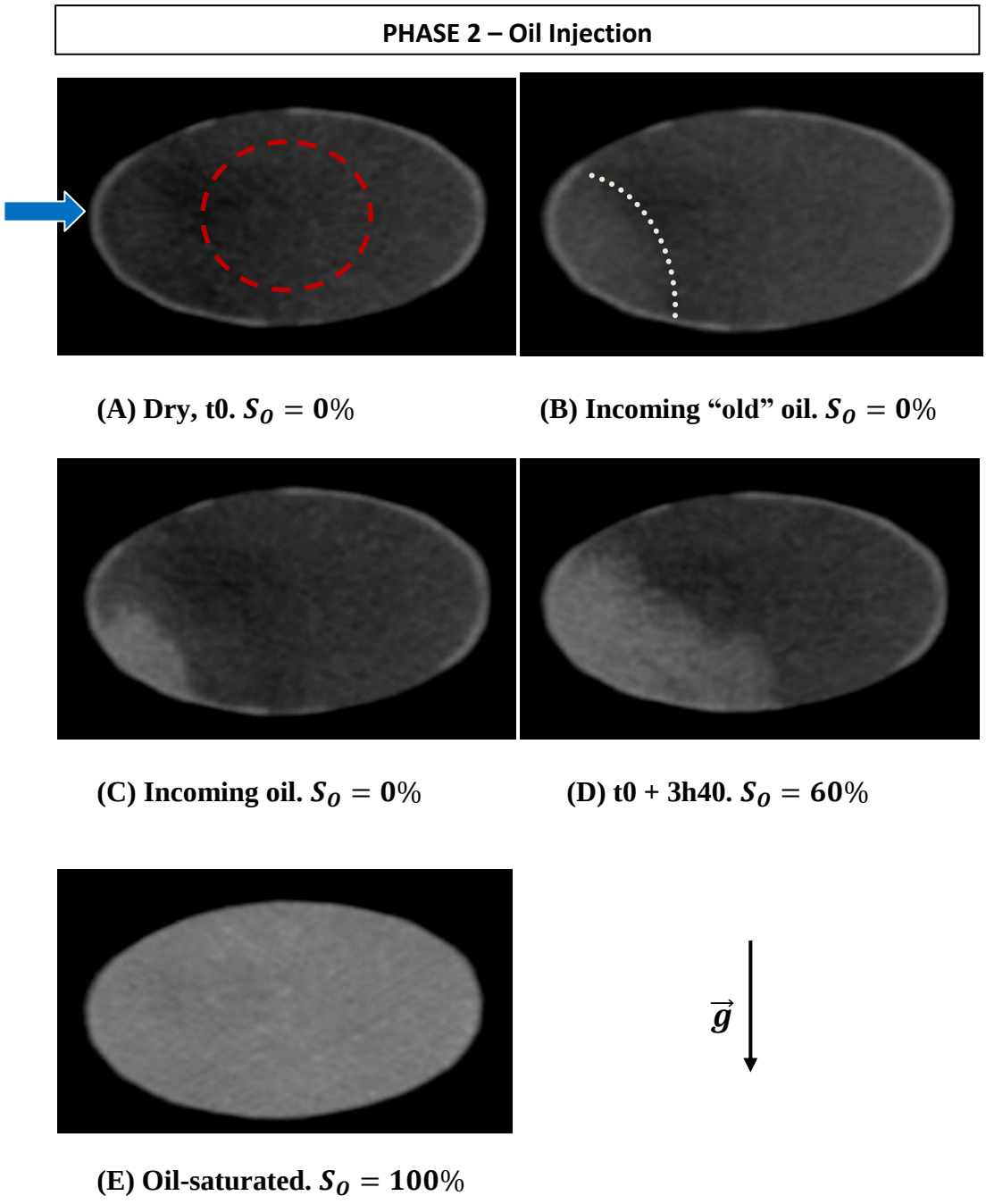

Figure 47 CT scans from dry **(A)** to oil-saturated **(E)** (Phase 2). The saturation front moves from left to right (in the direction of the injection, blue arrow). There is an initial tendency of the fluid to distribute on the lower part of the sample, mostly influenced by gravity ($\vec{g}$) (perpendicular to injection rate). Red circle represent the area where the local saturation was estimated. Oil saturation (S_O) also shown for each moment. Note the "old" oil that enters prior to the light-oil in (B) (limited by white dashed line).

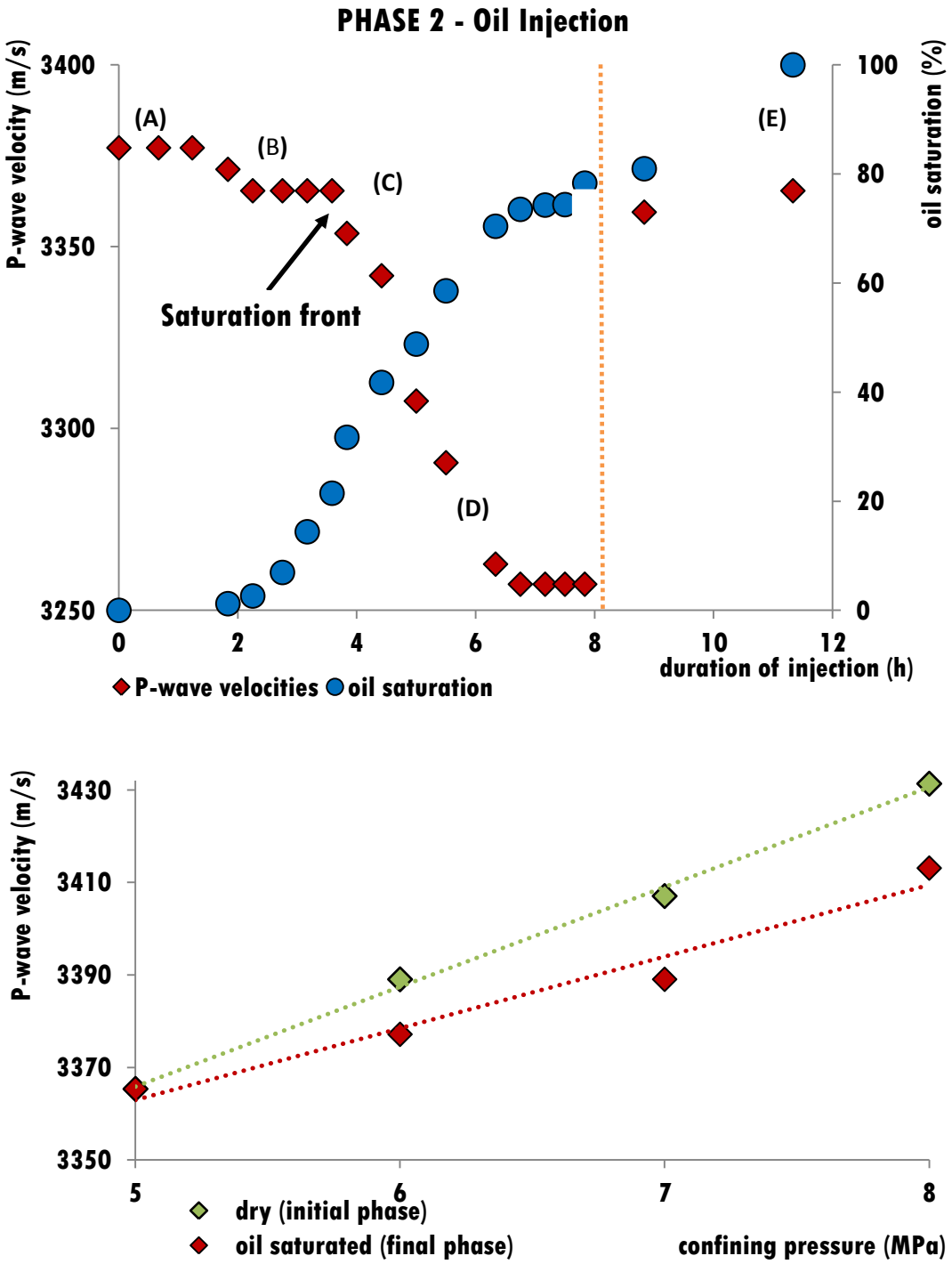

Figure 48 (**Top**) P-wave velocity and oil saturation with duration of injection (injection rate: 3 mL/h, confining pressure: 5 MPa). Orange line is the moment when the injection was stopped and the forced saturation was initiated (injection rate: 60 mL/h, confining pressure: 8 MPa, pore pressure 3 MPa). (A) to (E) are the moments depicted in Figure 47. **(Bottom)** P-wave velocity dependence with confining pressure (pore pressure: 3 MPa) at the beginning and end of the oil injection.

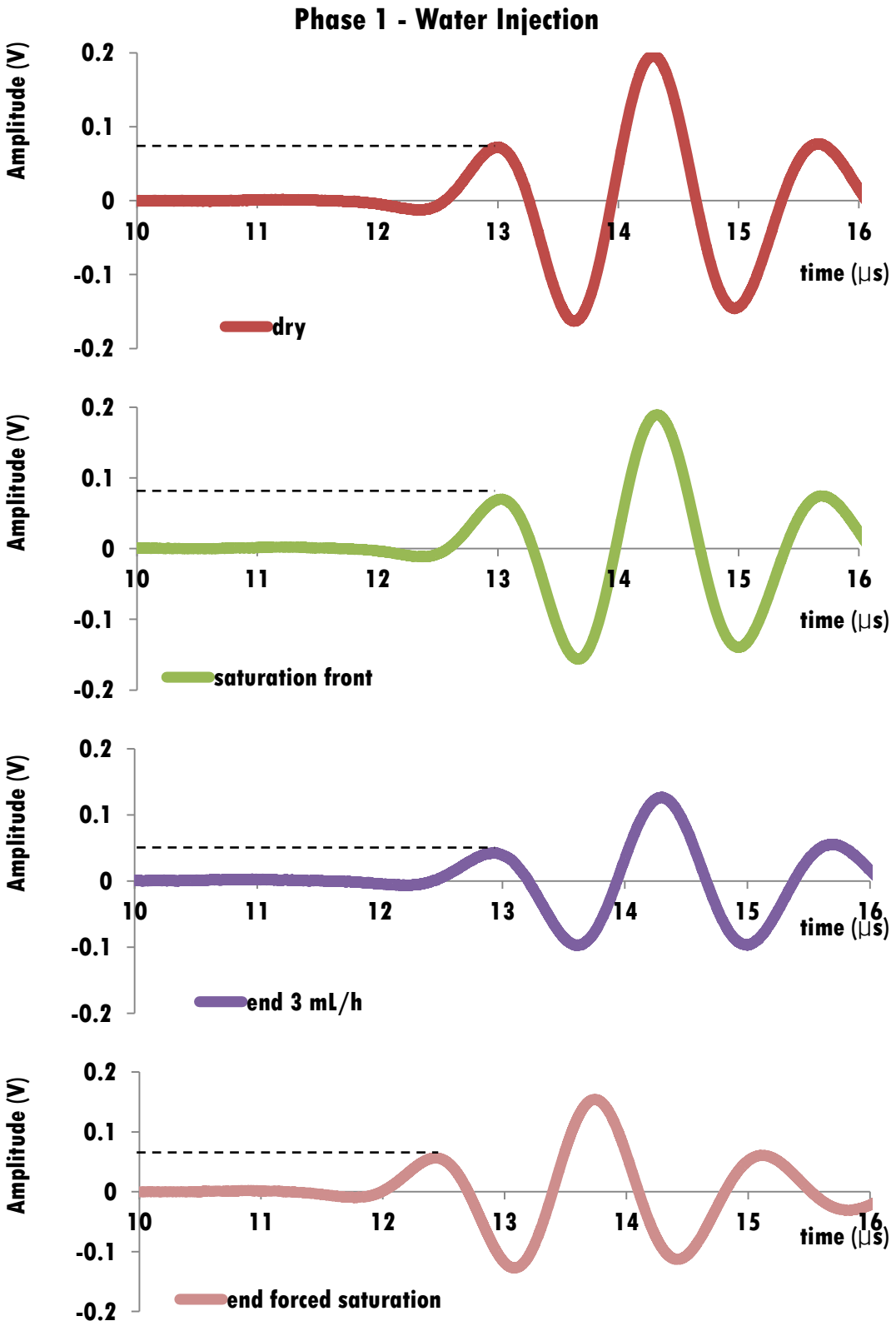

Figure 49 P-waves for Phase 1 (water injection) at several stages of the imbibition. The wave amplitude decreased from "dry" to "end 3 mL/h" and increased at the "end of forced saturation".

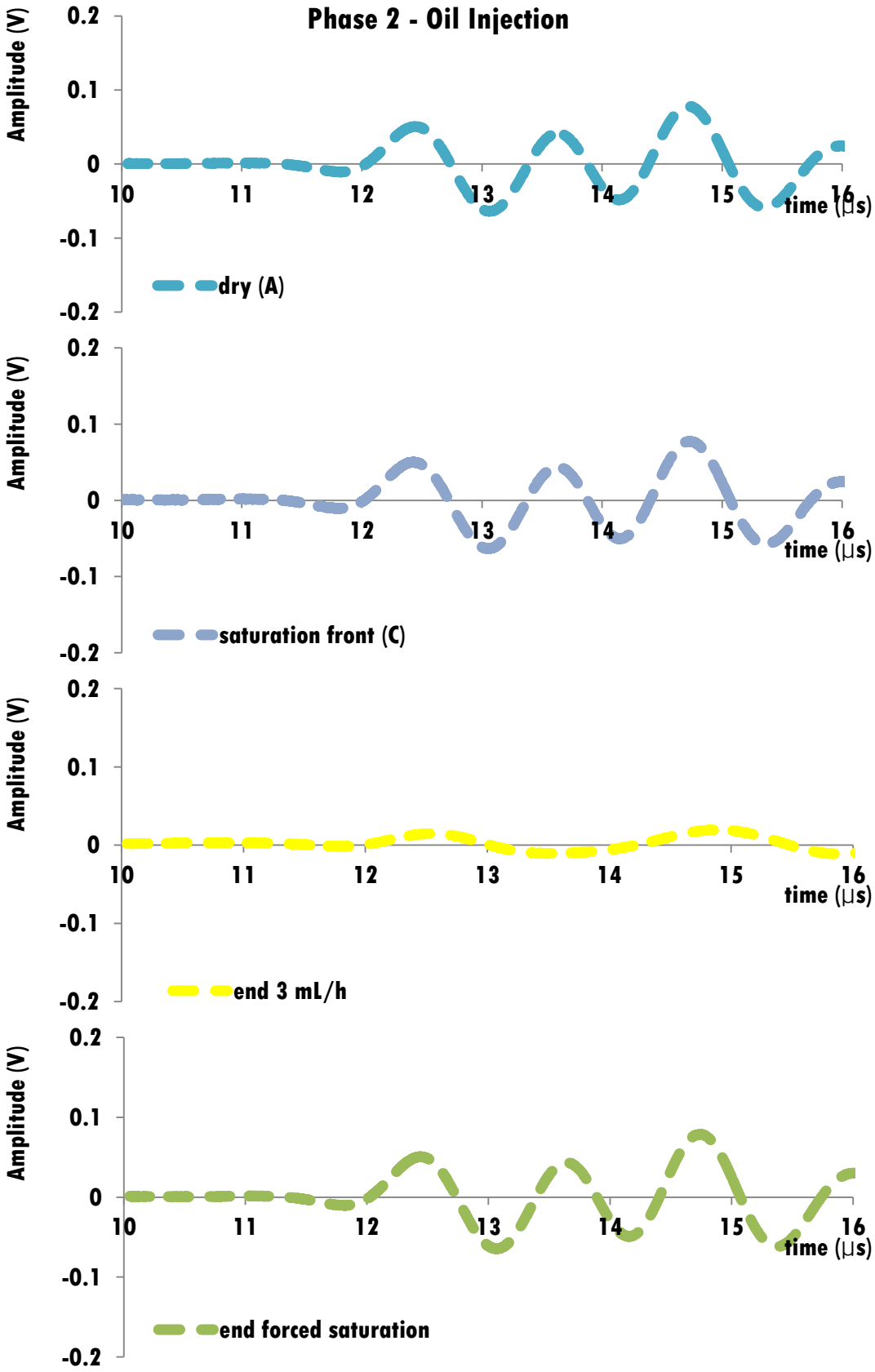

Figure 50 P-waves for Phase 2 (oil injection) at several stages of the imbibition. "Dry" and "saturation front" waves are almost the same. The wave amplitude increases at the "end of forced saturation". The same vertical scale as Figure 49 is displayed for comparison.

CHAPTER 6
CARBONATES

Carbonate samples were used to investigate the distribution of fluids in highly heterogeneous rocks with low-permeability. Brine was injected (60 g/L of KCl mixed in distilled water) to enhance contrast between matrix and fluids in the CT scan. First, the injection started at the rate of 3 mL/h, confining pressure of 5 MPa and no pore pressure (the outlet was open). When the water exited the sample, the forced saturation commenced. The injection rate was increased up to 60 mL/h, and the confining and pore pressures were set to 8 and 3 MPa, respectively (resulting in an effective pressure of 5 MPa). The P-wave velocity dependence with confining pressure was recorded when the samples were dry and fully-saturated.

Table 6 shows the P- and S-wave velocities (V_P and V_S, respectively) for the carbonate samples in the axial and radial directions. These velocities were measured when the samples were dry, prior to any fluid flow experiment. The ratio $\left(\frac{V_{P,radial}}{V_{P,axial}}\right)$ gives an idea of the level of the ultrasonically acoustic anisotropy of each sample. CB #2 is very anisotropic $\left(\frac{V_{P,radial}}{V_{P,axial}} \sim 1.2\right)$. Interestingly, CB #1 and CB #3 have V_P in the radial direction smaller than in the axial direction. This might indicate preferential bedding in the axial direction that aids the faster propagation of P-waves. The first CT scans taken of these samples displays well their level of heterogeneity.

CB	V_P radial (m/s)	V_S radial (m/s)	V_P axial (m/s)	V_S axial (m/s)
CB #1	1924.24	n/a	2042.86	1172.13
CB #2	2010.58	1402.21	1681.01	n/a
CB #3	1421.64	865.91	1438.98	895.83

Table 6 P- and S-wave velocities (V_P and V_S, respectively) for the radial and axial directions of the cylindrical carbonate samples.

6.1 CB #1

Figure 51 shows the evolution of V_P and S_W with duration of injection for CB #1. The initial injection was at the rate of 2 mL/h and at the confining pressure of 5 MPa. The forced saturation happened at 22 hours, at the injection rate of 60 mL/h and confining and pore pressures of 8 and 3 MPa, respectively.

During the fluid flow experiment the pressure cell tipped slightly (less than 0.5 cm) and was only repositioned before the forced saturation. This resulted in different scanned areas between CT scans (A)-(D)-(E) and CT scans (B)-(C) (see Figure 52). This means that the evolution of S_W in Figure 51 and the CT numbers in Figure 53 are not of the same scanning area. However, this does not influence the purpose of this study: 1) match the advancement of the saturation front to a specific trend in V_P; 2) characterize the fluid distribution inside the sample. (Note that because the transducers were glued to the surface of the cell, the acoustic monitored path did remain the same throughout the experiment.)

There was a decrease of V_P when the saturation front entered the monitored position. Though this decrease is small it is still noticeable. The small variation of V_P with the presence of water is an expected feature since carbonates are generally not acoustically fluid-sensitive rocks. S_W increased 27% in the same period of time. At approximately 22 hours (the end of the initial injection), S_W increased only 2% while V_P increased 36 m/s. Upon the forced saturation, V_P and S_W increased considerably: 177 m/s and 70%, respectively. S_W soon stabilized at 100% while V_P still increased 77 m/s in the next 3 hours, ending at 2190 m/s. The increase of V_P and S_W with the forced saturation was also observed in CIPS #1.

Figure 51 also shows the $V_p(p_c)$ when the sample is 100% water-saturated. The dependence is clearly linear, with a strong increase of 118 m/s in V_P for a variation of 5 MPa in confining pressure. CB #1 is then a pressure sensitive rock. As explained for the CIPS #2, the increase in confining pressure promotes the closure of open pores and/or fractures. As a consequence, water may be expelled or compressed, increasing the rock's bulk modulus V_P (GW theory).

The evolution of S_W matched well with the displacement of the injected water (Figure 52). Water entered the CT scan approximately 3 hours after the beginning

of the injection (Figure 52-B) and S_W increased fast, 21% in two hours. Two hours later, the increase of S_W slowed down and it did not change significantly for the next 14 hours (Figure 52-D). As seen for the synthetic sandstones, upon the forced saturation, S_W increased fast and full-water saturation was reached.

Figure 53 shows the variation of CT numbers (ΔCT) along the length of the CT scan (blue line in top figure). There was a small ΔCT between "dry" (moment A in Figure 51) and "beginning of the forced saturation" (Figure 51-E) of ~130 on the left side of the CT scan which corresponds to $\Delta S_W = 30\%$. From that moment on, CT increased quite evenly throughout the sample's length, reaching at the end of the experiment (end of the forced saturation), $\overline{CT}_E = 2300$ which corresponds to an increase of 300 from $\overline{CT}_A = 2000$.

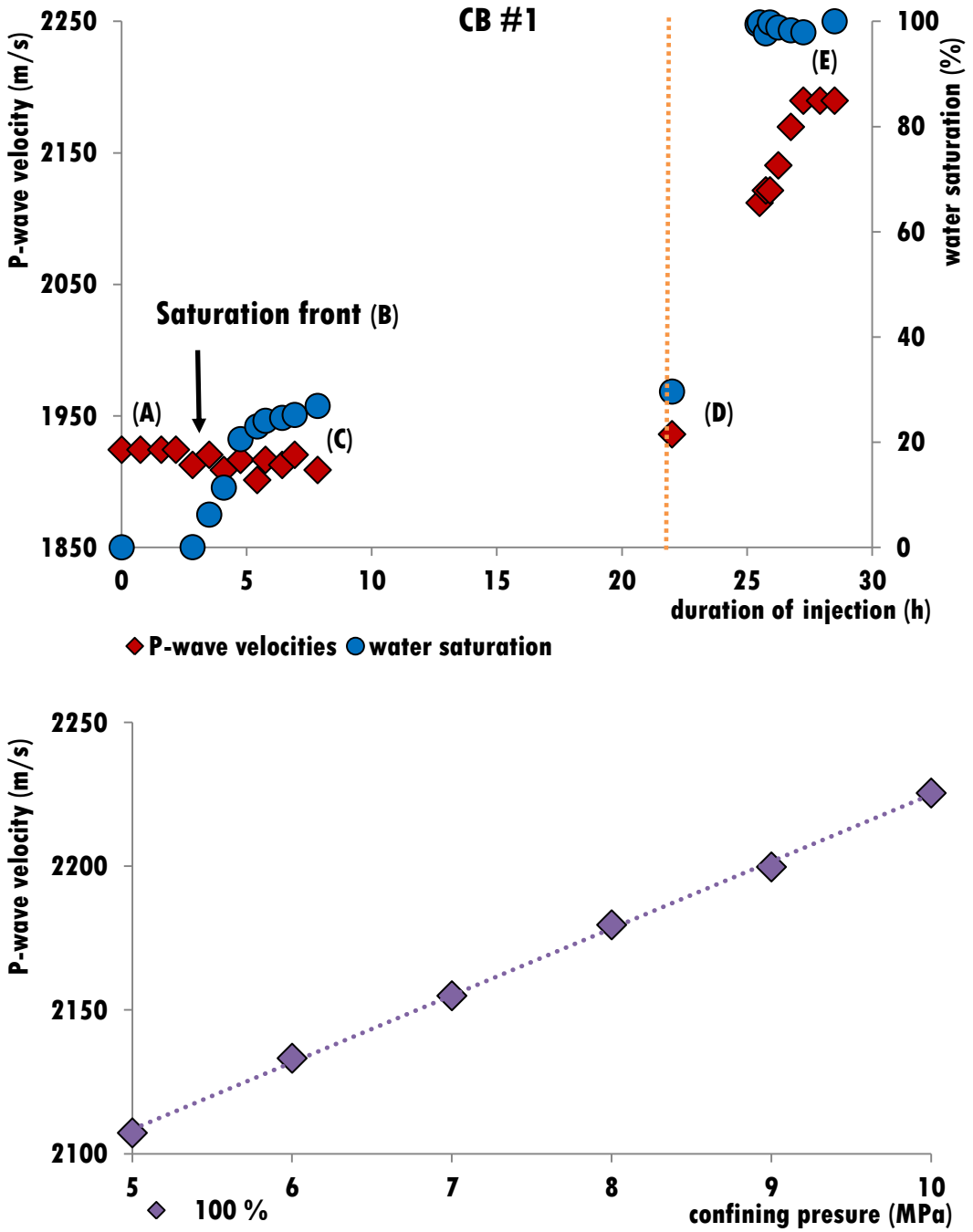

Figure 51 (Top) P-wave velocity (V_P) and water saturation (S_W) with duration of injection for CB #1. Initial injection rate: 3 mL/h, confining pressure: 5 MPa. Orange line represent the moment the forced saturation was initiated (injection rate: 60 mL/h, confining pressure: 8 MPa, pore pressure: 3 MPa.). **(Bottom)** Evolution of V_P with confining pressure (pore pressure: 3 MPa) at S_W = 100%.

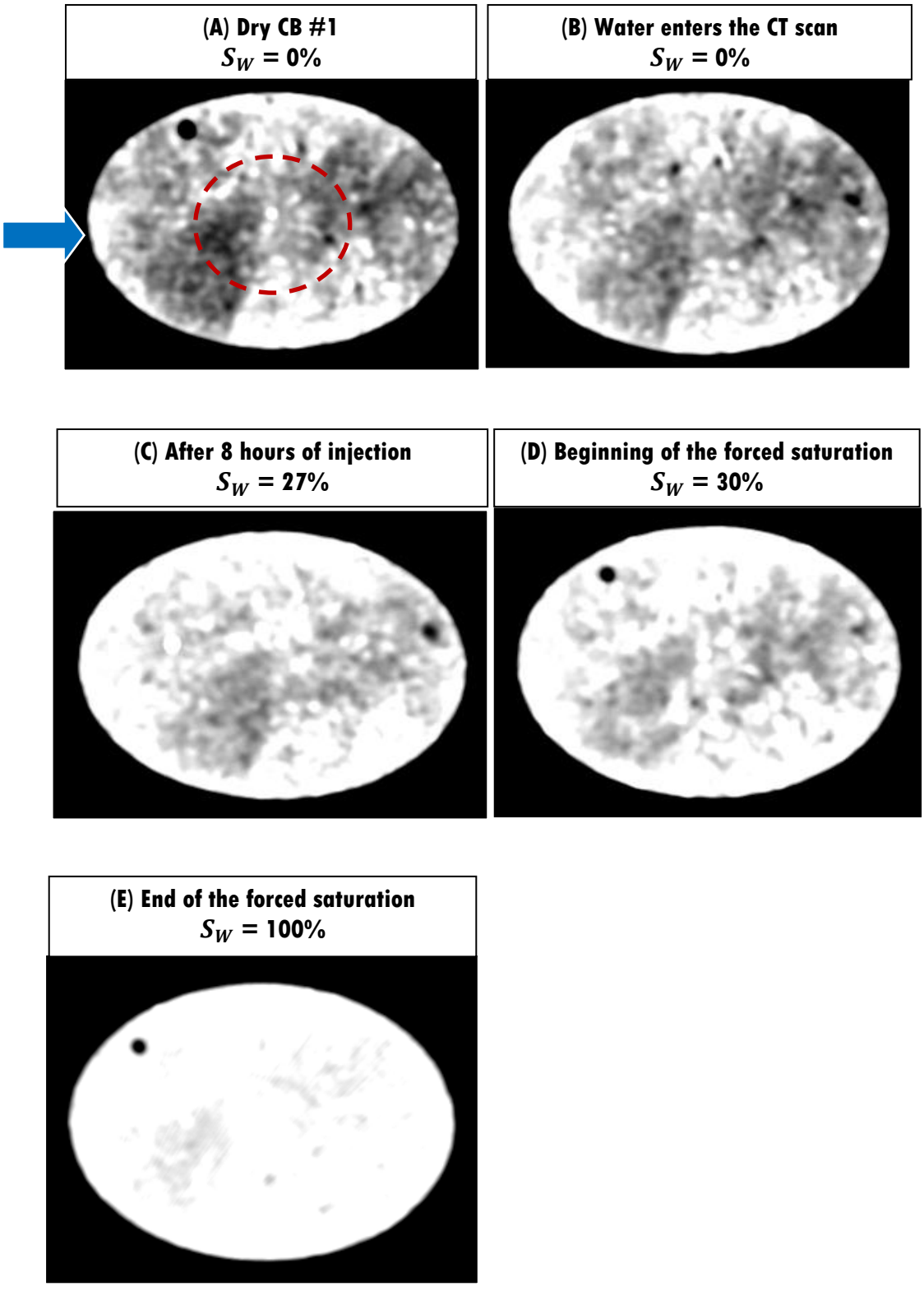

Figure 52 Sequence of CT scans of CB #1 from dry to water saturated (after the forced saturation). (A) to (E) are the moments depicted in Figure 51-Top. Water saturation (S_W) also shown for each moment. Red circle represents the ultrasonically monitored position. Blue arrow indicates the direction of injection.

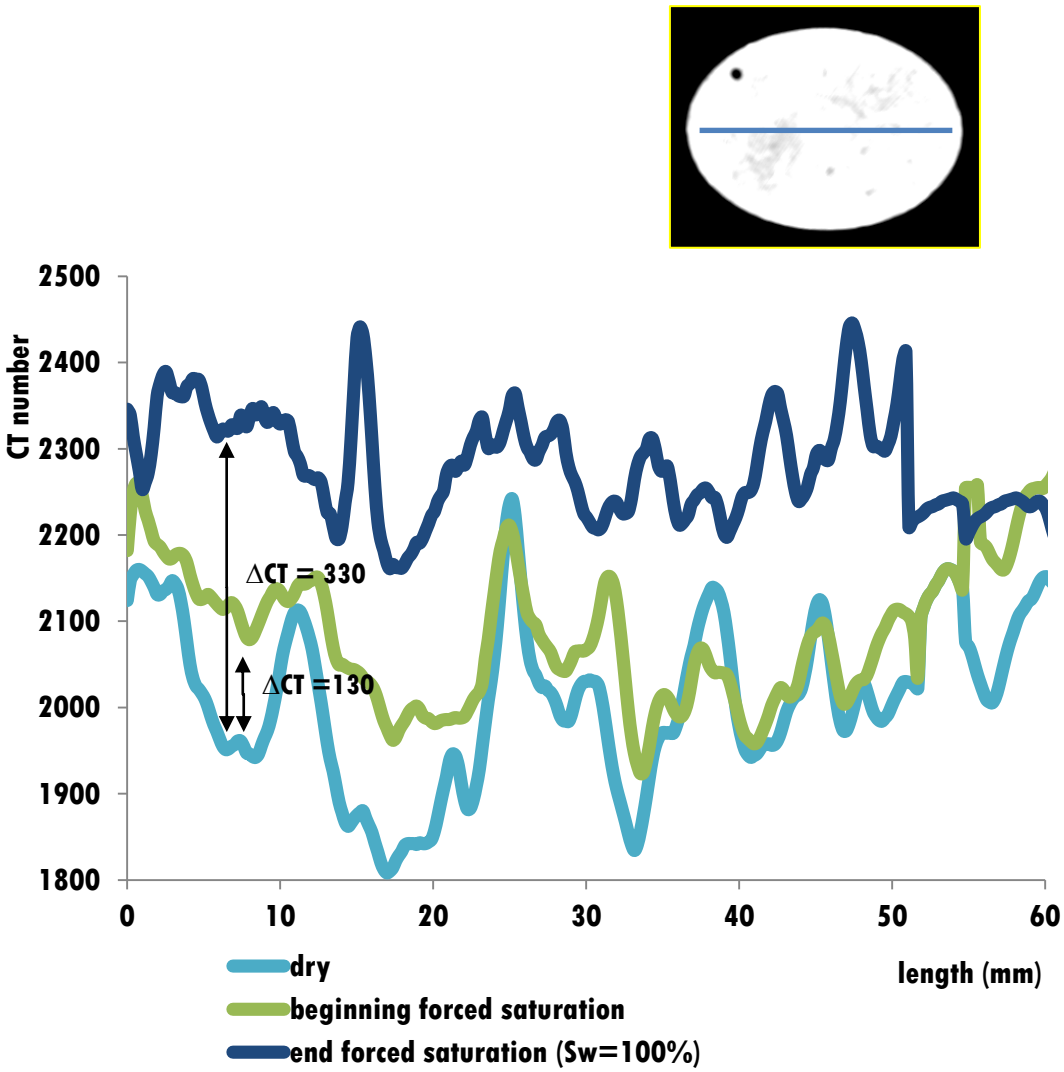

Figure 53 Variation of the CT number (ΔCT) along the length of the sample (blue line in top figure) when the sample is dry (Figure 52-A) and at the beginning ((Figure 52-D) and end ((Figure 52-E) of the forced saturation.

6.2 CB #2

Figure 54 shows the evolution of V_P and S_W for CB #2. The injection was performed at the rate of 3 mL/h and at the confining pressure of 5 MPa. It was a very low permeable rock, K_l = 4.6 mD, therefore it took a long time (over 24 hours) for the water to exit the sample. There was hardly any change in V_P and S_W in the first 10 hours of injection. Then, V_P started increasing and reached the final value of 2077 m/s at S_W = 38%. The forced saturation occurred at the injection rate of 60 mL/h and confining and pore pressures of 8 and 3 MPa, respectively. Upon the forced saturation, V_P increased 300 m/s. However, 100% water saturation was not reached. Figure 54 also shows $V_p(p_c)$. The dependence is linear for dry and at the end of the forced saturation. The is an increase of ~90 m/s in V_P when the confining pressure is increased from 4 to 9 MPa (at the pore pressure of 3 MPa). This change portrays an acoustically pressure-sensitive rock.

The small variation of V_P with the presence of water is an expected feature as discussed in CB #1. However, the small variation of V_P in such a long period of time, 22 hours, and at the (high) injection rate of 3 mL/h, is surprising. Though, an explanation was retrieved when the CT scans in Figure 55 were analysed in more detail. From the beginning to the end of the injection at the rate of 3 mL/h, there was no change in the coloured gradient of the CT scan, denoting no intrusion of water. Only upon the forced saturation, changes in the "whiteness" of the scan were observed, i.e. water was visible in the CT scan. Water must have travelled close to the walls of the sample and started moving in the direction of the centre, accumulating preferentially on the left side. Hence, it seems this is the most permeable and well-connected side of the sample. At the end of the forced saturation, a significant part of the sample is still unfilled with water: the left side of the CT scan is much more saturated than the right side. The evolution of S_W plotted in Figure 54-Top is affected by this "duality". Actually, if the sample is divided through the middle of the ellipse and is assumed that the left side is fully saturated (100%), the maximum S_W reached for the right side is 52%.

Figure 56 shows the variation of CT numbers (ΔCT) along the length of the CT scan (blue line in top figure). It is confirmed quantitatively what was observed in

Figure 55: a much higher variation of CT numbers on the left side of the scan between dry sample and end of the experiment (end of forced saturation), $\Delta CT = 260$, than the right side (maximum $\Delta CT = 100$). This also shows that most of the water accumulated on the left side of the sample during the forced saturation. Also to note that there was not a significant change in ΔCT on the right side between the beginning and end of the forced saturation.

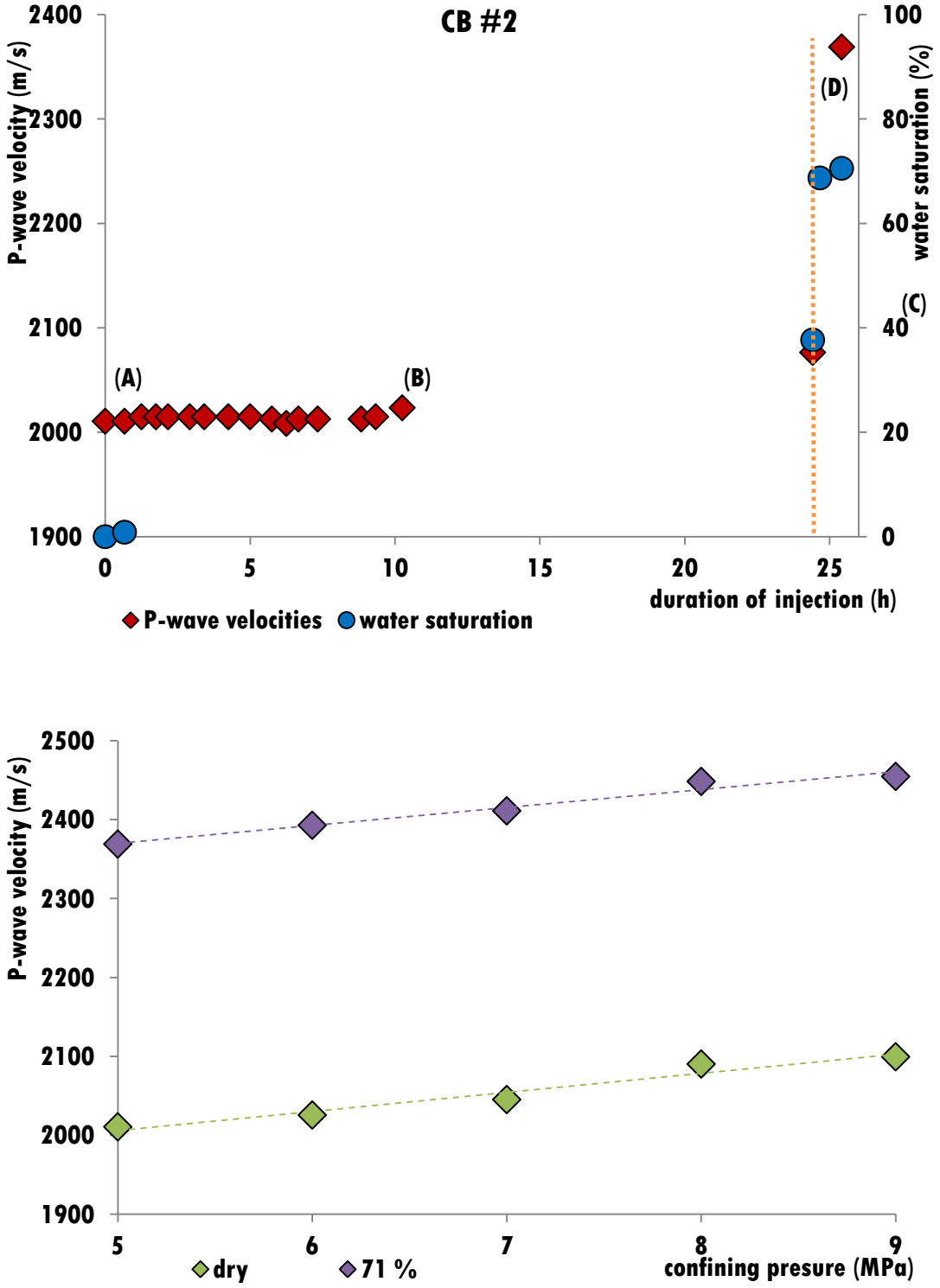

Figure 54 (Top) P-wave velocity (V_P) and water saturation (S_W) with duration of injection for CB #2 (injection rate: 3 mL/h, confining pressure: 5 MPa). Orange line represent the moment when the forced saturation was initiated (injection rate: 60 mL/h, confining pressure: 8 MPa, pore pressure: 3 MPa). **(Bottom)** Evolution of V_P with confining pressure for dry and S_W = 71%.

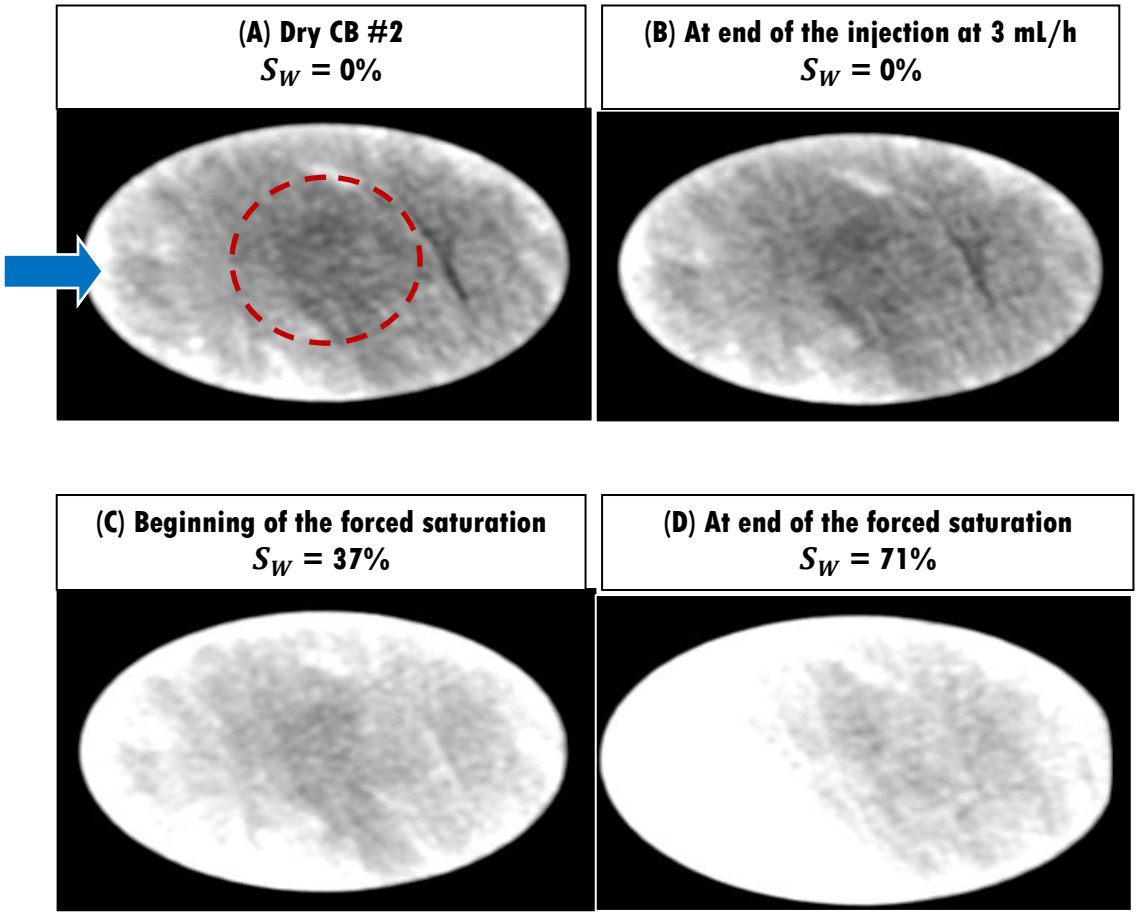

Figure 55 CT scans of CB #2 from the beginning of the experiment to the end of the forced saturation. (A) to (D) are the moments marked in Figure 54-Top. Note that at the end of the forced saturation, the left side is much more saturated (whiter) than the left side (darker). Water saturation (S_W) also shown for each moment. Red circle represents the ultrasonically monitored position. Blue arrow indicates the direction of injection.

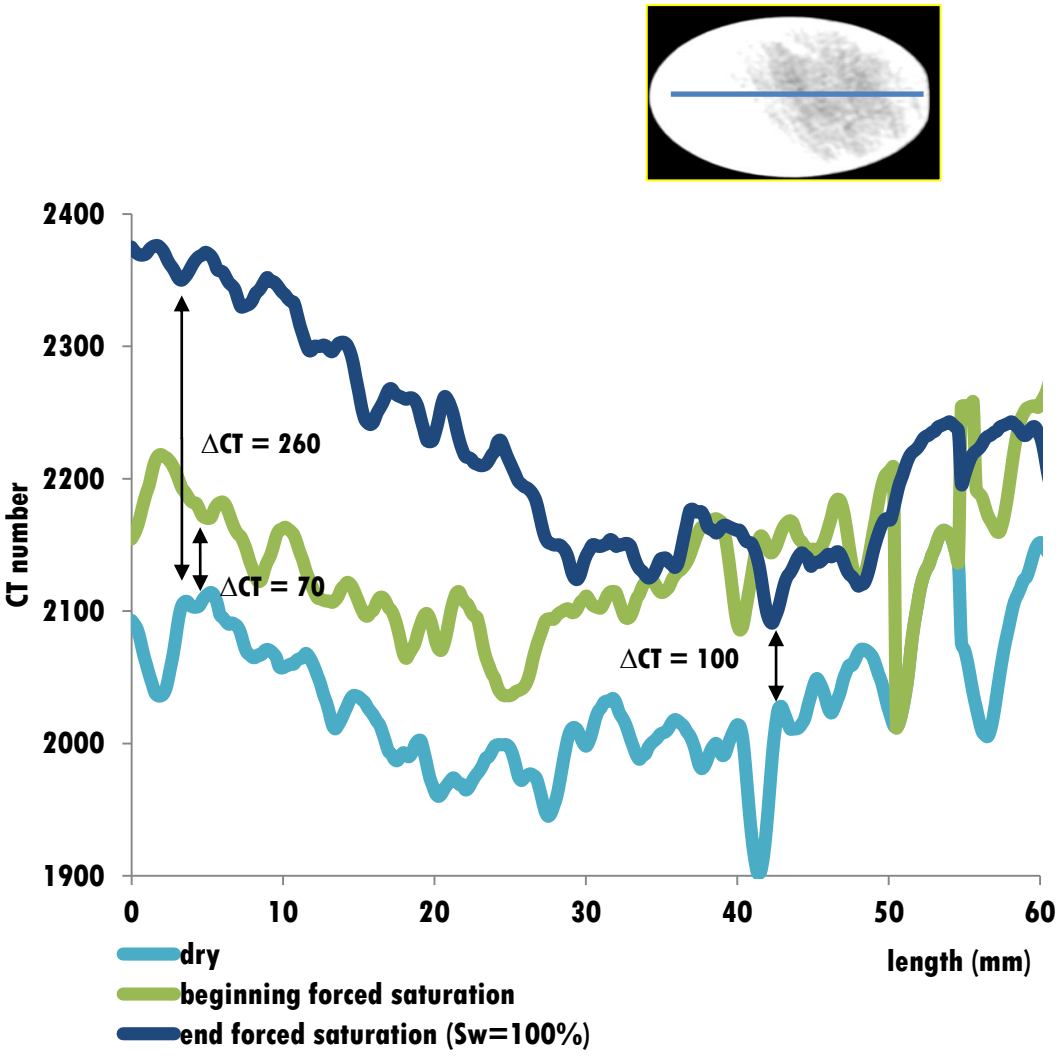

Figure 56 Variation of the CT number (ΔCT) along the length of the sample (blue line in top figure) when the sample is dry and at the beginning and end of the forced saturation. Note the very small ΔCT between the beginning and end of the experiment on the right side when compared to the left side (100 vs. 260, respectively).

6.3 CB #3

Figure 57 shows the evolution of V_P and S_W for CB #3. The injection was performed at the rate of 3 mL/h and at the confining pressure of 5 MPa. The V_P when is the sample is dry is the lowest from all the carbonate samples, $V_P = 1418\, m/s$. Also, the difference between V_P when the sample is dry and water-saturated is the smallest: 78 m/s. At 45 minutes, V_P started decreasing with increasing S_W. The V_P response to the presence of water is very discreet, in 6 hours it only decreases 11 m/s corresponding to an increase of $S_W = 25\%$. Upon the forced saturation (injection rate of 60 mL/h and confining and pore pressures of 8 and 3 MPa, respectively), the response of V_P and S_W was immediate, as observed on the other carbonates. Both V_P and S_W increased significantly after 45 minutes: by 89 m/s and 75%, respectively.

The acoustic response matches well with the specific fluid distribution seen in Figure 58. There is not a clear difference between Figure 58-A and Figure 58-B. There is a small concentration of water on the left side of the CT scan, outside the red circle and therefore does not affect the estimated S_W (recall that S_W is estimated over the red circle in Figure 58-A). However there is a change in V_P. Figure 56-B and 56-C shows that the water distributed preferentially on the periphery of the sample, going from the walls to the centre of the sample. This tendency to propagate through the walls may have brought enough water to the ultrasonically monitored path to influence the P-wave propagation and decrease V_P though it is not visible in our plan of CT scanning.

Figure 57 also shows $V_P(p_c)$. For dry and $S_W = 25\%$, $V_P(p_c)$ is similar up to 6 MPa. There is a "jump" for the dry sample after 6 MPa and for $S_W = 25\%$ after 7 MPa. These "discontinuities" reinforce the initial supposition that this sample has significant structural damage (a large void, either a fracture or a large pore) as indicated by the very low V_P (Table 6) and high anisotropy: $\frac{V_P}{V_S} \sim 1.6$ (for both axial and radial direction). As the sample is compressed, the fracture can close (or the pore collapses) and the increasing local density promotes an increasing in V_P (Müller, Gurevich & Lebedev 2010). When $S_W = 100\%$, the water fills the void entirely and works as a structural bond (Carles & Lapointe 2005). Hence, the matrix

and pore fluid compress in phase ("synchronized") and $V_P(p_c)$ is linear. The reason why at $S_W = 25\%$ the "jump" occurs at a higher pressure when compared to the dry sample is due to the presence of water. The water offers more resistance to the compression than air, delaying the closure of the void. Unfortunately, these structural changes are not visible in the CT scans due to their low resolution. However, CB #3 had the lowest average CT number of all dry carbonates (estimated over the whole sample), $\overline{CT} = 1800$ ($\overline{CT} = 2000$ for CB #1 and CB #2). Low CT numbers are associated to low density matrices (see Equation 8). On the other hand, low dense carbonates (more porous) often generate low V_P (Eberli et al. 2003), which is the case of this sample.

Figure 59 shows the P-waves for when CB #3 is dry and $S_W = 40\%$ and 100%. The decrease with the presence of water is striking. The wave-amplitude decays by more than half within only 40% of S_W. Upon the forced saturation, the wave-amplitude increases significantly. This behaviour is the same for the other carbonates of Part II (data not shown) and for the samples investigated in Part I (sandstones and limestone). Wave attenuation may be induced by trapped fluids and residual saturation in the porous media that causes a local discontinuous phase (Rubino & Holliger 2012; Steeb et al. 2013). The sudden increase in volume of water (or in fluid saturation) upon the "forced saturation" stage leads to a homogenization of the system, i.e. a one fluid phase in the porous media. The transition from partially saturated (two-fluid phase: pores filled with water and air) to fully saturated (one-fluid phase: pores totally filled with water) is the transition from a heterogeneous to homogenous media. As a consequence, the P-wave velocity increases considerably (as established by GW theory, Gassmann 1951).

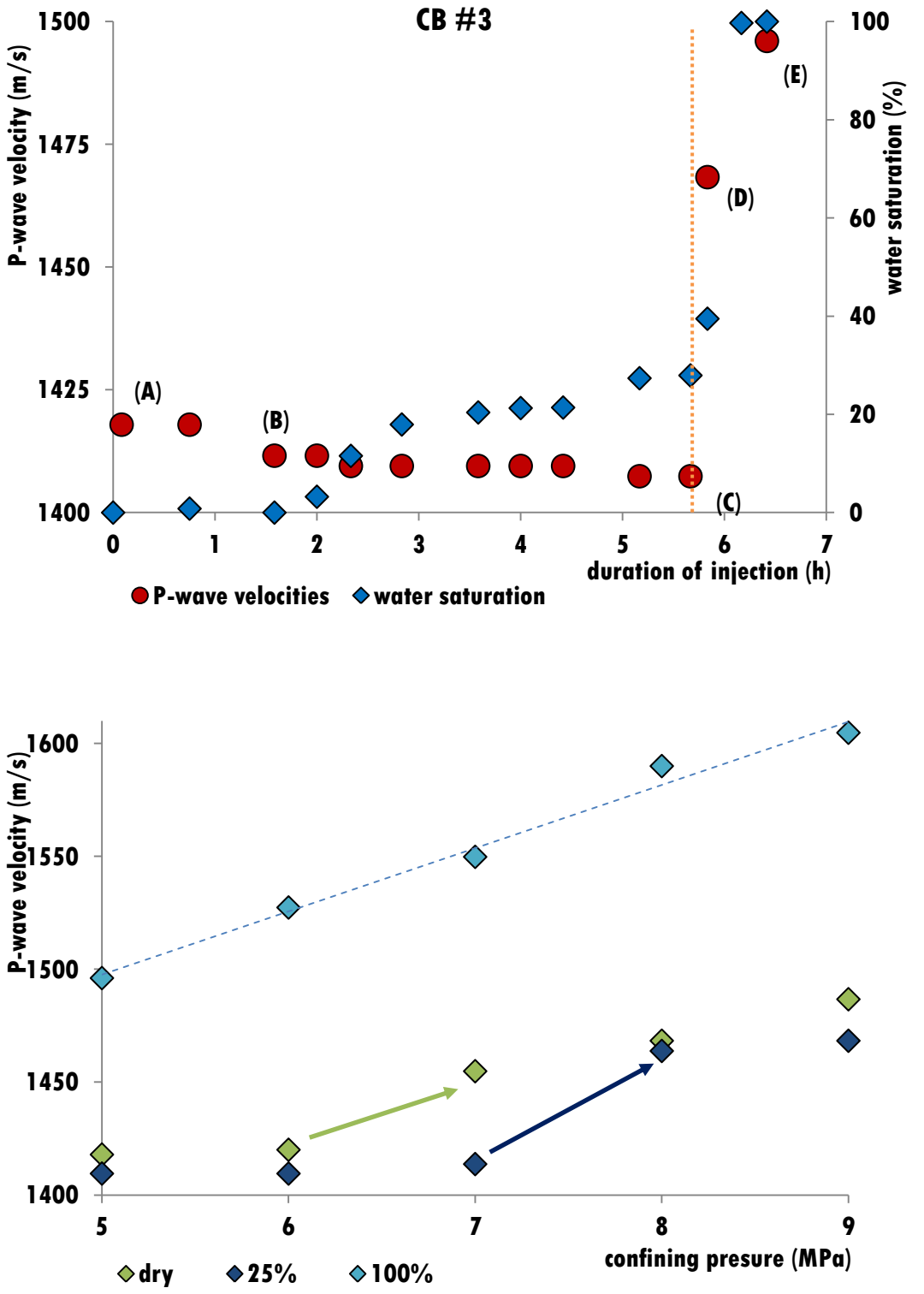

Figure 57 (Top) P-wave velocity (V_P) and water saturation (S_W) with duration of injection for CB #3 (injection rate: 3 mL/h, confining pressure: 5 MPa). Orange line represent the moment when the forced saturation was initiated (injection rate: 60 mL/h, confining pressure: 8 MPa, pore pressure: 3 MPa). **(Bottom)** Evolution of V_P with confining pressure for dry, $S_W = 25\%$ and 100%. Note the non-linearity when the sample is dry at 6 MPa and at $S_W = 25\%$ at 7 MPa coloured arrows).

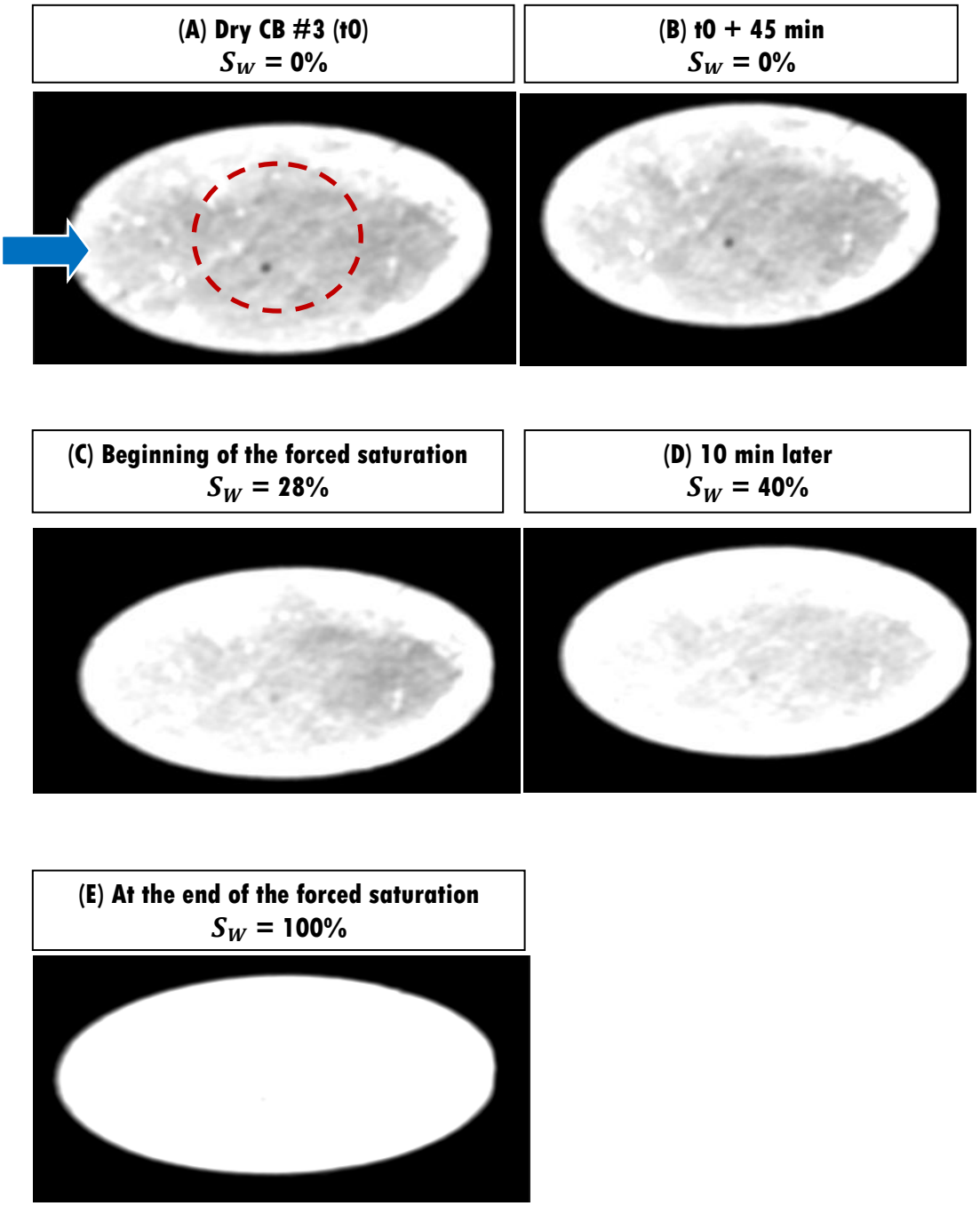

Figure 58 CT scans of CB #3 from the beginning of the experiment to the end of the forced saturation. (A) to (E) are the moments marked in Figure 57-Top. Water saturation (S_W) also denoted for each moment. Red circle represents the ultrasonically monitored position. Blue arrow indicates the direction of injection.

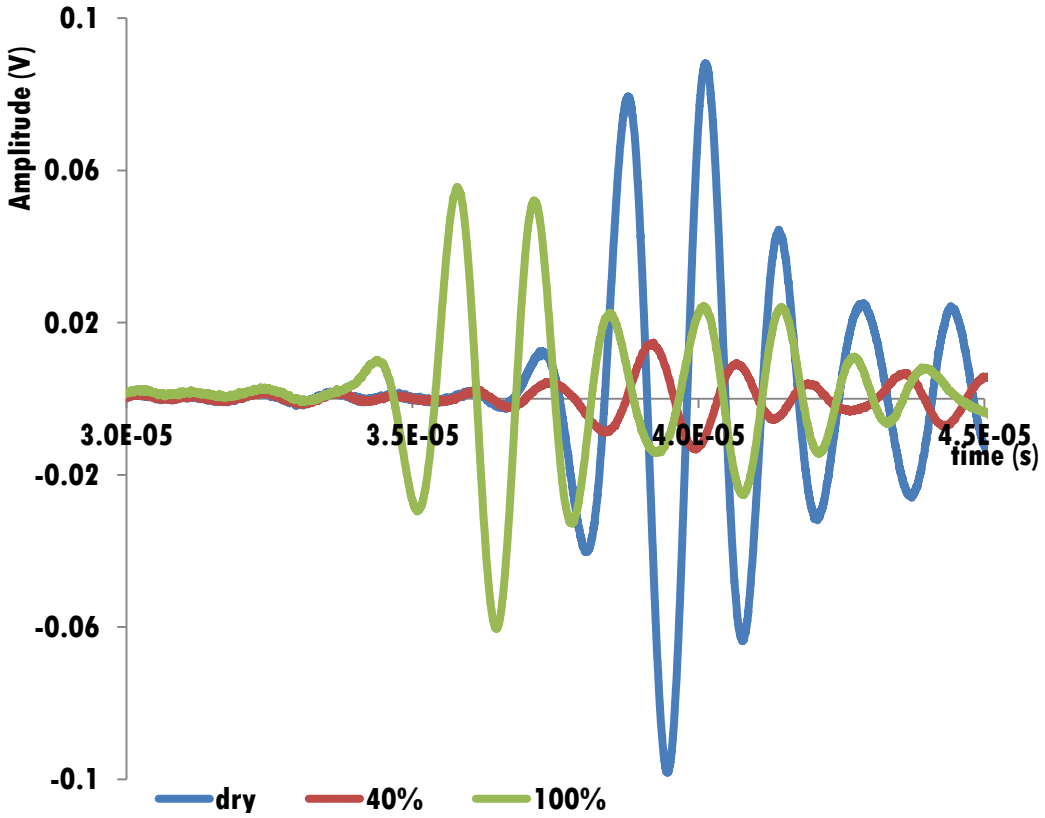

Figure 59 P-waves for dry, 40% and 100% water-saturated CB #3.

II.3 SUMMARY OF PART II

In Part II, acoustic-waves and fluid saturation were monitored simultaneously during the injection of water and oil in dry synthetic sandstones (Chapter 5) and "salty" water was injected in dry carbonates (Chapter 6) under confining pressure at constant injection rates. At the end of the imbibition, forced saturation was performed under confining and pore pressure at a high injection rate.

The intrusion of the injected fluid was identified through a notable change in the evolution of the P-wave velocity and water saturation. For all samples, the P-wave velocity decreased with increasing water and oil saturation.

The P-wave velocity dependence with confining pressure between dry and fully saturated phases evaluates how sensitive the rock is in the presence of fluids (Guéguen & Palciauskas 1994). The increase in confining pressure promotes the closure of open pores and/or fractures inside the sample. As a consequence, the fluids present in the pore network may be expelled or compressed, increasing the local rock's bulk modulus. According to the Gassmann-Wood theory, the P-wave velocity will increase. This effect was observed for all samples.

A decrease in P-wave amplitude as the fluids entered the ultrasonically monitored position (a two-fluid phase: pores filled with both air and water) followed by an increase as the sample head to full saturation (a one-fluid phase: pores filed with water) was consistently observed for all samples (including the ones from Part I).

The acoustic response to the presence of water between the two synthetic sandstones was different. In spite of having the same porosity and permeability (they were cored from the same block), the fluid distributed inside each sample was very different. For CIPS #1, the water displaced as a straight, piston-like displaced saturation front. For CIPS #2 there is no saturation front *per se* as the water appeared initially at the centre of the sample (of the CT scan). The water travelled through a preferential path outside the scanning plane, close to the walls of the sample. Therefore, for CIPS #2 the P-wave velocity decreased immediately (the water was in the ultrasonically monitored path) while for CIPS #1, the P-wave velocity started decreasing 1h30 after the beginning of the injection (after a period of no change). The other interesting difference was the range of the P-wave

velocity: CIPS #1 varied 100 m/s in 60% of water saturation while CIPS #2 varied 400 m/s in 40% of water saturation. This is indeed puzzling. However it might be connected to what was also found in Part I: more than the amount of water within a certain area, it is how the fluid is distributed that ultimately will affect the travelling P-wave (Cadoret, Mavko & Zinszner 1998). For example, 60% of water saturation represents 40% of air that might be present in the ultrasonically monitored position as few but large voids or a combination of several small ones.

The pattern of the acoustic response and fluid distribution between Phase 1 (water injection) and Phase 2 (oil injection) of CIPS #2 is very similar. This was not surprising as the oil had a density and bulk modulus close to water. A saturation front was well defined with the oil propagating as a piston-like displacement (from one base of the cylindrical sample to the other). Phase 2 generated a very low variation in the P-wave velocity, 120 m/s in 8 hours of injection. Since the same low range of P-wave velocity was observed for water injection (Phase 1), it is clear that this common behaviour is connected to the sample's microstructure. Unfortunately, the low resolution of the CT scans did not allow a further investigation of the particular aspect of the sample's microstructure that influenced the acoustic response.

The P-wave dependence with pressure was recorded when the samples were dry and fully-saturated. In this way, the P-wave velocity dependence with (1) pressure and (2) with the presence of fluids in the sample was studied. CIPS#2 was an important example of how the presence of fluid can be more phenomenological important that the effect of pressure on the acoustic response. As water was injected, the variation in P-wave velocity was much higher than due to the increase of confining pressure.

The acoustic properties of carbonates are less sensitive to the presence of fluids than sandstones. The carbonates produced higher variations in P-wave velocity due to the increase in confining pressure than due to the presence of fluids. The difference between the P-wave velocity when the sample is dry and the successive partially saturated phases was very small. However, though the difference in the P-wave arrival time was difficult to detect, the decrease on P-wave amplitude was always present simply due to the presence of fluids (observed in all samples of Part I and II).

The distribution of water on the carbonates was very uneven revealing strong structural heterogeneities that (1) inhibited the formation of a saturation front parallel to the base of the cylindrical sample, as seen on the samples in Part I and CIPS #1, and (2) prevented the full saturation of one of the carbonates (CB #2). The presence of structural heterogeneities (e.g. the presence of large pores or fractures) could be inferred from the P-wave velocity dependence with the confining pressure. More particularly, the non-linearity of that dependence shows that at a certain confining pressure, the fracture closed (or the pore collapsed) and the local density increased and the P-wave velocity increased (Gassmann-Wood theory).

A noticeable discrepancy from the experiments in Part I is the absence of the initial drop in P-wave velocity (the moisture weakening effect) as water enters the samples. This may be simply due to different microstructures, for example, lack of clay content in the carbonates and in the synthetic sandstones. Clay has a great capacity to absorb water inducing significant changes in mechanical properties.

OUTLOOK

Fluid injection is a common procedure in enhanced oil recovery or storage of CO_2. It is well known that the presence of fluids change the physical properties of rocks, particularly the velocity of the acoustic waves. Time-lapse seismic monitoring is used to remote-detect fluid content changes in underground reservoirs. It is commonly used on field applications where fluids are to be extracted from underground reservoirs (e.g. hydrocarbon production) or to be injected (e.g. enhanced oil recovery). Therefore, acoustic monitoring of fluid injections is the basis for locating saturation fronts and following its time-space migration.

Experimental work leading to the knowledge of the rock's physical behaviour and acoustic signature is a key factor for a better interpretation of field data. However, the characterization of acoustic-wave velocities when fluids are present is a challenging process, from acquisition to interpretation and modelling. Plus, the interaction of seismic waves with the fluid-rock system is complex and complicates the interpretation of time-lapse signals. This leads to a significant lack of experiments aimed to assess the physical behaviour of rocks in multi-phase flow conditions. This was the compelling factor of this thesis: to collect extensive, consistent data that allowed relating quantitative parameters (acoustic velocities and saturation level) with qualitative parameters (fluid distribution and geometry of the saturation front).

This thesis, “Fluid injection in reservoir rocks with X-ray CT scanning and active ultrasonic monitoring”, explored an innovative method in the field of fluid flow in experimental Rock Physics: the simultaneous acquisition of ultrasonic waveforms and X-Ray Computed Tomography scans. By combining this information with the X-ray Computed Tomography scans, the acoustic response was complemented with a dimensional image representative of the time-space evolution of the fluid in the rock. Changes in the rock can, then, be quantified during fluid injection by successfully matching a specific evolution of acoustic-wave velocities with the fluid’s saturation. This technique is an important step in interpreting the changes of the rock’s physical properties due to the presence of fluids. It also contributed to a more comprehensive insight into velocity-saturation

relationships dependence with the injection rate. A general behaviour in two types of rocks, sandstones and carbonates, was observed: dependence of acoustic velocities and fluid saturation with the flow rate and a similar trend in the evolution of those two parameters with the change of injection rates.

Reservoir monitoring during fluid injection can considerably improve reservoir performance. Therefore, I hope this thesis is an important step into interpreting field data analysis and will bring a new vision in how to interpret solid/fluid interactions at sample and pore scales.

LIST OF FIGURES

LIST OF TABLES

BIBLIOGRAPHY

Akin, S., Schembre, J. M., Bhat, S. K., Kovscek, A. R., 2000. Spontaneous imbibition characteristics of diatomite. Journal of Petroleum Science and Engineering 25, 149-165

Albright, J., Cassell, B., Dangerfield, J., Deflandre, J.-P., Johnstad, S., Withers, R., 1994. Seismic surveillance for monitoring reservoir changes. Oilfield Review 6-1

Arns, C. H., Bauget, F., Limaye, A., Sakellariou, A., Senden, T. J., Shepard, A. P., Sok, R. M., Pinczewsi, W. V., Bakke, S., Berge, L. I., Øren, P.-E., Knackstedt, M. A., 2005. Pore-scale characterization of carbonates using X-ray microtomography. SPE 90638

Assefa, S., McCann, C., Sothcott, J., 2003. Velocities of compressional and shear waves in limestones. Geophysical Prospecting 51, 1-13

Babadagli, T., Ershaghi, I., 1992. Imbibition assisted two-phase flow in natural fractures. SPE 24044

Berryman, J. G., Berge, P. A., Bonner, B. P., 2002. Estimating rock porosity and fluid saturation using only seismic velocities. Geophysics 67-2, 391-404

Biot, M. A., 1956. Theory of propagation of elastic waves in a fluid saturated porous solid. II. Higher-frequency range. Journal of the Acoustical Society of America, 28, 168-178

Birovljev, A., Furuberg, L., Feder, J., Josang, T., Maloy, K. J., Aharony, A., 1991. Gravity invasion percolation in two dimensions: experiment and simulation. Physical Review Letters 67-5, 584-588

Blunt, M. J., Scher, H., 1995. Pore-level modelling of wetting. Physical Review E 52(6), 6387-6403

Cadoret, T., Marion, D., Zinszner, B., 1995. Influence of frequency and fluid distribution on elastic wave velocities in partially saturated limestones. Journal of Geophysical Research 100 (B6), 9789-9803

Cadoret, T., Mavko, G., Zinszner, B., 1998. Fluid distribution effect on sonic attenuation in partially saturated limestones. Geophysics, 63-1, 154-160

Carles, P., Lapointe, P., 2005. Water-weakening of carbonates under stress: new insights into pore-volume compressibility measurements. Petrophysics 46-5, 361-368

Cnudde, V., Boone, M. N., 2013. High resolution X-ray computed Ttomography in geosciences: a review of the current technologies and applications. Earth-Scince Reviews, 123, 1-17

Derluyn, H., Griffa, M., Mannes, D., Jerjen, I., Dewanckele, J., Vontobel, P., Sheppard, A., Derome, D., Chudde, V., Lehmann, E., Carmeliet, J., 2013. Characterizing saline uptake and salt distributions in pororus limestone with neutron radiography and X-ray micro-tomography. Journal of Building Physics 0(0), 1-22

Ding, M., Katnzas, A., 2004. Capillary number correlations for gas-liquid systems. SEP 2004-062

Eberli, G. P., Baechle, G. T., Anselmetti, F. S., Incze, M. L., 2003. Factors controlling elastic properties in carbonate sediments and rocks. The Leading Edge 22(7), 654-660

Garg, A., Zwahlen, E., Patzek, T. W., 1996. “Experimental and Numerical Studies of One-Dimensional Imbibition in Berea Sandstone” in the Proceedings of the Sixteenth Annual American Geophysical Union Hydrology Days, pp. 171-183, Denver, CO, April 15-18

Gassmann, F., 1951. Über die elastizität poröser medien: Vierteljahrss-chrift der Naturforschenden Gesellschaft in Zurich, 96, 1-23

Guéguen, Y., Palciauskas, V., 1994. Introduction to the Physics of Rocks. Princeton University Press. ISBN-10 0691034524, 392 pp

Hill, R., 1963. Elastic properties of reinforced solids: Some theoretical principles. Journal of the Mechanics and Physics of Solids, 11, 357-372

Hirono, T., Takahashi, M., Nakashima, S., 2003. In situ visualization of fluid flow image within deformed rock by X-ray CT. Engineering Geology 70, 37-46

Johnson, D. L., 2001. Theory of frequency dependent acoustics in patchy-saturated porous media. Journal of the Acoustical Society of America 110, 682

Karimaie, H., Torsaeter, O., 2007. Effect of injection rate, initial water saturation and gravity on water injection in slightly water-wet fractured porous media. Journal of Petroleum Science and Engineering 58, 293-308

Katz, D. L., Legatski M. W., Gorring L., Nielsen, R.L., 1966. How water displaces gas from porous media. The Oil and Gas Journal, 55-60

Ketcham, R. A., Carlson, W.D., 2001. Acquisition, optimization and interpretation of X-ray computed tomography imagery: applications to the geosciences. Computer & Geosciences 27, 381-400

Knight, R., Noelen-Hoeksema, R., 1990. A laboratory study of the dependence of elastic wave velocities on pore scale fluid distribution. Geophysical Research Letters 17(10), 1529-1532

Lebedev, M., Toms-Stewart, J., Clennell, B., Pervukhina, M., Shulakova, V., Paterson, L., Müller, T. M., Gurevich, B., Wenzlau, F., 2009. Direct laboratory observation of patchy saturation and its effects on ultrasonic velocities. The Leading Edge 28(1), 24-27

Lebedev, M., Pervukhina, M., Mikhaltsevitch, V., Dance, T., Bilenko, O., Gurevich, B., 2013. An experimental study of acoustic responses on the injection of supercritical CO_2 into sandstones from the Otway Basin. Geophysics 78(4), D293–D306

Lei, X., Xue, Z., 2009. Ultrasonic velocity and attenuation during CO_2 injection into water-saturated porous sandstone: Measurements using difference seismic tomography. Physics of the Earth and Planetary Interiors 176 224-234

Leverett, M. C., 1940. Capillary Behaviour in Porous Solids

Li, K., Horne, R.N., 2010. Method to evaluate the potential of water injection in naturally fractured reservoirs, Transport in Porous Media, 83, 699-709

Li, X., Zhong, L., Pyrak-Nolte, L. J., 2001. Physics of partially saturated porous media: residual saturation and seismic-wave propagation. Annual Review of Earth and Planetary Sciences 29, 419-60

Lumley, D. E., 2001. Time-lapse seismic reservoir monitoring, Geophysics, 66-1, 50-53

MacDowell, N., Florin, N., Buchard, A., Hallett, J., Galindo, A., Jackson, G., Adjiman, C.S., Williams, C.K., Shah, N., Fennell, P., 2010. An overview of CO_2 capture technologies. Energy and Environmental Science 3, 1645-1669

Masuda, K., Nishizawa, O., Kusunose, K., Satoh, T., 1993. Laboratory study of effects of in situ stress state and strength on fluid-induced seismicity. International Journal of Rock Mechanics and Mining Sciences & Geomechanics Abstracts 30-1, 1-10

Mavko, G., Mukerji, T., Dvorkin, J., 1998. The rock physics handbook: Tools for seismic analysis in porous media. Cambridge Univ. Press, 329 pp

Mavko, G., Nolen-Hoeksema, R., 1994. Estimating seismic velocities at ultrasonic frequencies in partially saturated rocks. Geophysics, 59-2, 252-258

Mavko, G., Mukerji, T, Dvorkin, J., 2009, The Rock Physics Handbook, Tools for Seismic

Analysis of Porous Media, Second Edition. Cambridge United Press. ISBN-13 978-0-521-86136-6, 524 pp

Mees, F., Swennen, R., Van Geet, M., Jacobs, P. 2003. Applications of X-ray Computed Tomography in the Geosciences. Geological Society, London, Special Publications 215

Melean, Y., Broseta, D., Blossey, R., 2003. Imbibition fronts in porous media: effects of initial wetting fluid saturation and flow rate. Journal of Petroleum Science & Engineering 39, 327-336

Monsen, K., Johnstad, S. E., 2005. Improved understanding of velocity-saturation relationships using 4D computer-tomography acoustic measurements. Geophysical Prospecting 53, 173-181

Morrow, N. R., Mason, G., 2001. Recovery of oil by spontaneous imbibition. Colloid and Interface Science 6, 321-337

Müller, T. M., Gurevich, B., 2004. One dimensional random patchy saturation model for velocity and attenuation in porous rocks. Geophysics 69, 1166-1172

Müller, T. M., Gurevich, B., Lebedev, M., 2010. Seismic wave attenuation and dispersion due to wave-induced flow in porous rocks – A review. Geophysics 75(5), A147-A164

Nakagawa, S., Kneafsey, T. J., Daey, T. M., Freifeld, B. M., Rees, E. V., 2013. Laboratory seismic monitoring of supercritical CO_2 flooding in sandstone cores using the Split Hopkinson Resonant Bar Technique with concurrent X-ray Computed Tomography imaging. Geophysical Prospecting 61, 254-269

Noiriel, C., Luquot, Made, B., Raimbault, L., Gouze, P., Lee, J., 2009. Changes in reactive surface area during limestone dissolution: an experimental and modelling study. Chemical Geology 265, 160-170

Perkins, F.M., 1957. An Investigation of the role of capillary forces in laboratory water floods. AIME Technical note. SPE 840-G

Rangel-German, E. R., Kovscek, A. R., 2002. Experimental and analytical study of multi-dimensional imbibition in fractured porous media. Journal of Petroleum Science and Engineering 36, 45-60

Riaz, A., Tang, G.-Q., Tchelepi, H. A., Kovscek, A. R., 2007. Forced imbition in natural porous media: comparison between experiments and continuum models. Physical Reviews E-75, 036305

Rubino, J. G., Holliger, K., 2013. Research note: Seismic attenuation due to wave-induced fluid flow at microscopic and mesoscopic scales. Geophysical Prospecting, doi: 10.1111/1365-2478.12009

Schembre, J. M., Kovscek, A. R., 2003. A technique for measuring two-phase relative permeability in porous media via X-ray CT measurements. Journal of Petroleum Science and Engineering 39, 159-174

Skjæveland, S. M., Kleppe, J., 1992. SPOR monograph: recent advances in improved oil recovery methods for north sea sandstone reservoirs. Norwegian Petroleum Directorate, Stavanger, ISBN 82-7257-340-7

Steeb, H., Kurzeja, P. S., Frehner, M., Schmalholz, S. M., 2011. Phase velocity dispersion and attenuation of seismic waves due to trapped fluids in residual saturated porous media. Vadose Zone Journal, 11(3)

Strand, S., Austad, T., Puntervold, T., Hognesen, E. J., Olsen, M., Barstad S. M. F., 2008. “Smart water” for oil recovery from fractured limestone: a preliminary study. Energy and Fuels 22, 3126-3133

Sudaryanto, B., Yorstos, Y. C., 2000. Optimization of fluid front dynamics in porous media using rate control. I. Equal mobility fluids. Physics of Fluids 12, 1656

Tang, G.-Q., Kovcsek, A. R., 2011. High resolution imaging of unstable, forced imbibition in Berea sandstone. Transport of Porous Media 86, 617-634

Taylor, J., 1997. An Introduction to Error Analysis: The Study of Uncertainties in Physical Measurements. University Science Books. ISBN-10 0935702423, 327 pp.

Teufel, L.W., Rhett, D.W., Farrell, H.E. 1991. Effect of reservoir depletion and pore pressure drawdown on in situ stress and deformation in the Ekofisk Field, North Sea in the Proceedings of 32nd U.S. symposium for Rock Mechanics, Norman, Oklahoma, 10-12 July

Toms, J., Müller, T. M., Ciz, R., Gurevich, B., 2006. Comparative review of theoretical models for elastic wave attenuation and dispersion in partially saturated rocks. Soil Dynamics and Earthquake Engineering 26, 548–565

Toms-Stewart, J., Müller, T. M., Gurevich, B., Peterson, L., 2009. Statistical characterization of gas-patch distributions in partially saturated rocks. Geophysics 74-2, WA51

Tserkovnyak, Y., Johnson, D. L., 2003. Capillary forces in the acoustics of patchy-saturated porous media. Journal of the Acoustical Society of America 114(5), 2596-2606

Udey, N., 2012. Waves: Coupled porosity and saturation waves in porous media in Mathematical and numerical modelling in porous media: applications in Geosciences. CRC Press, pp. 303-333

Valvatne, P. H., Blunt, M. J., 2004. Predictive pore-scale modelling of two-phase flow in mixed wet media. Water Resources Research, 40, W07406

Yang, S., Liu, K., Mayo, S., Tulloh, A., 2012. CIPS sandstone microstructure. CSIRO. Data Collection. 10.4225/08/5045B5990B44E (http://researchdata.ands.org.au/cips-sandstone-microstructure)

Yortsos, Y. C., Huang, A. B., 1986. Linear-stability analysis of immiscible displacement: Part 1 – Simple basic flow properties. SEP 12692

Yousef, A. A., Gentil, P., Jensen, J. L., Lake, L. W., 2006. A capacitance model to infer interwell connectivity from production- and injection-rate fluctuations. Reservoir Evaluation and Engineering SPE 95322

Wellington, S. L., Vinegar, H. J., 1987. X-ray computerized tomography. Journal of Petroleum Technology 39, 885-898

White, J. E., Mihailova, N., Lyakhovitsky, F., 1975. Low-frequency seismic waves in fluid-saturated layered rocks. Journal of the Acoustical Society of America 57, S30

Wulff, A. M., Mjaaland, S., 2002. Seismic monitoring of fluid fronts: an experimental study. Geophysics 67(1), 221-229

Zhang, L., Bryant, S. L., Jennings, J. W., Arbogast, T. J., Paruchuri, R., 2004. Multiscale flow and transport in highly heterogeneous carbonates. SPE 90336

APPENDICES

A. CALIBRATION OF THE PEEK CELL

Calibration of the PEEK cell was made by comparing the P-wave in the radial direction of an aluminium rod outside of the PEEK cell and the P-wave recorded when the aluminium rod was inside the cell. The difference between the arrival times of these two waves is the "time delay", i.e. the time the P-wave takes to cross the system (cell + hydraulic oil + sleeve). The time delay is constant since the conditions of the experiment do not change during the imbibition. The delay time is 6.164 μs. All the P-wave arrival times picked in the oscilloscope during the imbibition experiments were adjusted and the P-wave velocity of the sample was calculated based on the adjusted arrival time.

The P-wave arrival time of the system (cell + hydraulic oil + sleeve) regarding the pressure-dependence was also calibrated. The P-wave arrival time was rcorded for increments of 2 MPa, from 2 to 10 MPa. Figure A.1 shows the linear dependence of the P-wave arrival time with confining pressure. The decrease is quite small, 0.2 μs in 8 MPa.

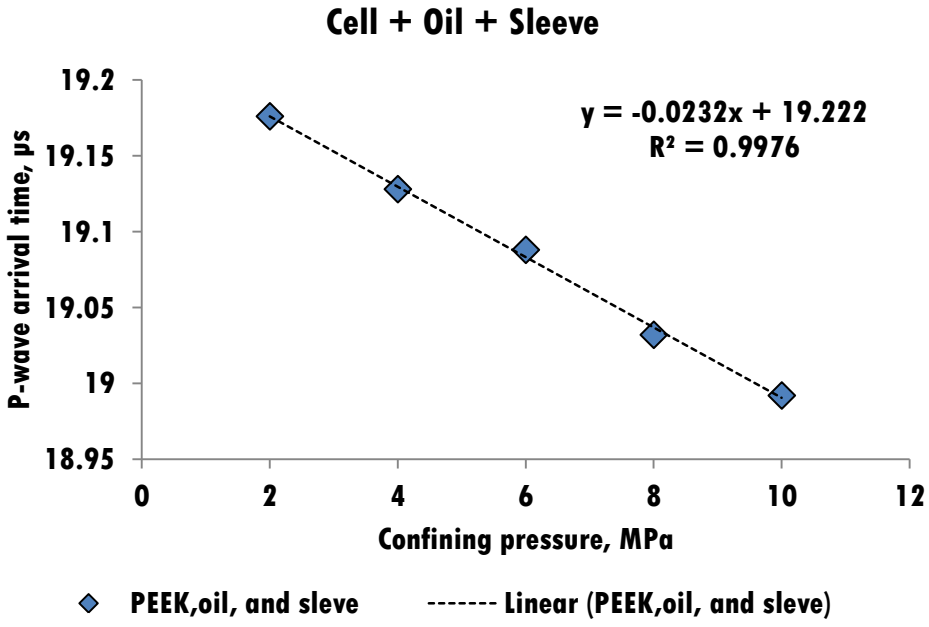

Figure A.1 Variation of the P-wave arrival time with the confining pressure of the system cell + hydraulic oil + sleeve.

B. LIST OF MANUSCRIPTS

The work described in **Chapter 2** was published in the form of an article in Geophysical Prospecting, n. 60, pages 572–580, 2012: "**Research note: Laboratory study of the influence of changing the injection rate on the geometry of the saturation front and on P-wave ultrasonic velocities in sandstone**".

- DOI: 10.1111/j.1365-2478.2011.01009.x

The work described in **Chapter 1** was accepted for publication in form of a book's chapter in "Sandstone: Geochemistry, Uses and Environmental Impact, Chapter 2", by Nova Science Publishers, and is currently being printed: "**Water imbibition into sandstones: influence of flow rate on water distribution and acoustic response**":

- https://www.novapublishers.com/catalog/product_info.php?products_id=46435&osCsid=6f727d78014c0457a4ad20826b4a24fe

The work described in **Chapter 3** was accepted for publication in Geophysical Prospecting, February 2014 and is currently in production: "**Forced imbibition into a limestone: measuring P-wave velocity and water saturation dependence on injection rate**", and is presently under the final revisions.

I am a co-author of a manuscript still in preparation: "Effects of wave-induced fluid flow and capillarity on elastic wave dispersion and attenuation". It presents the first attempt of our research group to **model** the experimental data collected during this thesis, more particularly, the results presented on Chapter 3 (variable injection rate on a limestone). The preliminary results of this work were presented in a poster at the EAGE (European Association of Geoscientists & Engineers): Workshop on Seismic Attenuation, in Singapore, Singapore, on October 2013.

The summary of the manuscript in preparation and the poster can be found in the following pages.

Effects of wave induced fluid flow and capillarity on elastic wave velocity dispersion and attenuation

Q. Qi[1], T. M. Müller[2], B. Gurevich[1,2], S. Lopes[1], M. Lebedev[1]

[1] *Department of Exploration Geophysics, Curtin University, Perth, Australia*

[2] *CSIRO Earth Science and Resource Engineering, Perth, Australia*

SUMMARY

We study the combined effects of wave-induced pressure diffusion and capillarity on acoustic wave dispersion and attenuation in partially saturated rocks. By incorporating an undrained static limit encompassing the membrane stiffness as a phenomenological parameter, the continuous random model of patchy saturation is extended to account for capillary action. The presence of surface stiffness at patch interfaces induced by capillary pressure discontinuity weakens the relative fluid-solid motion and is accompanied with lower viscous dissipation. The phase velocity is enhanced due to superimposed stiffening from wave-induced pressure equilibration and capillarity reinforcement. We apply this model to check the associated velocity/attenuation saturation relations for a forced water imbibition experiment in which the small capillary number indicates the presence of capillary forces. Using statistical characterisation, we study effect of fluid distribution by extracting the degree of saturation, patch correlation, fluid compressibility contrast and specific surface area from X-ray computed tomography images. The autocovariance functions show consistency with the fluid patch alteration during saturation evolution. At median saturation level, the autocovariance function can be well approximated by a superposition of two Debye correlation functions. The associated correlation length and

specific surface area exhibit inverse proportional and proportional behaviour with increasing water saturation. The degree of fluid heterogeneity shows a dependency on relative arrangement between saturation and characteristic patch size. Acoustic analysis based on such random heterogeneities reveals that mesoscopic flow only can explain partially the velocity deviation from Gassmann-Wood bound and also leads to an attenuation overestimation. The capillarity-extended random patchy saturation model yields consistent predictions for the velocity- and attenuation-saturation relations. There is only one unconstrained parameter —— the shape factor entering the capillarity extended random patchy saturation model. By matching the model predictions with the experimentally determined velocities, we inversely model this shape factor. We compare the forward modelled attenuation with attenuation of the ultrasonic waveforms and its consistency corroborates the validity of the shape factor. Hence, the new model shows capability of modelling the acoustic properties in the immiscible flow regime where capillarity can be significant. Our results suggests that the wave-induced fluid redistribution at mesoscopic patches in conjunction with capillary action has important implication for interpreting acoustic change in reservoir condition involving a small capillary number. The capillarity extended random patchy saturation theory also provides insights in extracting crucial saturation information from seismic data.

Key words: Image processing; Tomography; Seismic attenuation; Theoretical seismology; Wave propagation; Acoustic properties.

Seismic Attenuation in Partially Saturated Porous Rocks

Experiment, Theory and Simulation

Q. Qi (Curtin University), E. Caspari (Curtin University and CO2CRC), J.G. Rubino (University of Lausanne), S.C. Lopes (Curtin University), M. Lebedev (Curtin University), T.M. Müller (CSIRO Earth Science and Resource Engineering) & B. Gurevich (Curtin University and CSIRO)

EARTH SCIENCE AND RESOURCE ENGINEERING
www.csiro.au

Summary: Seismic waves propagating in porous rocks saturated with two immiscible fluids can be strongly attenuated. This is because seismic waves induce relative motion between the fluid and solid phases. The effect is known as wave-induced fluid flow (WIFF, Müller et al., 2010). Particularly, millimetre- to centimetre-sized (so-called mesoscopic) fluid patches have important implications for interpreting laboratory and field observations. To characterise the effects of mesoscale fluid patches on the change of acoustic properties, we carry out laboratory experiments, analyse well log data and perform numerical simulations at seismic frequencies. We also develop rock physics models for partially saturated rocks.

Details: Müller et al., 2010

Attenuation Mechanism

Velocity saturation relation: Homogeneous versus Patchy saturation

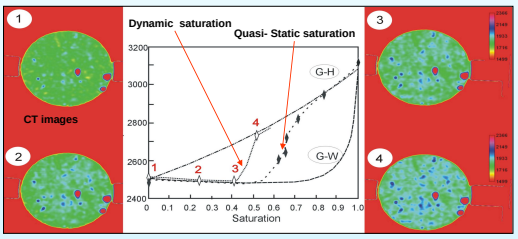

Wave-induced fluid flow

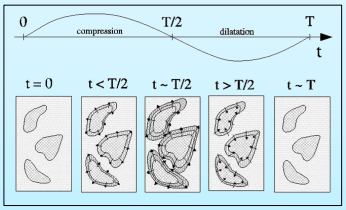

Mesoscopic Heterogeneity

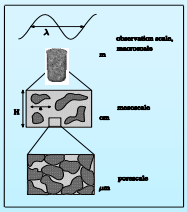

Laboratory Experiments

To better understand and quantify the dependence of velocity-saturation relationships on the injection rate, forced imbibition experiments are performed using Savonnières limestone. The injection is monitored with X-ray Computed Tomography (CT) and active ultrasonic measurements, so that the time-space distribution of the invading fluid and the associated acoustic change can be simultaneously observed.

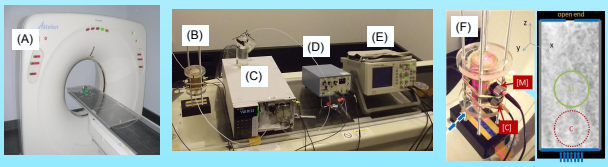

Fig. 1: Experimental setup: (A) X-ray CT scanner; (B) Sample set for vertical injection; (C) Injection pump; (D) Pulser/receiver and (E) oscilloscope (F) Savonnières limestone cylinder connected to two pairs of transducers: position C, close to the area of injection, and position M, in the middle of the sample. Also shown is the CT scan of the dry sample. Dashed red and green circles mark the positions of the transducers.

Details: Lopes et al., 2013

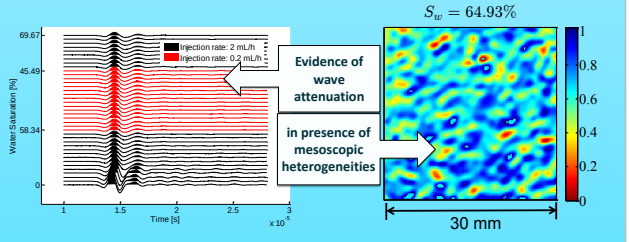

Fig. 2: (a) The ultrasonic waveforms at various saturations, the black waveforms correspond to 2 mL/h injection rate while the red waveforms correspond to injection rate 0.2 mL/h. (b) Water saturation image reveals millimetre-scale fluid patches and contains morphological information for statistical analysis.

Capillarity Extended Random Medium Model

We study the combined effects of wave-induced pressure diffusion and capillarity on acoustic waves. By incorporating an undrained static limit encompassing the membrane stiffness as a phenomenological parameter, the continuous random model of patchy saturation is extended to account for capillary action. The presence of surface stiffness at patch interfaces induced by capillary pressure discontinuity weakens the relative fluid-solid motion and is accompanied with lower viscous dissipation. The phase velocity is enhanced due to superimposed stiffening from wave-induced pressure equilibration and capillarity reinforcement.

Details: Qi et al., 2013

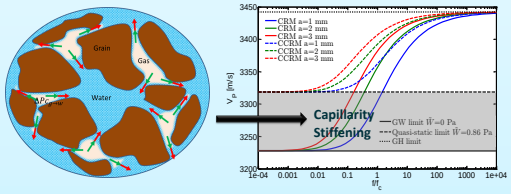

Fig. 3: (a) Schematic representation of the unsaturated rock at pore-scale. The arrows signify the local capillary pressure across the fluid interfaces. By postulating a macroscopic boundary condition $\mathbf{p} - \mathbf{p}' = \mathbf{W}\emptyset(\mathbf{U_n} - \mathbf{u_n})$, the effect of capillary forces at pore-scale is upscaled to mesoscopic scale. (b) The incorporation of the boundary condition into poroelasticity framework results in a rescaled static limit.

Laboratory Data Modelling

We apply this model to check the associated velocity/attenuation saturation relations for a forced water imbibition experiment in which the small capillary number indicates the dominance of capillary forces in forming the fluid distribution.

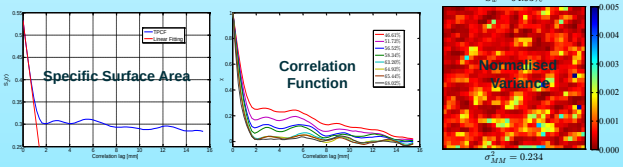

Fig. 4: Input parameters for acoustic analysis of random fluid heterogeneities (**Fig. 2**(b)). (a) Two-point correlation function (blue curve) and linear fitting (red line) for specific surface area extraction. (b) Fluid distribution characterisation at different saturation levels using the normalised autocovariance function. (c) Normalised variance provides the degree of fluid compressibility contrast.

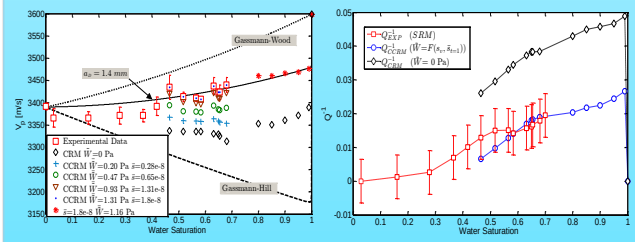

Fig. 5: Velocity-saturation relation (VSR) and attenuation-saturation relation (ASR) modelling results using the newly developed capillarity-extended CRM model(CCRM). (a) The phase velocities for increasing membrane stiffness ($\bar{W}$=0~1.31 Pa) are modelled and compared with laboratory observations (red squares). (b) The deduced membrane stiffness that matches the experimental VSR ($\bar{W}$=1.31) is then used to model the experimental ASR (black and blue symbols). A reasonable match is obtained. In the absence of capillary action the attenuation would be over-predicted (black diamonds). This supports the choice of membrane stiffness value in (a). Thus, the CCRM model allow us to consistently model velocity and attenuation.

ACKNOWLEDGEMENTS

We wish to acknowledge the funding provided by the CRGC and the CIRPS scholarship.

Log Data Modelling

Based on time-lapse sonic and neutron porosity logs from the Nagaoka CO_2 sequestration experiment, a *P*-wave velocity-saturation relation at reservoir depth is retrieved. It does not coincide with either of the end-member models of uniform and patchy saturation but falls in between even if realistic error estimates for the host rock properties are considered. Assuming a random distribution of CO_2 patches it is shown that the mechanism of wave-induced flow can be evoked to explain this velocity-saturation relation. Characteristic CO_2 patch size estimates range from 1 to 5 mm. Such mesoscopic heterogeneity can be responsible for attenuation and dispersion in the well logging frequency band.

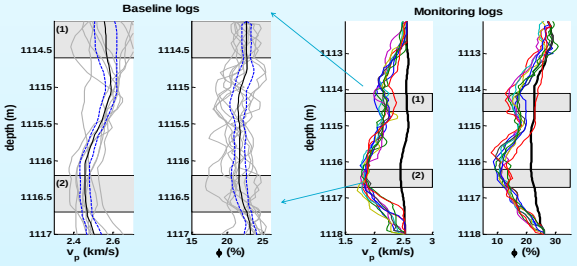

Fig . 6 : (a) Sonic and neutron porosity baseline logs 1–13 (grey lines), averaged baseline log (black line) and the corresponding standard variation (dashed blue line). (b) Sonic and neutron porosity monitoring logs 17–26 (coloured lines) and averaged baseline log (black line). Gary boxes indicate the chosen depth intervals (data from Konishi et al. [2009]).

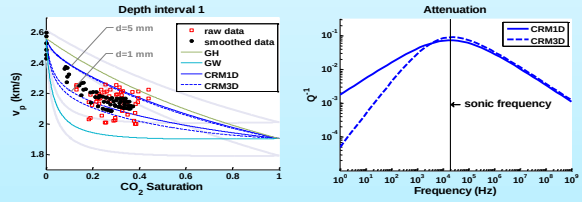

Fig. 7 : (a) Comparison between theoretical models (GW, GH and CRM) and log data for depth interval 1. The grey lines show the deviations of the GW and GH bounds, obtained from the standard variation (non-repeatability) of the repeated baseline logs. The CRM models are displayed for 20 kHz with correlation lengths d of 1 mm and 5 mm (solid and dashed blue curves). **(**b) Corresponding attenuation for the correlation length of 1 mm.

Seismic Signatures of Patchy Saturation

In order to study WIFF effects on seismic data, we consider a poorly consolidated sandstone (Utsira sand) with a spatially variable CO_2 -brine distribution in the form of irregular patches fully saturated with CO_2 and zones fully saturated with brine. Then, we applied a numerical upscaling procedure based on oscillatory compressibility tests (Rubino et al., 2009) in a Monte Carlo fashion to obtain the statistical behaviour of attenuation and phase velocity as functions of frequency. Finally, we use such curves to perform propagation of seismic waves employing corresponding equivalent viscoelastic solids, and compare the results with those obtained using Gassmann's equation.

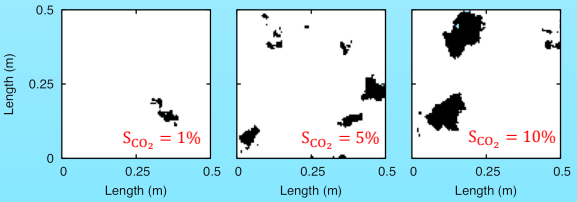

Fig. 8: Samples of quasi-fractal distributions of CO_2 and brine in the Utsira Sand for a correlation length of 0.1m and CO_2 saturations of 0.01, 0.05 and 0.1, respectively. We generate these binary heterogeneous fields based on the von Karman self-similar correlation functions.

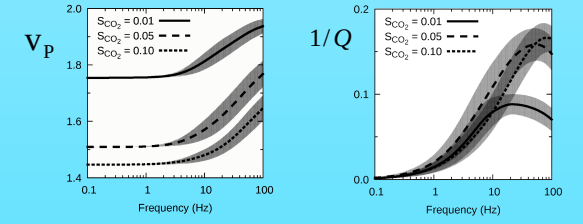

Fig. 9: Mean equivalent (a) phase velocity and (b) inverse quality factor as functions of frequency for three CO_2 saturation levels. Shaded gray areas indicate their corresponding standard deviation intervals. These curves were computed applying a numerical oscillatory compressibility test in a Monte Carlo fashion to a large number of samples.

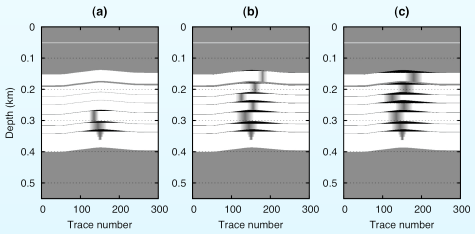

Fig. 10: Scheme of the geological model (Sleipner Field) employed to analyze mesoscopic effecs on seismic data containing patchy saturation, related to a CO_2 injection operation. The black thin areas indicate the main component of CO_2 (charcterized by a CO_2 saturation of 0.9), while the narrow gray shaded areas indicate the presence of diffuse component of CO_2, with saturations varying from 0.1 in their axial parts to zero in the outer parts. Labels a) to c) indicate three different stages of the injection process.

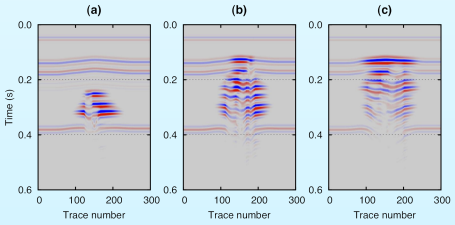

Fig. 11: Seismic response of a model similar to the Sleipner field considering the mesoscopic effects due to the patchy nature of the fluid distributions. Labels a) to c) indicate the three injection stages depicted in **Fig. 10**.

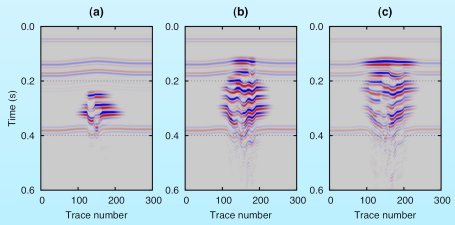

Fig. 12: Seismic responses of a model similar to the Sleipner field, obtained replacing the viscoelastic media by elastic media with the same bulk density and shear velocity, but with a compressional velocity given by Gassmann's formula. Labels a) to c) indicate the three injection stages depicted in **Fig. 10**.

Future Work

❖ How come 2-phase flow concepts into play?

Injection rate dependence

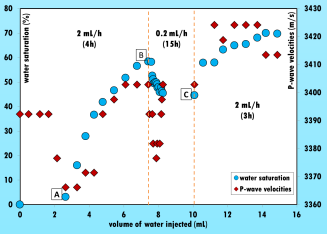

Irreducible water saturation

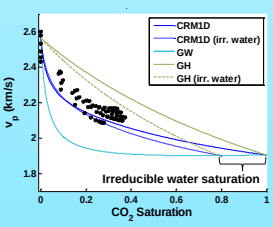

❖ Can we image fluid patches?

Pore-scale imaging and modelling

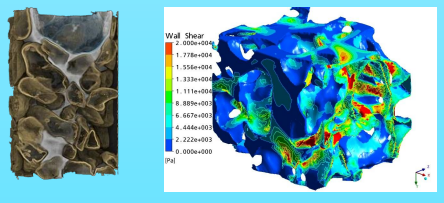

Time-lapse data is needed for further analysis!

REFERENCES

Caspari, E., T.M. Müller and B. Gurevich, 2011. Time-lapse sonic logs reveal patchy CO_2 saturation in-situ, Geophys. Res. Lett. 38:L13301-1-L13301-4.

Konishi, C., H. Azuma, D. Nobuoka, Z. Xue and J. Watanabe, 2009. CO_2 saturation estimation from P-wave velocity changes by considering patchy saturation, paper presented at Summer Research Workshop, Soc. of Explor. Geophys., Banff, Alberta, Canada, 23-27 Aug.

Lopes, S., M. Lebedev, T. M. Müller, M. B. Clennell and B. Gurevich, 2013. Forced imbibition into a limestone: Measuring P-wave velocity and water saturation dependence on injection rate, submitted Geophysical Prospecting.

Müller, T.M., B. Gurevich and M. Lebedev, 2010. Seismic wave attenuation and dispersion resulting from wave-induced flow in porous rocks - a review, Geophysics 75:75A147-75A164

Qi, Q., T.M. Müller, B. Gurevich, S. Lopes and M. Lebedev, 2013. Effects of capillarity and wave-induced fluid flow on elastic wave velocity dispersion and attenuation, manuscript prepared submission.

Rubino, J., D.R. Velis and M.D. Sacchi, 2011. Numerical analysis of wave-induced fluid flow effects on seismic data: Application to monitoring of CO2 storage at the Sleipner field, J. Geophys. Res. 116:B03306-1-B03306-16.

Rubino, J.G., Ravazzoli, C.L. and Santos, J.E., 2009. Equivalent viscoelastic solids for heterogeneous fluid-saturated porous rocks, Geophysics, 74, N1-N13.

Toms, J., T.M. Müller and B. Gurevich, 2007. Seismic attenuation in porous rocks with random patchy saturation, Geophys. Prospect. 55:671-678.

C. LIST OF CONFERENCES ATTENDED

The work I developed during my thesis (between July 2010 and October 2013) was presented at the following national (Australian) and international conferences:

2nd International Workshop on Rock Physics - Southampton, UK, August 2013

Oral presentation: Laboratory study of the influence of changing the injection rate on P-wave velocities and water saturation in a Limestone

Curtin Reservoir Geophysics Consortium, CRGC - Perth, Australia, December 2012

Poster presentation: Influence of changing the flow rate in the acoustic response and saturation during forced imbibition in a limestone

American Geophysical Union, AGU - San Francisco, USA, December 2012

Poster Presentation: Influence of changing the flow rate in the acoustic response and saturation during forced imbibition in a limestone

Australian Society of Exploration Geophysics, ASEG - Brisbane, Australia, February 2012

Oral presentation: Laboratory study of the influence of changing the injection rate on P-wave velocities and water saturation in a limestone

New Technology Forum & Topical Conference - Perth, Australia, September 2011

Poster presentation: Laboratory study of the influence of changing the injection rate on P-wave velocities and water saturation in a limestone

- **Awarded "Best Poster"**

European Geosciences Union, EGU - Vienna, Austria, April 2011

Poster presentation: Reservoir rock fluid imbibition experiments: complex study using X-ray computer tomography and ultrasonic techniques

Curtin Reservoir Geophysics Consortium, CRGC - Perth, Australia, December 2010

Oral presentation: Reservoir rock fluid imbibition experiments: complex study using X-Ray computer tomography and ultrasonic techniques

Cooperative Research Centre for Greenhouse Gas Technologies, CO2CRC - Melbourne, Australia, December 2010

Poster presentation: Reservoir rock fluid imbibition experiments: complex study using X-Ray computer tomography and ultrasonic techniques